THE UNIVERSITY
of EDINBURGH

Appendix A – Luminescence dating of sediments from Underhoull and Lund, Unst, Shetland

Citation: Kinnaird, T.C., Sanderson, D.C.W., Preston, J., Dugmore, A.J. and Newton, A.J. (2017) Luminescence dating of sediments from Underhoull and Lund, Unst, Shetland. Technical Report. SUERC, East Kilbride, UK.

Scottish Universities Environmental Research Centre

Luminescence dating of sediments from Underhoull and Lund, Unst, Shetland

November 2016

T.C. Kinnaird[1], D.C.W. Sanderson[1],
J. Preston[2], A.J. Dugmore[2], A.J. Newton[2]

[1]SUERC, East Kilbride, Glasgow
[2]School of Geosciences, University of Edinburgh, Edinburgh

East Kilbride Glasgow G75 0QF Telephone: 01355 223332 Fax: 01355 229898

Summary

This report is concerned with optically stimulated luminescence (OSL) investigations of sediments from the the foreshore at Burga Sands, Underhoull, and a dune section at Lund, in south-west Unst (Shetland). In both places, samples were collected to establish the timing of sand accumulation, and in doing so, contribute to an expanding catalogue of historical sand blows in the Northern Isles and Scotland. The sediment chronologies were used to interpret the environmental record of sand movements in the vicinity of Underhoull and Lund, and the adjacent Norse longhouses and chapel. The Underhoull sections included samples located under the walls of two boat noosts, with potential to constrain the ages of construction, and, in one case potentially modification, based on sand units enclosed by the exposed structural elements. The sediment stratigraphies on the foreshore of Burga Sands were also explored through four profiles, comprising the natural accumulations adjacent to two noosts (profiles 1 and 2), and the substrate sequences to the noosts (P3&4). The dune section at Lund was explored in a single profile (P5).

This report describes the progression from fieldwork and sampling, through initial luminescence screening measurements made with the portable OSL reader (on 45 samples), to subsequent calibrated analysis in the laboratory, first, to characterise the OSL and IRSL signals from each sample, then by targeted quantitative OSL dating on a further set of 10 samples. The 'field profiles' provided the first indication that the substrate stratigraphies at Underhoull, extend from the late glacial period to the modern day. The maxima and dynamic ranges in signal intensities for the sequences beneath the noosts, suggest that the construction and modification of these structures were temporally distinct. For the Lund section, the range in signal intensities through these sediments, indicate a shorter chronology, which was confirmed by subsequent characterisation of the profiling samples in the laboratory.

The following chronology was obtained for the Underhoull section:

1) onset of sand activity, as recorded in the sedimentary archives of profiles 1 and 2, at 3.22 ± 0.29 ka (1210 ± 290BC; SUTL2861) and 1.99 ± 0.15 ka (AD30 ± 150; SUTL2863)
2) construction of the W noost at 0.81 ± 0.07 ka (AD1210 ± 70; SUTL2867)
3) modification and re-built of the E noost at 0.48 ± 0.06 ka (AD1540 ± 60; SUTL2866)
4) continued sand movements into the early 20th century AD (0.12 ± 0.06 ka; AD1900 ± 60; SUTL2862), with arguably heightened activity at the onset of the Little Ice Age (0.64 ± 0.10 ka; AD 1380 ± 60; SUTL2866).

For the Lund dune section, the sediment chronology spans from the early 14th century AD through to the early 18th century AD (0.70 ± 0.05 ka; SUTL2868, through 0.52 ± 0.04 ka; SUTL2869, to 0.31 ± 0.02 ka; SUTL2870), corresponding with the onset and waning stages of the Little Ice Age.

The chronology presented here is consistent with an emerging regional framework of sand movements in the Northern Isles and Scotland, with activity in the Neolithic, Early and Late Bronze Ages, the Iron Age, the Viking/Medieval period, and Little Ice Age. The Underhoull

section dated here provides a broad chronology for sand blow and, importantly, places sediments underneath two noosts into the late Norse/ Mediaeval period. The dune section dates a high resolution local record within the last 700 years. Opportunities to extend the high resolution palaeoenvironmental record were identified in the adjacent land and dune-scape, and especially in the palaeo-loch landward of the Lund section, which has received sand in the past.

Contents

List of figures

List of tables

1. Introduction

This paper reports optically stimulated luminescence (OSL) investigations of the foreshore sediments at Burga Sands, Underhoull, and Lund, in south-west Unst (Shetland), which were undertaken to to better understand both the late Holocene history of sand accumulation and the use of the foreshore by people. The Underhoull sections included samples located under the walls of two boat noosts, with the aim to constrain the ages of construction, and, in one case potential modification, based on sand units enclosed by the exposed structural elements.

The work follows earlier OSL dating studies of wind-blown sands in Scotland and the Northern Isles, which have identified periods of increased sand movements in the Neolithic, Early and Late Bronze Ages, within the Iron Age, the Viking/Medieval period, and the Little Ice Age (Burbidge et al., 2001; Sommerville, 2003). In a broader regional setting there are signs of emerging convergence between dates for sand deposition in NW Scotland (our data; Burbidge et al., 2007a; Gilbertson et al., 1999; Kinnaird et al., 2011; Sommerville, 2003; Sommerville et al., 2007; Wilson et al., 2002), NW Ireland (Wilson and Braley, 1997; Wilson et al., 2004), Southern Ireland (Wintle et al., 1998), NE England (Wilson et al., 2001) and Denmark (Clemmensen et al., 2001; Clemmensen et al., 2009), and in the radiocarbon-dated aeolian sand record in coastal peat bogs (Anderson, 1998; Langdon et al., 2003; Wilson, 2002). Luminescence ages for sand deposition in the 18th and 19th centuries have also been linked to historic accounts of storms in this period. For earlier periods, the physical evidence shows both erosive and accumulative features in terrestrial and coastal settings. Within Shetland, Scatness Broch has yielded OSL dates from 760 ± 60 BC to AD 1860 ± 5 (Rhodes et al., 2003), and a series of analyses from the site of Broo, and Quendale have produced both LIA associated dates (Kinnaird et al., 2014; Kinnaird et al., 2013) and evidence of earlier depositional relics within the surrounding landscape. At Channerwick, Shetland Mainland (Kinnaird et al 2016), deposition from the mid/late first millennium BC and first millennium AD has been registered in the stratigraphy of a broch/wheelhouse. On Unst, the Norse settlement of Sandwick South has yielded dates for sand deposition in the early 13th century AD, and also in the late 18th /early 19th centuries AD (Kinnaird et al., 2015). The material from Sandwick South presented challenging conditions for luminescence dating associated with the ultrabasic materials from SE Unst. The samples collected from Underhoull and Lund come from a different set of lithological contexts, but also from areas with surficial till, and one of the questions associated with these analyses concerns the extent to which quartz SAR OSL methods could be applied here.

The sampling and analysis reported here were conducted in support of the German Research Council (DFG) funded 'Harbours in the North Atlantic AD 800-1300 (HaNoA)' project, which aims to identify potential harbours and anchorages throughout this region (Iceland, Greenland, Shetland and Faroe), and to evaluate the quality of different landing-places within natural harbours. Within this study the PhD research of John Preston includes modelling geomorphological changes on the island of Unst, which may have had destabilised beaches and

embayments exploited by the Norse, in response to changes in climate conditions from the Medieval Climatic Anomaly to the Little Ice Age to the present day.

Fieldwork was conducted in February 2016 with the aim of identifying sediment units which could be dated to ascertain the timings of significant sand blows in the vicinity of both Underhoull and Lund. Both sites have Norse associations, with Longhouses excavated at Lower and Upper Underhoull (Canmore ID 28; Site No. HP50SE 1), a boat noost at Burga Sands (Canmore ID 88166; Site No. HP50SE 45), and a prominent Norse chapel, west of Lunda Wick (Canmore ID 64; Site No. HP50SE 6). The fieldwork identified a coastal exposure in the vicinity of Burga sands where two noosts could be seen and linked to stratigraphy. It also opened a dune section which was sampled for palaeo-environmental exploration.

The report outlines the fieldwork, luminescence profiling results, both in the field and in the laboratory, and the methods and results of luminescence dating measurements and their chronological significance. A total of 45 profiling samples, collected from 5 vertical sequences were investigated in field and laboratory, and 10 samples were subjected to quartz OSL Single Aliquot Regenerative (SAR) dating procedures.

2. OSL Sampling

Fieldwork took place between the 22nd and 28th of February, with David Sanderson and John Preston, being joined by Andrew Dugmore and Anthony Newton on 25th February. The area visited was Underhoull and Lund (figs 2-1 to 2-3), with sections investigated at the foreshore at both Underhoull (noost sections; figs 2-2 to 2-6; SUTL2861-67) and Lund (palaeo-environmental section; Fig 2-7; SUTL2868-70).

Figure 2-1: GoogleEarth Images showing the relationship of Unst in the Sheltland Isles; and the Underhoull/Lund area, with the locations of the noost and environmental sampling sections marked. See photograph in figure 2-2.

Sampling was targeted to explore the sediments associated with two noosts, one intact (noost 2; profile 4), and one later modified (noost 1; profile 3), and the natural accumulations along strike (profiles 1 and 2), including significant sand accumulations which preserve an environmental record of sand activity (Fig 2-2). In addition, a palaeo-environmental section, in the foreshore of the next embayment to the SW was investigated (Fig 2-2). Samples were collected in five profiles (figs 2-4 to 2-7).

Figure 2-2: Overview of Underhoull and Lunda Wick; the locations of the two sampling sites are marked

Figure 2-3: Overview of the foreshore at Underhoull showing the noost ocations

Profiles 1 to 4 sampled the Underhoull section above the high water mark. Profiles 1 and 2 explore the stratigraphy of the Holocene (post-glacial) backshore/beach

accumulations (Fig. 1-1), encompassing at the base, re-worked glacial materials (P1/1-2; P2/1-2), the overlying buried soil (P1/3; P2/3), clay (P1/4-5; P2/4) and sand sequences (P1/6-8; P2/5-7), into the turf base (P1/9). Profiles 3 and 4 encompass the same sediments, but in adjacent positions, beneath noost 1, (P3) and noost 2 (P4). At the base, the profiles enclose the reworked glacial materials (P3/1-2; 4/1), and above that lie sands that correlate with the upper parts of profiles 1 and 2 (P3/3-4; P4/2-4). The samples provide a temporal (and spatial) framework to interpret the climatic conditions prior to, and the lead up to the construction of the noosts, and the conditions post-construction. Samples for dating were positioned through these profiles, at the base and top of the sand sequences (in P1 and P2; Fig. 1-2), and directly under the two noosts (in P3 and P4, respectively; Fig 1-2). The dating questions associated with these samples relate to the timing of the first sand blow, as preserved here (SUTL2861 and 2863), the cessation of sand activity (SUTL2862 and 2864), the timing of construction and modification of the two noosts (SUTL2865 and 2866).

Figure 2-4: Photographs showing the modified noost (noost 1) on the foreshore of Underhoull Bay; illustrating the late construction of an internal wall to reduce the size of the primary noost. The vertical step from the noost floor to the current beach indicates significant erosion, beach instability and a possible reason for the noosts to fall into disuse.

The fifth profile explores the sediments preserved along strike, in a second, more westward embayment of the bay, providing a further opportunity to explore the environmental record as archived in the backshore/beach accumulations (Fig. 1-3). The profile encompasses 2 m of sands and buried soils, including top down, the turf base (1 sample, P5/20), three soils (5 samples, P5/18-17, P5/5 and P5/3-2), and the enclosing sands, alternating between darker, dirtier sands (9 samples, P5/19, P5/15-14, P5/12-8, P5/4 and P5/1) and lenses of cleaner, paler sands (4 samples, P5/16, P5/13 and P5/7-6). Dating samples were positioned throughout this sequence to provide temporal constraints to constrain the environmental record as preserved in this section.

Small quantities of sediment (15-20 g each) were collected under dark cover from 45 positions within the 5 sediment sequences, for screening measurements (Table 2-1) and further laboratory characterisation (Table 2-1) with the aim of generalising the luminescence stratigraphy throughout the sequence. Samples for luminescence dating were collected from the key stratigraphic units (Table 2-2) using steel tubes, 3.5 cm in diameter, which were inserted into the cleaned face of the section, extracted, and sealed. In-situ field gamma spectrometry (FGS) measurements (see below) were taken from these positions using a Rainbow Multichannel Analyser coupled with a 2 x 2" NaI probe. In-situ field gamma dose rates are listed in table 2-3.

	Field no.	SUTL no.	Height/cm	Field description/ context	Archaeological significance
Profile 1	P1/9	2871I	37[a]	turf base	
	P1/8	2871H	27[a]	clean sand	cessation of sand activity
	P1/7	2871G	22[a]	top base sand	
	P1/6	2871F	17[a]	base red sand	onset of sand activity (in position of profile)
	P1/5	2871E	9[a]	sandy clay	
	P1/4	2871D	3[a]	clay above dark layer	
	P1/3	2871C	-2[a]	dark layer	=P2/3
	P1/2	2871B	-8[a]	weathered till	=P2/2=3/1=4/1
	P1/1	2871A	-13[a]	till	=P2/1
Profile 2	P2/7	2872G	58[a]	top red sand	cessation of sand activity
	P2/6	2872F	45[a]	middle red sand	
	P2/5	2872E	30[a]	base red sand	onset of sand activity
	P2/4	2872D	10[a]	clay above dark layer	
	P2/3	2872C	1[a]	dark layer	=P1/3
	P2/2	2872B	-4[a]	weathered till	=P1/2=3/1=4/1
	P2/1	2872A	-10[a]	till	=P1/1
Profile 3	P3/4	2873D	13[a]	top sand	TPQ for noost 1
	P3/3	2873C	9[a]	base sand	=P1/6=2/5?; onset of sand activity
	P3/2	2873B	3[a]	dark layer	=P1/3=2/3?
	P3/1	2873A	-2[a]	top of till	=P1/2=2/2=4/1
Profile 4	P4/4	2874D	30[a]	top red sand	TPQ for noost 2
	P4/3	2874C	25[a]	middle red sand	
	P4/2	2874B	13[a]	base red sand	=P1/6=2/5?; onset of sand activity
	P4/1	2874A	6[a]	clay on till	=P1/2=2/2=3/1
Profil	P5/20	2875T	4	turf/roots	

	P5/19	2875S	14	sand/soil mix	
	P5/18	2875R	23	top, sand dark soil	
	P5/17	2875Q	31	base, sandy dark soil	
	P5/16	2875P	35	light sand (3)	
	P5/15	2875O	41	top, red sand	
	P5/14	2875N	56	base, red sand	
	P5/13	2875M	62	light sand (2)	
	P5/12	2875L	64	top, red sand	
	P5/11	2875K	87	middle, red sand	
	P5/10	2875J	103	base, red sand	
	P5/9	2875I	108	sandy soil	
	P5/8	2875H	118	Sand	
	P5/7	2875G	131	light sand, top of charcoal-bearing horizon	
	P5/6	2875F	162	light sand, base of charcoal-bearing horizon	cultural activity?
	P5/5	2875E	175	dark sand	
	P5/4	2875D	187	sand	
	P5/3	2875C	195	brown sandy soil	
	P5/2	2875B	198	sand	
	P5/1	2875A	209	base of section, light sand (1)	

Table 2-1: Sample descriptions, contexts and archaeological significance of the profiling samples used for initial screening and laboratory characterisation [a] **distance from weathered surface cut on till (estimated from local datums)**

Associated with profile	Field no.	SUTL no.	Depth /cm	Context	Archaeological significance
1	OSL1	2861	100†	red sand (base)	onset of sand blow
	OSL2	2862	40†	clean sand	later sand blow
2	OSL3	2863	150†	red sand (base)	onset of sand blow
	OSL4	2864	100†	red sand (middle)	progression?
	OSL5	2865	40†	red sand (top)	cessation of sand activity
3	OSL6	2866	50†	sand (top)	modification of noost
4	OSL7	2867	40†	sand (top)	construction of noost
5	OSL8	2868	175	sands, above brown sandy soil (lowest sampled in profile)	TAQ for soil formation
	OSL9	2869	65	sands, top of charcoal-bearing horizon	constraint on age of charcoal-bearing horizon
	OSL10	2870	31	sands	

Table 2-2: Sample descriptions, contexts and archaeological significance of sediment samples SUTL2832-2839 †depths estimated relative to the overlying landforms for cosmic attenuation estimation

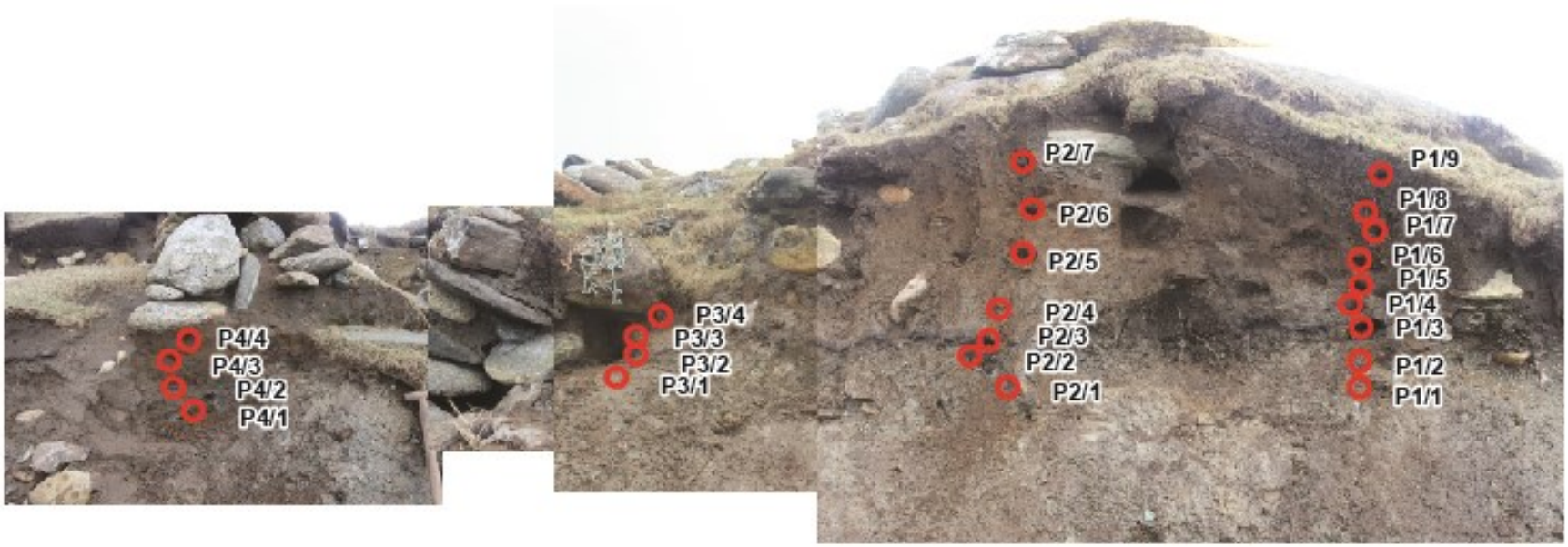

Figure 2-5: Profiles 1-4, Underhoull, with profiling samples marked

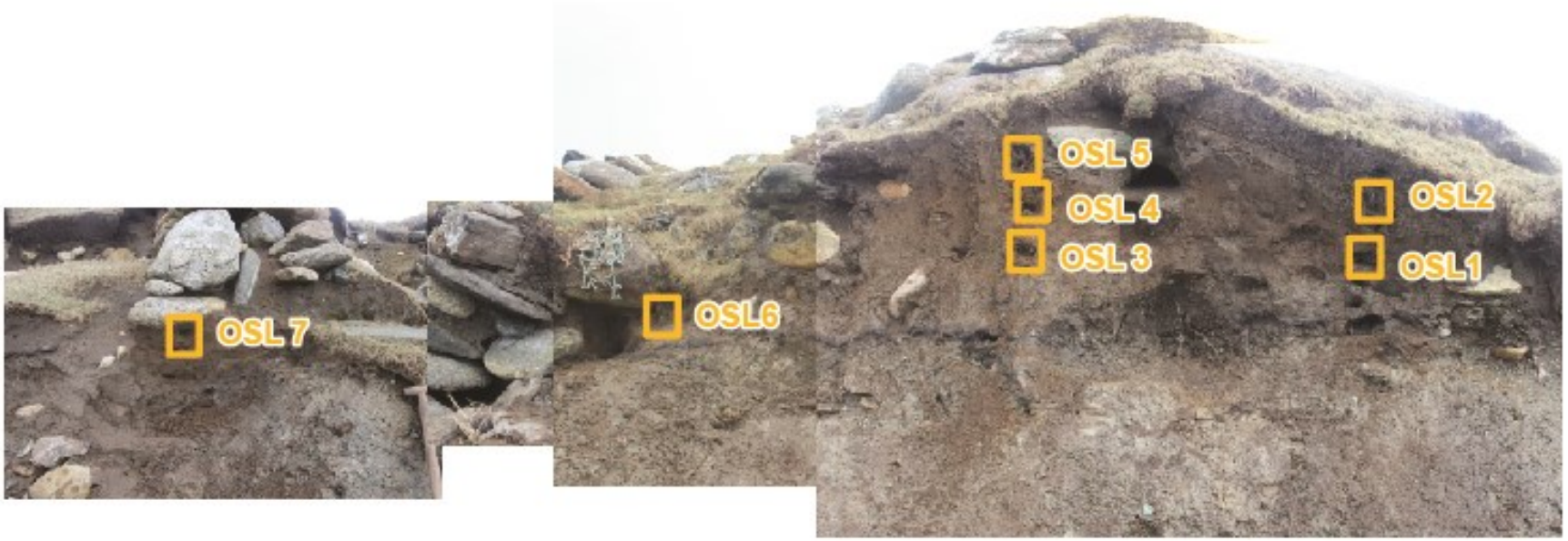

Figure 2-6: Profiles 1-4, Underhoull, with dating positions marked

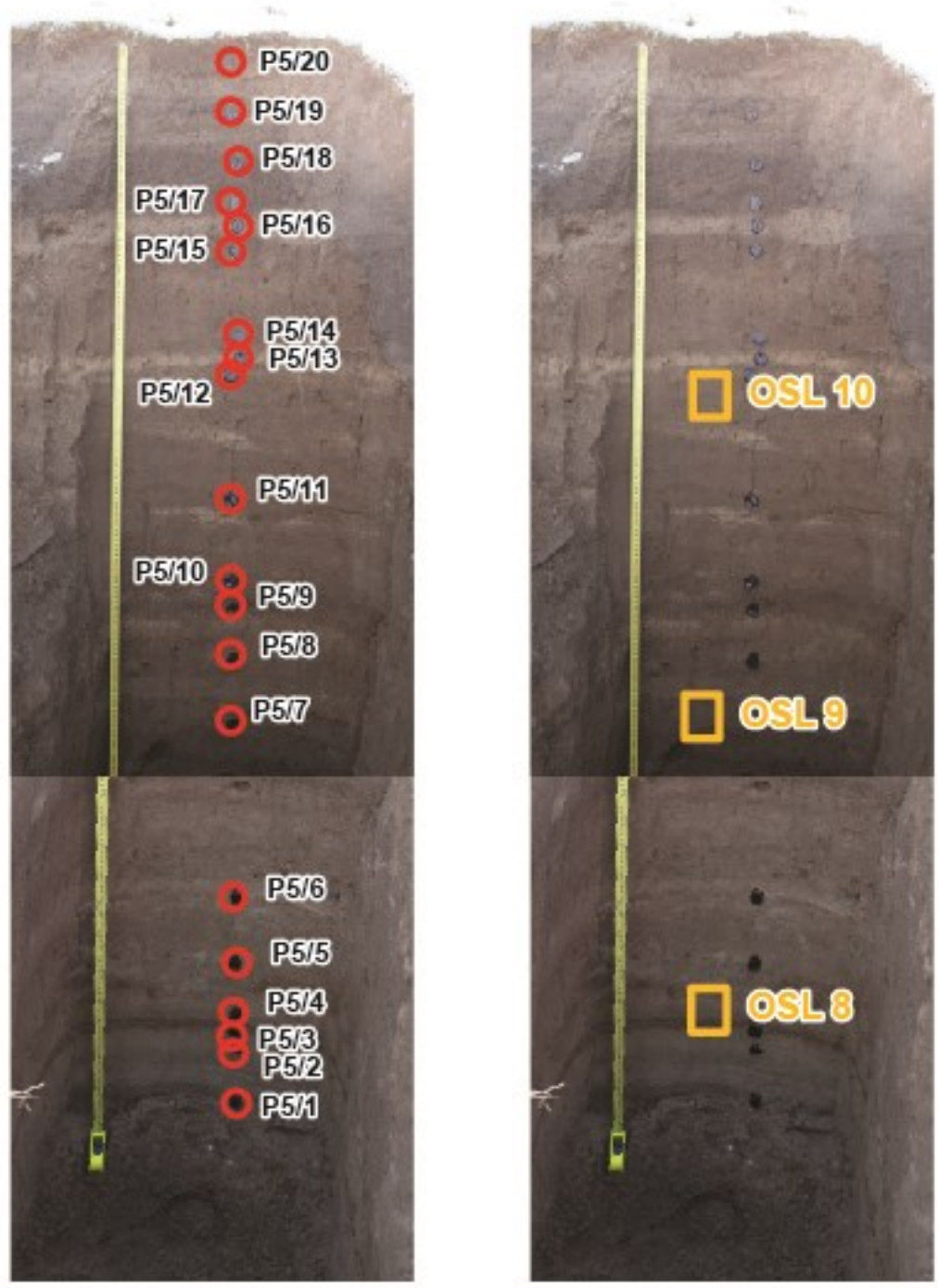

Figure 2-7: Profile 5, beach section, Underhoull, with profiling samples and dating positions shown

SUTL no.	Context no.	Archaeological significance	FGS, wet / mGy a^{-1}
2861	OSL1	onset of sand blow	0.31 ± 0.02
2862	OSL2	later sand blow	0.25 ± 0.02
2863	OSL3	onset of sand blow	0.36 ± 0.02
2864	OSL4	progression?	0.34 ± 0.02
2865	OSL5	cessation of sand activity	0.44 ± 0.02
2866	OSL6	modification of noost	0.41 ± 0.02
2867	OSL7	construction of noost	0.36 ± 0.02

Table 2-3: Field gamma spectrometry (FGS) data

3. Preliminary luminescence stratigraphies

All samples were first appraised using the SUERC portable OSL reader, following an interleaved sequence of system dark count (background), infra-red stimulated luminescence (IRSL) and OSL, similar to that described by Sanderson and Murphy (2010). This method allows for the calculation of IRSL and OSL net signal intensities, depletion indices and IRSL:OSL ratios, which are then used to generate luminescence-depth profiles. The results are shown in figures 3-1 to 3-3, and presented in table 3-1.

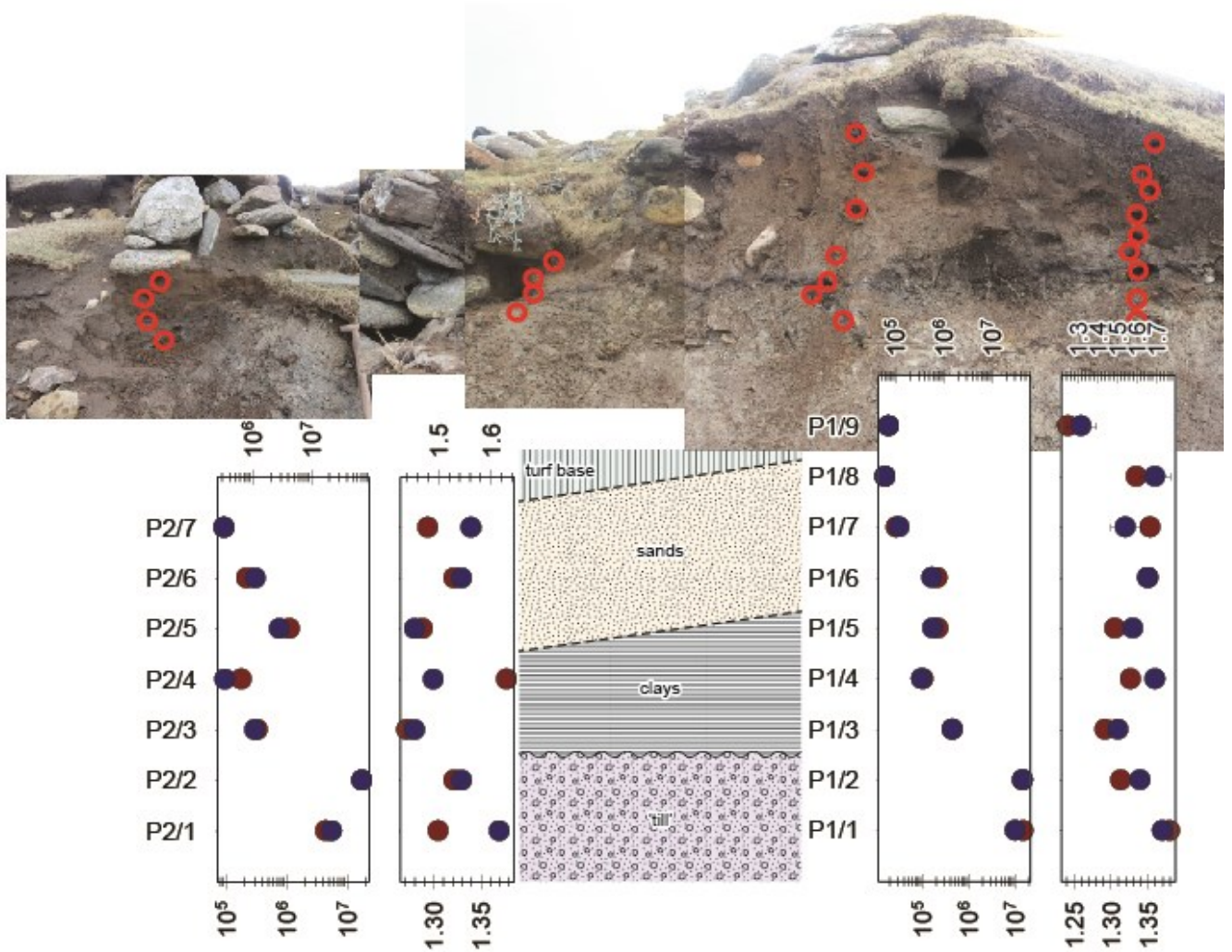

Figure 3-1: Photograph, and luminescence -depth profile, for the

NB: the first plot in each is the plot of signal intensity (net signal intensities in photon counts) versus depth, the second, depletion ratio (the first 30s of measurement/the second 30s of measurement) versus depth. The bottom horizontal axis is the response to blue stimulation; the upper axis, the response following infra-red stimulation

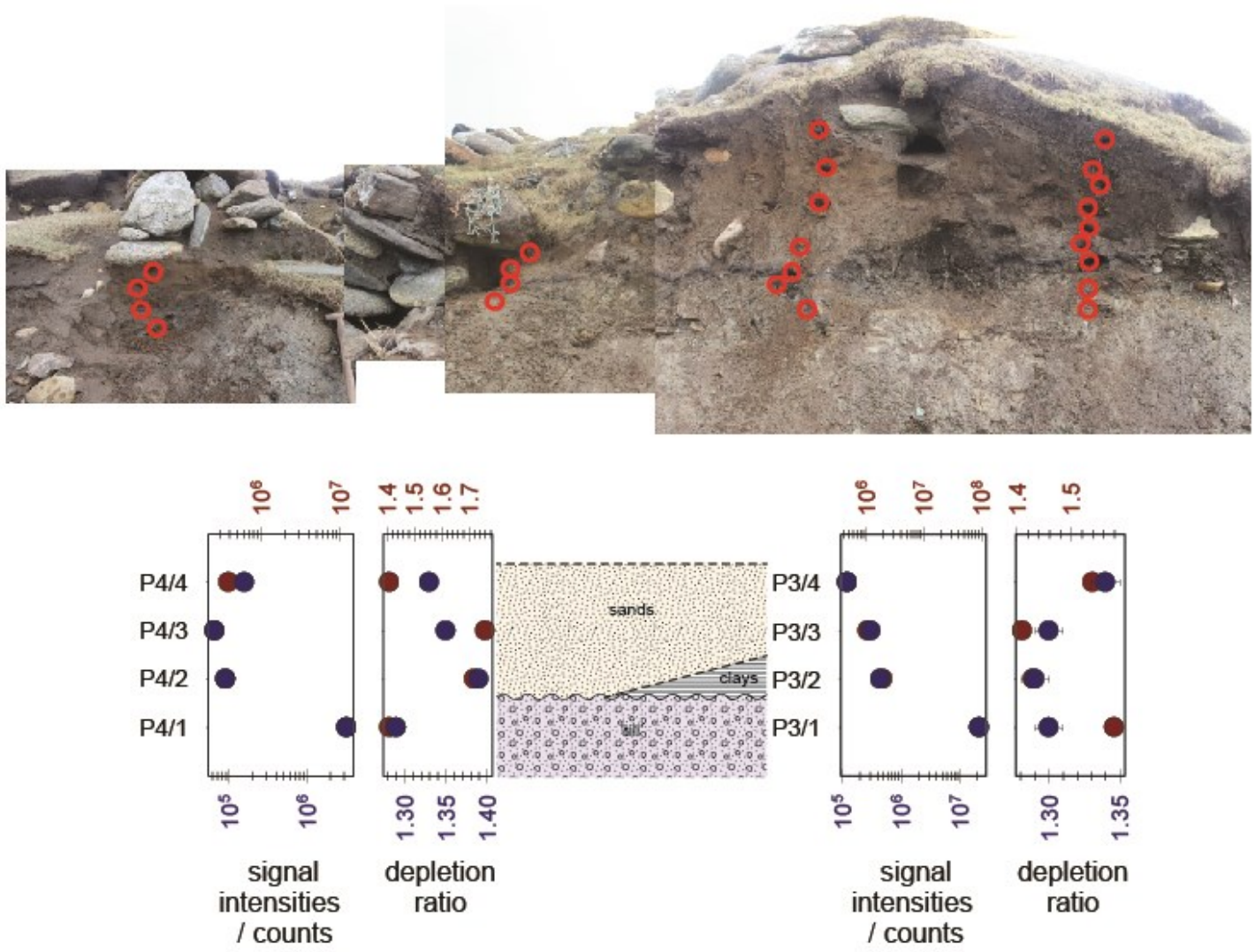

Figure 3-2: Photograph, and luminescence -depth profile, for the sediment stratigraphy sampled in profiles 3 and 4

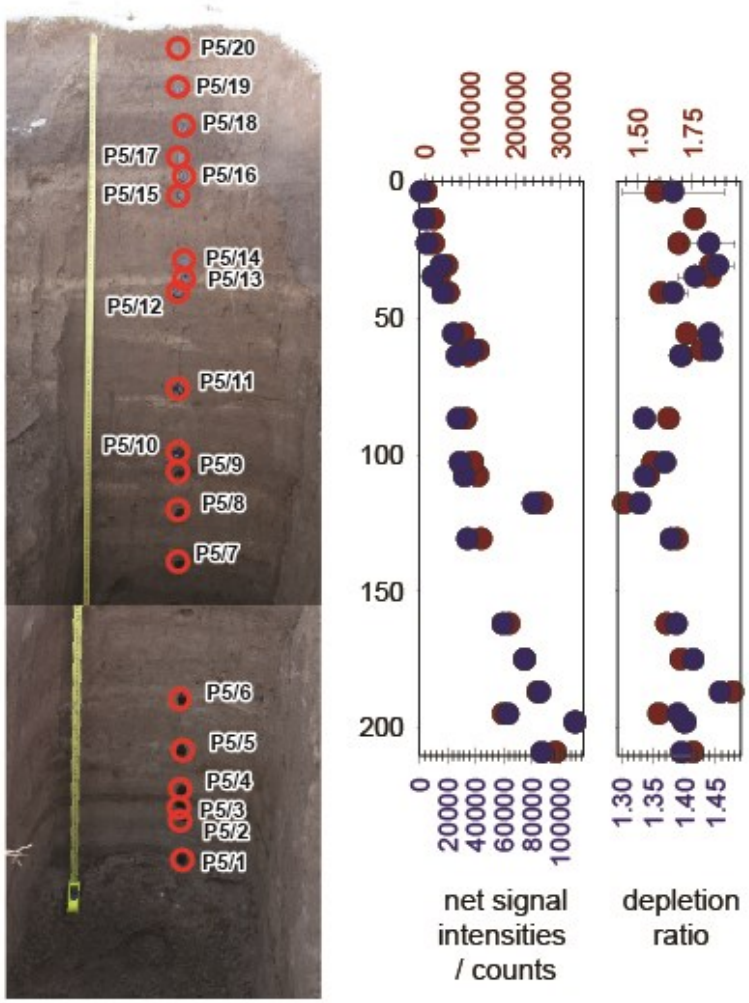

Figure 3-3: Photograph, and luminescence -depth profile, for the sediment stratigraphy sampled in profile 5

Sample no.	IRSL net signal intensities	IRSL depletion ratio	OSL net signal intensities	OSL depletion ratio	IRSL/OSL ratio
P1/1	10203164 ± 3201	1.37 ± 0.01	45489580 ± 6758	1.77 ± 0.01	0.22 ± 0.01
P1/2	14894251 ± 3868	1.34 ± 0.01	44186836 ± 6664	1.52 ± 0.01	0.34 ± 0.01
P1/3	455212 ± 677	1.31 ± 0.01	1530540 ± 1241	1.44 ± 0.01	0.30 ± 0.01
P1/4	97066 ± 315	1.36 ± 0.01	378146 ± 617	1.57 ± 0.01	0.26 ± 0.01
P1/5	170328 ± 416	1.33 ± 0.01	773952 ± 883	1.49 ± 0.01	0.22 ± 0.01
P1/6	162418 ± 405	1.35 ± 0.01	745981 ± 866	1.66 ± 0.01	0.22 ± 0.01
P1/7	32134 ± 185	1.32 ± 0.02	105632 ± 328	1.67 ± 0.01	0.30 ± 0.01
P1/8	16041 ± 134	1.36 ± 0.02	61643 ± 253	1.60 ± 0.01	0.26 ± 0.01
P1/9	19035 ± 145	1.26 ± 0.02	73423 ± 275	1.25 ± 0.01	0.26 ± 0.01
P2/1	170328 ± 416	1.33 ± 0.01	773952 ± 883	1.49 ± 0.01	0.22 ± 0.01
P2/1	5576089 ± 2367	1.37 ± 0.01	17683807 ± 4215	1.50 ± 0.01	0.32 ± 0.01
P2/2	17492761 ± 4192	1.33 ± 0.01	73049828 ± 8566	1.53 ± 0.01	0.24 ± 0.01
P2/3	300034 ± 551	1.28 ± 0.01	1208983 ± 1104	1.44 ± 0.01	0.25 ± 0.01
P2/4	96350 ± 314	1.30 ± 0.01	646569 ± 807	1.63 ± 0.01	0.15 ± 0.01
P2/5	764875 ± 878	1.28 ± 0.01	4272293 ± 2072	1.47 ± 0.01	0.18 ± 0.01

P2/6	307389 ± 557	1.33 ± 0.01	797237 ± 896	1.53 ± 0.01	0.39 ± 0.01
P2/7	93404 ± 309	1.34 ± 0.01	327240 ± 575	1.48 ± 0.01	0.29 ± 0.01
P3/1	21430063 ± 4640	1.30 ± 0.01	92541562 ± 9642	1.58 ± 0.01	0.23 ± 0.01
P3/2	444344 ± 669	1.29 ± 0.01	1946670 ± 1399	1.43 ± 0.01	0.23 ± 0.01
P3/3	306312 ± 556	1.30 ± 0.01	1074063 ± 1039	1.41 ± 0.01	0.29 ± 0.01
P3/4	121448 ± 352	1.34 ± 0.01	471859 ± 690	1.54 ± 0.01	0.26 ± 0.01
P4/1	3249190 ± 1807	1.29 ± 0.01	12050631 ± 3480	1.41 ± 0.01	0.27 ± 0.01
P4/2	89081 ± 302	1.39 ± 0.01	356627 ± 600	1.72 ± 0.01	0.25 ± 0.01
P4/3	64715 ± 259	1.35 ± 0.01	260528 ± 513	1.76 ± 0.01	0.25 ± 0.01
P4/4	156615 ± 398	1.33 ± 0.01	388871 ± 627	1.41 ± 0.01	0.40 ± 0.01
P5/1	87762 ± 300	1.40 ± 0.01	289627 ± 540	1.75 ± 0.01	0.30 ± 0.01
P5/2	111333 ± 337	1.40 ± 0.01	333370 ± 581	1.71 ± 0.01	0.33 ± 0.01
P5/3	63618 ± 257	1.39 ± 0.01	174950 ± 422	1.60 ± 0.01	0.36 ± 0.01
P5/4	86346 ± 297	1.46 ± 0.01	250618 ± 503	1.94 ± 0.01	0.34 ± 0.01
P5/5	75376 ± 279	1.42 ± 0.01	222234 ± 474	1.70 ± 0.01	0.34 ± 0.01
P5/6	59851 ± 249	1.39 ± 0.01	187571 ± 436	1.63 ± 0.01	0.32 ± 0.01
P5/7	34825 ± 192	1.38 ± 0.02	126460 ± 359	1.68 ± 0.01	0.28 ± 0.01

P5/8	81720 ± 290	1.33 ± 0.01	259051 ± 512	1.44 ± 0.01	0.32 ± 0.01
P5/9	32386 ± 186	1.34 ± 0.02	119102 ± 348	1.55 ± 0.01	0.27 ± 0.01
P5/10	29472 ± 178	1.37 ± 0.02	108088 ± 332	1.57 ± 0.01	0.27 ± 0.01
P5/11	27860 ± 173	1.34 ± 0.02	92188 ± 308	1.64 ± 0.01	0.30 ± 0.01
P5/12	27314 ± 173	1.39 ± 0.02	98199 ± 318	1.71 ± 0.01	0.28 ± 0.01
P5/13	38363 ± 201	1.44 ± 0.02	120571 ± 350	1.79 ± 0.01	0.32 ± 0.01
P5/14	24787 ± 164	1.44 ± 0.02	87573 ± 300	1.73 ± 0.01	0.28 ± 0.01
P5/15	17108 ± 137	1.38 ± 0.02	54602 ± 238	1.61 ± 0.01	0.31 ± 0.01
P5/16	10040 ± 110	1.42 ± 0.03	34202 ± 190	1.83 ± 0.02	0.29 ± 0.01
P5/17	16038 ± 132	1.45 ± 0.02	50834 ± 230	1.83 ± 0.02	0.32 ± 0.01
P5/18	5838 ± 86	1.44 ± 0.04	21708 ± 152	1.69 ± 0.02	0.27 ± 0.01
P5/19	3949 ± 76	0.58 ± 0.02	21410 ± 153	1.76 ± 0.03	0.18 ± 0.01
P5/20	1537 ± 57	1.38 ± 0.08	5763 ± 87	1.59 ± 0.05	0.27 ± 0.01

Table 3-1: Field profiling data, as obtained using portable OSL equipment, for the sediment stratigraphies examined at Underhoull

In the sediment stratigraphies associated with the noosts (profiles 1 - 4), signal intensities progress through the sands down-profile from 6.2 × 10^4 to 4.3 × 10^6 OSL photon counts and 1.6 × 10^4 to 7.7 × 10^5 IRSL photon counts, consistent with a normal age progression, and a chronology between deposition of the upper and lower units. Interestingly, the substrate stratigraphies to the noosts are each characterised by discrete luminescence 'packages', with the sands beneath the modified noost showing a signal progression over a dynamic range of 2-3, and the sands beneath the intact noost showing a progression over a range of 1-2. Notably though, the sands immediately beneath each noost are characterised by similar OSL and IRSL signal intensities i.e 4.7 × 10^5 and 3.9 × 10^5 OSL counts, and 1.2 × 10^5 and 1.6 × 10^5 IRSL counts (Noost 1 and 2, respectively).

Further down-profile, across the boundary between the sands and clays, signal intensities drop off, presumably in response to the darker colour of the sediments; yet, internally, these sediments are marked by progression in signal intensity with depth. Notably, within this unit, it is the profiling samples that are characterised by the lowest signal intensities that have the highest depletion indices, which would be consistent with these samples being better bleached at deposition. The basal units, those encompassing the glacial materials and its weathered interface, are characterised by the largest OSL and IRSL signal intensities in the profiles, in excess of 1.7 × 10^7 OSL photon counts and 1.0 × 10^7 IRSL counts. Interestingly, the dynamic ranges in OSL and IRSL signal intensities across this lithostratigraphic boundary, suggest a substantial temporal break. For profile 1, the progression in OSL signal intensities with depth, from the turf base (P1/8-9), through the clay/red sands (P1/5-6), to the till (P1/1-2) - from c. 6.8 × 10^4 counts (averaged across P1/1-2), to 7.6 × 10^4 counts to 4.5 × 10^7 counts, is broadly consistent with the expected age range of 50 years, to 500 years, to last glacial maximum.

Signal intensities are comparable for equivalent units across all four profiles.

In the beach section located along strike, in the more western embayment of the bay, the range in signal progressions from 5.8 × 10^3 to 3.3 × 10^5 counts following OSL, and from 1.5 × 10^3 to 1.1 × 10^5 counts following IRSL, suggests that only the later Holocene archive was sampled. If the ratios in luminescence intensities between the different lithostratigraphic units identified in the noost sections are projected onto this luminescence sequence, then the ranges in OSL and IRSL signal intensities are only suggestive of a temporal record spanning the last 500-600 years.

4. Laboratory calibrated screening measurements

Having established that there are measureable stratigraphic trends in the luminescence 'field' profiles, it remains to be determined whether these signal progressions are influenced, or indeed controlled, by sensitivity variations. Laboratory profiling provides one means to assess luminescence sensitivity distributions, and the first preliminary assessment of apparent doses.

4.1. Methodology

All profiling samples were wet sieved at 90 and 250µm. The 90-250 µm fractions were then subjected to acid treatments of 1M HCl for 10 mins, 15% HF for 15mins and 1M HCl for 10mins. The samples were split into two fractions, one for polymineral analysis and one for quartz analysis.

Luminescence sensitivities (Photon Counts per Gy) and stored doses (Gy) were evaluated from paired aliquots of the polymineral and HF-etched quartz fractions, using Risø DA-15 automatic readers (following procedures establised in Burbidge et al., 2007b; Sanderson et al., 2001; Sanderson et al., 2003). The readout cycles comprised a natural readout, followed by readout cycles for a nominal 1Gy test dose, a 5Gy regenerative dose, and a further 1Gy test dose. For the polymineral samples, a 260˚C preheat was followed by 60s OSL measurements using the IR LEDs at 50˚C, the IR LEDs at 225˚C (the post-IR IRSL signal), the blue LEDs at 125˚C, and a TL measurement to 500˚C. For the quartz samples, a 240˚C preheat was used with 60s OSL measurements using the blue LEDs.

4.2. Results of screening measurements

The data are tabulated below (tables 4-1 to 4-4), and presented graphically in figures 4-1 to 4-9.

The laboratory profiling data reproduces the maxima and trends in the field profiling dataset. For the western sections, those associated with the noosts, the substrate stratigraphies show a straight-forward progression in OSL stored dose estimates with depth. For the substrate stratigraphies adjacent to the built structures, the upper sand accumulations (those not affected by the turf base), show a progression from c. 1.3 to 2.5 Gy, the lower sand/clay sequence from c. 4 to 6 Gy, with the basal units, returning stored dose values in excess of 9-10 Gy. Intriguingly, OSL sensitivities peak across the boundary between the two lower units, suggesting a new source of material into the system, immediately after the palaeo-surface was cut on top of the

'weathered till'. Then, through the clays and upper sand accumulations, OSL sensitivities decrease, returning to values more comparable with those derived from the till, which suggests a mixing between these allochthonous materials and more locally-derived materials.

Beneath the noosts, the luminescence stratigraphies are variable, with each spanning different maxima and ranges in OSL stored dose estimates (and suggesting different depositional histories). For the substrate stratigraphy beneath noost 1, stored dose values range from 3 to 5 Gy, for sands immediately beneath the noost, to those in excess of 10 Gy for the basal units. In contrast, for the substrate stratigraphy beneath noost 2, stored dose values range between 0.2 and 1 Gy. Again, luminescence sensitivities are variable through these sections, with the maxima in sensitivities recorded across the 'till' - clay/sand boundary. It is important to note that the quartz OSL stored dose values vary independently of sensitivity, and that low sensitivities do not necessarily equate to low stored dose values. Given this, and withstanding substantial environmental dose rate variations, the maxima and range in OSL stored dose estimates as recorded for these two stratigraphies, suggests that different depositional ages for strata related to construction and modification of these noosts.

To the west, for the strata sampled in the beach section, the quartz age signature within the luminescence stratigraphies is obscured by variable luminescence sensitivities, which vary over 3 orders of magnitude throughout the profile, but generally increase down-section. Intriguingly, if only the bright horizons are considered, stored dose estimates show a progression with depth, from 0.3 Gy to 0.8 Gy. Notably, this indicates that only the later part of the environmental history (as recorded in the noost sections) is represented in the beach section, which strengthens the hypothesis first raised after field profiling. The IRSL stored dose values are more straight-forward to interpret, showing a progression from 3 to in excess of 10 Gy with depth, with more consistent luminescence sensitivities (~ 1000 counts Gy^{-1}). However, a stored dose value of 3 Gy given the expected environmental dose rates, would correspond to substantially older than expected ages.

In summary, the results of laboratory profiling are consistent with the data generated by field profiling - reinforcing: 1. the substantial temporal break between the glacial materials, and the overlying sand accumulations, which internally represent only a short chronology, 2. the suggestion that the substrate sequences beneath the two noosts - one intact, and potentially surviving from construction, and the second modified, and recording a later re-structuring of the noost - represent accumulations over different timescales and periods, suggesting that the two surviving noosts may be of different age, and 3. the environmental section to the west, in the adjacent embayment, only accessed strata related to the later environmental history of the site, covering the last 500-600 years..

SUTL no.	Field ID	Stored dose / Gy		Sensitivity / photon counts Gy^{-1}		/ Gy	/ photon counts Gy^{-1}
		Ali #1	Ali #2	Ali #1	Ali #2	Mean	
P1/9	2871I	1.1 ± 0.1	2.6 ± 0.4	641 ± 25	171 ± 13	1.9 ± 0.8	406 ± 235
P1/8	2871H	3.9 ± 0.5	4.7 ± 0.7	177 ± 13	138 ± 12	4.3 ± 0.4	157 ± 19
P1/7	2871G	1.7 ± 0.2	1.7 ± 0.1	513 ± 23	616 ± 25	1.7 ± 0.1	565 ± 51
P1/6	2871F	3.2 ± 0.2	1.9 ± 0.1	918 ± 30	784 ± 28	2.5 ± 0.7	851 ± 67
P1/5	2871E	3.8 ± 0.1	3.4 ± 0.1	14865 ± 122	31043 ± 176	3.6 ± 0.2	22954 ± 8089
P1/4	2871D	5.7 ± 0.1	5.5 ± 0.1	3661 ± 61	10741 ± 104	5.6 ± 0.1	7201 ± 3540
P1/3	2871C	7.2 ± 0.6	13 ± 1.2	295 ± 17	201 ± 14	10 ± 3	248 ± 47
P1/2	2871B	6.6 ± 0.6	8.7 ± 0.7	226 ± 15	393 ± 20	7.7 ± 1.1	310 ± 84
P1/1	2871A	9.6 ± 0.9	14 ± 1	204 ± 14	266 ± 16	12 ± 2	235 ± 31
P2/7	2872G	1.4 ± 0.1	1.3 ± 0.1	15790 ± 126	2507 ± 50	1.3 ± 0.1	9148 ± 6641
P2/6	2872F	1.4 ± 0.1	1.2 ± 0.1	4569 ± 68	1065 ± 33	1.3 ± 0.1	2817 ± 1752
P2/5	2872E	2.9 ± 0.2	2.2 ± 0.1	569 ± 24	1262 ± 36	2.5 ± 0.4	916 ± 347
P2/4	2872D	3.7 ± 0.1	4.3 ± 0.1	1970 ± 44	2947 ± 54	4 ± 0.3	2459 ± 488
P2/3	2872C	6.4 ± 0.1	47 ± 0.3	12172 ± 110	50775 ± 225	27 ± 20	31474 ± 19302
P2/2	2872B	31 ± 2	13 ± 1	871 ± 30	320 ± 18	22 ± 9	596 ± 275

P2/1	2872A	94 ± 1	14 ± 0.2	13462 ± 116	7760 ± 88	54 ± 40	10611 ± 2851
P3/4	2873D	3.7 ± 0.4	2.9 ± 0.4	195 ± 14	168 ± 13	3.3 ± 0.4	182 ± 14
P3/3	2873C	21 ± 1	4.6 ± 0.4	3235 ± 57	258 ± 16	13 ± 9	1747 ± 1488
P3/2	2873B	5.8 ± 0.1	10 ± 0.1	29466 ± 172	24781 ± 157	8 ± 2	27123 ± 2342
P3/1	2873A	31 ± 2	72 ± 0.7	365 ± 19	17910 ± 134	51 ± 20	9138 ± 8773
P4/4	2874D	0.2 ± 0.1	0.1 ± 0.0	6353 ± 80	29046 ± 170	0.2 ± 0.1	17699 ± 11346
P4/3	2874C	0.2 ± 0.1	0.2 ± 0.0	7049 ± 84	41253 ± 203	0.2 ± 0.1	24151 ± 17102
P4/2	2874B	0.2 ± 0.1	0.6 ± 0.1	13744 ± 117	1378 ± 37	0.4 ± 0.2	7561 ± 6183
P4/1	2874A	1.0 ± 0.1	0.9 ± 0.0	97675 ± 313	11916 ± 109	1.0 ± 0.1	54796 ± 42880
P5/20	2875T	5.9 ± 0.8	3.7 ± 0.6	142 ± 12	129 ± 11	4.8 ± 1.1	135 ± 7
P5/19	2875S	3.1 ± 0.4	5.6 ± 0.7	152 ± 12	187 ± 14	4.3 ± 1.3	170 ± 18
P5/18	2875R	2.5 ± 0.3	5.6 ± 0.7	245 ± 16	167 ± 13	4 ± 2	206 ± 39
P5/17	2875Q	2.1 ± 0.2	3.5 ± 0.5	328 ± 18	176 ± 13	2.8 ± 0.7	252 ± 76
P5/16	2875P	0.2 ± 0.0	0.1 ± 0.0	5987 ± 77	54648 ± 234	0.1 ± 0.0	30317 ± 24330
P5/15	2875O	3.0 ± 0.4	5.5 ± 0.8	183 ± 14	156 ± 12	4.3 ± 1.3	169 ± 14
P5/14	2875N	2.3 ± 0.3	3.5 ± 0.5	176 ± 13	158 ± 13	2.9 ± 0.6	167 ± 9
P5/13	2875M	4.7 ± 0.7	3.2 ± 0.4	136 ± 12	189 ± 14	3.9 ± 0.7	162 ± 26

P5/12	2875L	2.5 ± 0.3	0.7 ± 0.1	230 ± 15	1158 ± 34	1.6 ± 0.9	694 ± 464
P5/11	2875K	1.6 ± 0.1	5.9 ± 0.7	576 ± 24	152 ± 12	3.7 ± 2.2	364 ± 212
P5/10	2875J	0.7 ± 0.1	0.7 ± 0.1	2216 ± 47	16259 ± 128	0.7 ± 0.0	9237 ± 7021
P5/9	2875I	1.9 ± 0.2	3.0 ± 0.4	222 ± 15	135 ± 12	2.5 ± 0.6	178 ± 43
P5/8	2875H	0.6 ± 0.1	0.6 ± 0.1	25990 ± 161	9274 ± 96	0.6 ± 0.0	17632 ± 8358
P5/7	2875G	4.7 ± 0.6	2.1 ± 0.2	185 ± 14	450 ± 21	3.4 ± 1.3	317 ± 132
P5/6	2875F	1.9 ± 0.2	0.8 ± 0.1	334 ± 18	571 ± 24	1.3 ± 0.6	452 ± 118
P5/5	2875E	0.7 ± 0.1	0.8 ± 0.1	23769 ± 154	21325 ± 146	0.8 ± 0.0	22547 ± 1222
P5/4	2875D	5.2 ± 0.7	4.7 ± 0.5	154 ± 12	208 ± 14	5 ± 0.2	181 ± 27
P5/3	2875C	1.8 ± 0.1	1.1 ± 0.1	694 ± 26	4374 ± 66	1.5 ± 0.3	2534 ± 1840
P5/2	2875B	1.1 ± 0.1	1.1 ± 0.1	13496 ± 116	16949 ± 130	1.1 ± 0	15222 ± 1727
P5/1	2875A	0.8 ± 0.1	0.8 ± 0.1	67414 ± 260	92200 ± 304	0.8 ± 0	79807 ± 12393

Table 4-1: OSL screening measurements on paired aliquots of 90-250µm 40% HF-etched 'quartz'

SUTL no.	Field ID	Stored dose / Gy		Sensitivity / photon counts Gy^{-1}		/ Gy	/ photon counts Gy^{-1}
		Aliquot 1	Aliquot 2	Aliquot 1	Aliquot 2	Mean	
P1/9	2871I	0.21 ±0.02	0.20 ±0.03	147 ± 12	56 ± 8	0.20 ±0.01	102 ±45
P1/8	2871H	0.25 ±0.01	0.31 ±0.02	191 ± 14	178 ± 13	0.28 ±0.03	185 ±7
P1/7	2871G	0.38 ±0.02	8.82 ±0.27	194 ± 14	246 ± 16	4.60 ±4.22	220 ±26
P1/6	2871F	3.09 ±0.07	1.92 ±0.09	462 ± 21	120 ± 11	2.51 ±0.58	291 ±171
P1/5	2871E	11.3 ±0.1	7.4 ±0.1	1392 ± 37	1389 ± 37	9.36 ±1.98	1390 ±1
P1/4	2871D	10.0 ±0.1	10.3 ±0.1	969 ± 31	973 ± 31	10.2 ±0.20	971 ±2
P1/3	2871C	120.7 ±3.0	127.9 ±2.6	312 ± 18	505 ± 22	124.3 ±3.6	408 ±96
P1/2	2871B	1020 ±30	1250 ±40	250 ± 16	283 ± 17	1140 ±110	266 ±17
P1/1	2871A	1350±35	1793 ±45	356 ± 19	364 ± 19	1570 ±220	360 ±4
P2/7	2872G	2.02 ±0.05	1.92 ±0.05	374 ± 19	327 ± 18	1.97 ±0.05	351 ±23
P2/6	2872F	1.65 ±0.02	1.06 ±0.02	1698 ± 41	748 ± 27	1.36 ±0.29	1223 ±475
P2/5	2872E	85.5 ±2.7	58.6 ±1.2	210 ± 14	536 ± 23	72.0 ±13.4	373 ±163
P2/4	2872D	10 ±0.2	10.8 ±0.1	414 ± 20	1117 ± 33	10.4 ±0.4	766 ±352
P2/3	2872C	35.8 ±1.2	580 ±20	175 ± 13	235 ± 15	310 ±270	205 ±30
P2/2	2872B	699.5 ±6.4	1210±20	2224 ± 47	651 ± 26	950±250	1438 ±787

P2/1	2872A	214 ±7.4	369 ±6.2	165 ± 13	616 ± 25	290 ±80	390 ±225
P3/4	2873D	1.61 ±0.03	1.25 ±0.02	1010 ± 32	791 ± 28	1.43 ±0.18	901 ±110
P3/3	2873C	1.21 ±0.01	1.11 ±0.02	1806 ± 42	592 ± 24	1.16 ±0.05	1199 ±607
P3/2	2873B	1.32 ±0.03	0.97 ±0.02	559 ± 24	588 ± 24	1.15 ±0.18	574 ±14
P3/1	2873A	268.4 ±2.7	221.9 ±4.1	1868 ± 43	572 ± 24	245 ±23	1220 ±648
P4/4	2874D	22.1 ±0.34	170 ±5	800 ± 28	269 ± 16	97±74	535 ±266
P4/3	2874C	3.53 ±0.13	2.42 ±0.04	159 ± 13	819 ± 29	2.98 ±0.56	489 ±330
P4/2	2874B	155±3	150 ±5	641 ± 25	844 ± 29	150 ±3	743 ±101
P4/1	2874A	980±15	830 ±15	848 ± 29	632 ± 25	900 ±70	740 ±108
P5/20	2875T	0.11 ±0.01	0.11 ±0.01	279 ± 17	397 ± 20	0.11 ±0.01	338 ±59
P5/19	2875S	0.10 ±0.01	0.06 ±0.01	772 ± 28	1306 ± 36	0.08 ±0.02	1039 ±267
P5/18	2875R	0.14 ±0.01	0.16 ±0.01	532 ± 23	326 ± 18	0.15 ±0.01	429 ±103
P5/17	2875Q	0.18 ±0.01	0.26 ±0.01	996 ± 32	313 ± 18	0.22 ±0.04	654 ±342
P5/16	2875P	0.21 ±0.01	0.18 ±0.01	566 ± 24	830 ± 29	0.20 ±0.01	698 ±132
P5/15	2875O	0.42 ±0.01	0.59 ±0.02	587 ± 24	525 ± 23	0.51 ±0.08	556 ±31
P5/14	2875N	0.59 ±0.01	0.52 ±0.03	798 ± 28	165 ± 13	0.55 ±0.03	481 ±317
P5/13	2875M	0.60 ±0.02	0.42 ±0.01	528 ± 23	761 ± 28	0.51 ±0.09	645 ±117

P5/12	2875L	0.62 ±0.01	0.63 ±0.02	665 ± 26	493 ± 22	0.63 ±0.01	579 ±86
P5/11	2875K	0.68 ±0.02	0.78 ±0.02	631 ± 25	693 ± 26	0.73 ±0.05	662 ±31
P5/10	2875J	0.83 ±0.02	0.76 ±0.03	466 ± 22	254 ± 16	0.80 ±0.03	360 ±106
P5/9	2875I	1.42 ±0.03	0.73 ±0.02	648 ± 25	690 ± 26	1.08 ±0.34	669 ±21
P5/8	2875H	0.65 ±0.02	0.86 ±0.02	595 ± 24	626 ± 25	0.76 ±0.11	611 ±16
P5/7	2875G	1.23 ±0.03	1.17 ±0.03	422 ± 21	582 ± 24	1.20 ±0.03	502 ±80
P5/6	2875F	1.74 ±0.04	0.96 ±0.02	443 ± 21	839 ± 29	1.35 ±0.39	641 ±198
P5/5	2875E	1.01 ±0.03	0.93 ±0.01	410 ± 20	1103 ± 33	0.97 ±0.04	756 ±347
P5/4	2875D	0.94 ±0.01	1.51 ±0.05	1396 ± 37	290 ± 17	1.22 ±0.28	843 ±553
P5/3	2875C	1.79 ±0.06	1.21 ±0.03	267 ± 16	618 ± 25	1.50 ±0.29	443 ±176
P5/2	2875B	1.51 ±0.06	0.92 ±0.02	178 ± 13	495 ± 22	1.21 ±0.3	336 ±158
P5/1	2875A	1.00 ±0.02	1.22 ±0.02	572 ± 24	720 ± 27	1.11 ±0.11	646 ±74

Table 4-2: IRSL screening measurements on paired aliquots of 90-250µm 15% HF-etched 'polymineral'

SUTL no.	Field ID	Stored dose / Gy		Sensitivity / photon counts Gy^{-1}		/ Gy	/ photon counts Gy^{-1}
		Aliquot 1	Aliquot 2	Aliquot 1	Aliquot 2	Mean	
P1/9	2871I	275 ± 12	1939 ±140	3355 ± 58	767 ± 28	1107 ±832	2061 ±1294
P1/8	2871H	1455 ±157	1341 ±104	437 ± 21	778 ± 28	1398 ± 57	607 ± 171
P1/7	2871G	129 ± 8	146 ± 87	884 ± 30	1225 ± 35	137 ± 8	1055 ± 170
P1/6	2871F	6.2 ± 0.1	7.2 ± 0.2	6623 ± 81	4842 ± 70	6.7 ± 0.5	5733 ± 890
P1/5	2871E	39.1 ± 0.9	10.2 ± 0.2	5383 ± 73	4529 ± 67	25 ± 15	4956 ± 427
P1/4	2871D	2.5 ± 0.2	2.9 ± 0.2	1132 ± 34	687 ± 26	2.7 ± 0.2	909 ± 223
P1/3	2871C	1.2 ± 0.1	4.9 ± 0.3	898 ± 30	890 ± 30	3.1 ± 1.8	894 ± 4
P1/2	2871B	0.9 ± 0.1	0.4 ± 0	595 ± 24	1634 ± 40	0.6 ± 0.3	1114 ± 519
P1/1	2871A	1.8 ± 0.3	0.5 ± 0.1	348 ± 19	872 ± 30	1.2 ± 0.6	610 ± 262
P2/7	2872G	172 ± 15	366 ± 17	612 ± 25	1787 ± 42	268.6 ± 97	1200 ± 587
P2/6	2872F	916 ± 24	1246 ± 49	4492 ± 67	2146 ± 46	1081 ±165	3319 ±1173
P2/5	2872E	71.6 ± 5.9	561 ± 39	678 ± 26	851 ± 29	316 ± 245	764 ± 87
P2/4	2872D	8.2 ± 0.3	22.6 ± 0.7	2125 ± 46	2780 ± 53	15.4 ± 7.2	2453 ± 327
P2/3	2872C	19.4 ± 1.1	213.9 ± 10	1151 ± 34	1495 ± 39	117 ± 97	1323 ± 172
P2/2	2872B	1.2 ± 0.1	1.2 ± 0.1	4322 ± 66	1423 ± 38	1.2 ± 0.1	2872 ±1450
P2/1	2872A	2.7 ± 0.2	2.5 ± 0.2	771 ± 28	950 ± 31	2.6 ± 0.1	861 ± 89

P3/4	2873D	300 ± 9	94.5 ± 3.1	3683 ± 61	2590 ± 51	197 ± 103	3136 ± 547
P3/3	2873C	2 ± 0.1	1.5 ± 0.1	1728 ± 42	1816 ± 43	1.7 ± 0.3	1772 ± 44
P3/2	2873B	1.6 ± 0.1	1.4 ± 0.1	3066 ± 55	1199 ± 35	1.5 ± 0.1	2132 ± 934
P3/1	2873A	1.9 ± 0.1	1.9 ± 0.1	2288 ± 48	2590 ± 51	1.9 ± 0	2439 ± 151
P4/4	2874D	1104 ± 56	1065 ± 63	1404 ± 37	1088 ± 33	1084 ± 20	1246 ± 158
P4/3	2874C	189 ± 9	215 ± 10	1480 ± 38	1545 ± 39	202 ± 13	1513 ± 32
P4/2	2874B	3.6 ± 0.3	2.6 ± 0.1	832 ± 29	2155 ± 46	3.1 ± 0.5	1494 ± 662
P4/1	2874A	12.9 ± 0.5	132 ± 7	2610 ± 51	1015 ± 32	72 ± 60	1812 ± 797
P5/20	2875T	1.3 ± 0.1	1.3 ± 0.1	1007 ± 32	2389 ± 49	1.3 ± 0.1	1698 ± 691
P5/19	2875S	2.6 ± 0.3	1.0 ± 0.1	544 ± 23	870 ± 29	1.8 ± 0.8	707 ± 163
P5/18	2875R	1.4 ± 0.1	1.6 ± 0.1	1107 ± 33	1291 ± 36	1.5 ± 0.1	1199 ± 92
P5/17	2875Q	1.2 ± 0.1	2.4 ± 0.2	1762 ± 42	555 ± 24	1.8 ± 0.6	1159 ± 604
P5/16	2875P	1.4 ± 0.1	1.0 ± 0.1	671 ± 26	2078 ± 46	1.2 ± 0.2	1375 ± 704
P5/15	2875O	3.1 ± 0.2	1.1 ± 0.1	917 ± 30	1416 ± 38	2.1 ± 1.0	1167 ± 249
P5/14	2875N	1.8 ± 0.1	1.3 ± 0.1	796 ± 28	1312 ± 36	1.6 ± 0.2	1054 ± 258
P5/13	2875M	1.0 ± 0.1	1.4 ± 0.1	1117 ± 33	1141 ± 34	1.2 ± 0.2	1129 ± 12
P5/12	2875L	6.8 ± 0.3	0.9 ± 0.1	1898 ± 44	1197 ± 35	3.9 ± 2.9	1548 ± 350

P5/11	2875K	1.5 ± 0.1	1.4 ± 0.1	846 ± 29	649 ± 25	1.4 ± 0.1	748 ± 98
P5/10	2875J	1.0 ± 0.1	0.9 ± 0.1	1410 ± 38	1532 ± 39	1.0 ± 0.1	1471 ± 61
P5/9	2875I	1.2 ± 0.1	1.0 ± 0.1	1298 ± 36	1148 ± 34	1.1 ± 0.1	1223 ± 75
P5/8	2875H	1.2 ± 0.1	0.8 ± 0.1	962 ± 31	2142 ± 46	1.0 ± 0.2	1552 ± 590
P5/7	2875G	0.9 ± 0.1	1.2 ± 0.1	1286 ± 36	520 ± 23	1.1 ± 0.1	903 ± 383
P5/6	2875F	0.6 ± 0.1	1.2 ± 0.1	1173 ± 34	1007 ± 32	0.9 ± 0.3	1090 ± 83
P5/5	2875E	0.7 ± 0.1	0.5 ± 0.1	889 ± 30	1639 ± 40	0.6 ± 0.1	1264 ± 375
P5/4	2875D	0.4 ± 0.1	0.7 ± 0.1	1965 ± 44	1079 ± 33	0.6 ± 0.2	1522 ± 443
P5/3	2875C	0.3 ± 0.1	0.8 ± 0.1	1418 ± 38	847 ± 29	0.6 ± 0.2	1132 ± 285
P5/2	2875B	0.3 ± 0.1	0.2 ± 0.1	2330 ± 48	1796 ± 42	0.3 ± 0.1	2063 ± 267
P5/1	2875A	0.4 ± 0.1	0.6 ± 0.1	794 ± 28	693 ± 26	0.5 ± 0.1	744 ± 51

Table 4-3: post-IRSL OSL screening measurements on paired aliquots of 90-250µm 15% HF-etched 'polymineral'

SUTL no.	Field ID	Stored dose / Gy		Sensitivity / photon counts Gy^{-1}		/ Gy	/ photon counts Gy^{-1}
		Aliquot 1	Aliquot 2	Aliquot 1	Aliquot 2	Mean	

P1/9	2871I	712 ± 22	2644 ±142	2831 ± 18	657 ± 13	1678 ± 66	1744 ±1087
P1/8	2871H	1680 ± 49	1743 ± 94	296 ± 8	769 ± 12	1712 ± 32	532 ± 237
P1/7	2871G	212 ± 14	337 ± 16	720 ± 12	1009 ± 16	274 ± 63	865 ± 144
P1/6	2871F	49 ± 1	47 ± 1	2877 ± 26	2239 ± 23	48 ± 1	2558 ± 319
P1/5	2871E	144 ± 4	35 ± 1	2506 ± 25	2560 ± 24	90 ± 54	2533 ± 27
P1/4	2871D	11 ± 1	43 ± 5	964 ± 15	93 ± 7	27 ± 16	528 ± 435
P1/3	2871C	10 ± 1	30 ± 3	429 ± 10	322 ± 11	20 ± 10	375 ± 53
P1/2	2871B	8.3 ± 0.5	8.5 ± 0.5	549 ± 12	712 ± 11	8.4 ± 0.1	631 ± 82
P1/1	2871A	20 ± 2	10 ± 1	277 ± 6	337 ± 9	15 ± 5	307 ± 30
P2/7	2872G	787 ± 50	441 ± 14	524 ± 11	1943 ± 21	614 ± 173	1234 ± 710
P2/6	2872F	1036 ± 23	1273 ± 38	4640 ± 33	2266 ± 23	1155 ±118	3453 ±1187
P2/5	2872E	162 ± 11	479 ± 35	643 ± 11	431 ± 9	320 ± 158	537 ± 106
P2/4	2872D	78 ± 3	64 ± 2	1174 ± 18	2282 ± 24	71 ± 7	1728 ± 554
P2/3	2872C	95 ± 5	427 ± 14	863 ± 15	2060 ± 22	261 ± 166	1462 ± 599
P2/2	2872B	8.7 ± 0.2	9.0 ± 1	3693 ± 28	1414 ± 19	9.0 ± 0.3	2553 ±1140
P2/1	2872A	35 ± 2	37 ± 2	784 ± 15	751 ± 13	36 ± 1	767 ± 17
P3/4	2873D	344 ± 9	187 ± 8	3138 ± 27	1314 ± 16	266 ± 79	2226 ± 912
P3/3	2873C	24 ± 1	12 ± 1	1382 ± 17	1673 ± 19	18 ± 6	1528 ± 145

P3/2	2873B	8.4 ± 0.2	10 ± 1	3581 ± 30	995 ± 15	9.3 ± 0.9	2288 ±1293
P3/1	2873A	16 ± 1	17 ± 1	1515 ± 20	1652 ± 19	17 ± 0	1583 ± 69
P4/4	2874D	714 ± 25	729 ± 29	1858 ± 21	1478 ± 18	721 ± 8	1668 ± 190
P4/3	2874C	293 ± 10	184 ± 5	2021 ± 22	2571 ± 25	238 ± 55	2296 ± 275
P4/2	2874B	48 ± 4	20 ± 1	320 ± 10	1290 ± 18	34 ± 14	805 ± 485
P4/1	2874A	57 ± 2	108 ± 7	2442 ± 24	534 ± 12	82 ± 26	1488 ± 954
P5/20	2875T	9.1 ± 0.4	11.8 ± 0.4	1095 ± 16	2030 ± 20	10.5 ± 1.3	1563 ± 468
P5/19	2875S	53 ± 3	12.4 ± 0.7	452 ± 11	687 ± 13	32 ± 20	570 ± 118
P5/18	2875R	20 ± 1	14.3 ± 0.6	845 ± 14	1329 ± 19	17.4 ± 3.1	1087 ± 242
P5/17	2875Q	11.2 ± 0.4	21 ± 2	2012 ± 22	516 ± 11	16.2 ± 5.1	1264 ± 748
P5/16	2875P	23.2 ± 1.3	8.0 ± 0.3	610 ± 12	2136 ± 22	15.6 ± 7.6	1373 ± 763
P5/15	2875O	18.8 ± 0.8	11.2 ± 0.4	1337 ± 18	1377 ± 19	15 ± 3.8	1357 ± 20
P5/14	2875N	10.7 ± 0.5	10 ± 0.3	1124 ± 17	2141 ± 21	10.3 ± 0.3	1633 ± 509
P5/13	2875M	9.5 ± 0.4	14.6 ± 0.6	1095 ± 16	1284 ± 18	12.1 ± 2.5	1189 ± 94
P5/12	2875L	48 ± 2	7.0 ± 0.3	1963 ± 21	1252 ± 16	28 ± 21	1608 ± 355
P5/11	2875K	5.8 ± 0.2	10 ± 0.6	1398 ± 17	603 ± 13	7.9 ± 2.1	1001 ± 397
P5/10	2875J	9.1 ± 0.4	10.2 ± 0.4	1440 ± 17	1529 ± 19	9.7 ± 0.6	1484 ± 44

P5/9	2875I	11.6 ± 0.4	4.6 ± 0.2	1629 ± 20	2063 ± 23	8.1 ± 3.5	1846 ± 217
P5/8	2875H	15.1 ± 0.7	7.9 ± 0.3	1104 ± 17	1468 ± 19	11.5 ± 3.6	1286 ± 182
P5/7	2875G	6.3 ± 0.2	4.5 ± 0.3	1670 ± 20	517 ± 10	5.4 ± 0.9	1093 ± 577
P5/6	2875F	5.5 ± 0.2	6.6 ± 0.3	1679 ± 20	1086 ± 17	6.0 ± 0.5	1383 ± 297
P5/5	2875E	13.9 ± 0.5	6.9 ± 0.2	1520 ± 20	2315 ± 24	10.4 ± 3.5	1917 ± 398
P5/4	2875D	4.4 ± 0.1	6.1 ± 0.3	3627 ± 29	1037 ± 16	5.3 ± 0.8	2332 ±1295
P5/3	2875C	5.4 ± 0.2	13.3 ± 0.7	1688 ± 20	705 ± 12	9.3 ± 4.0	1197 ± 491
P5/2	2875B	3.7 ± 0.1	3.6 ± 0.1	2367 ± 24	3193 ± 31	3.7 ± 0.1	2780 ± 413
P5/1	2875A	8.0 ± 0.3	6.3 ± 0.3	1216 ± 17	1213 ± 16	7.2 ± 0.9	1215 ± 2

Table 4-4: post-IRSL TL screening measurements on paired aliquots of 90-250µm 15% HF-etched 'polymineral'

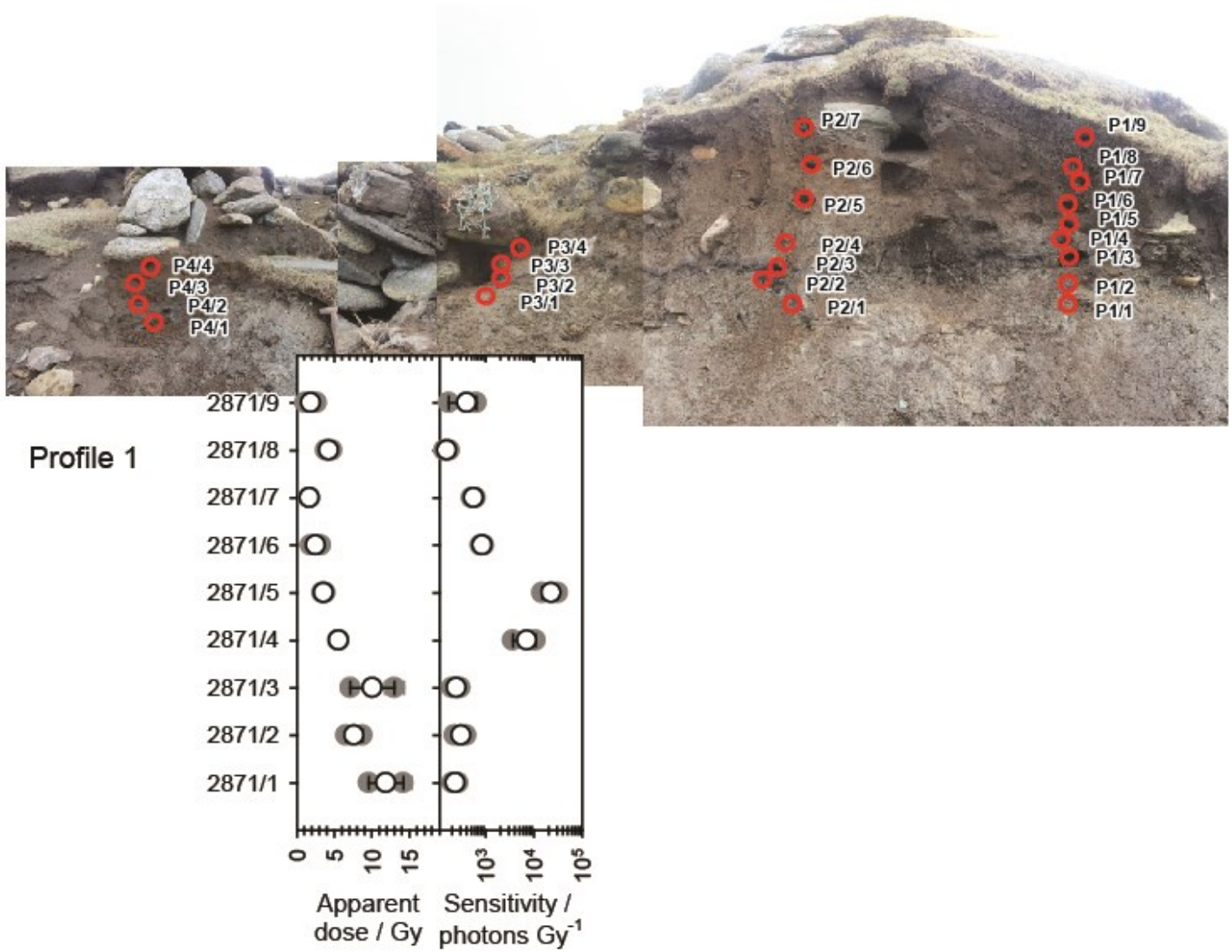

Figure 4-1: P1, Quartz OSL stored dose and sensitivities plotted vs depth

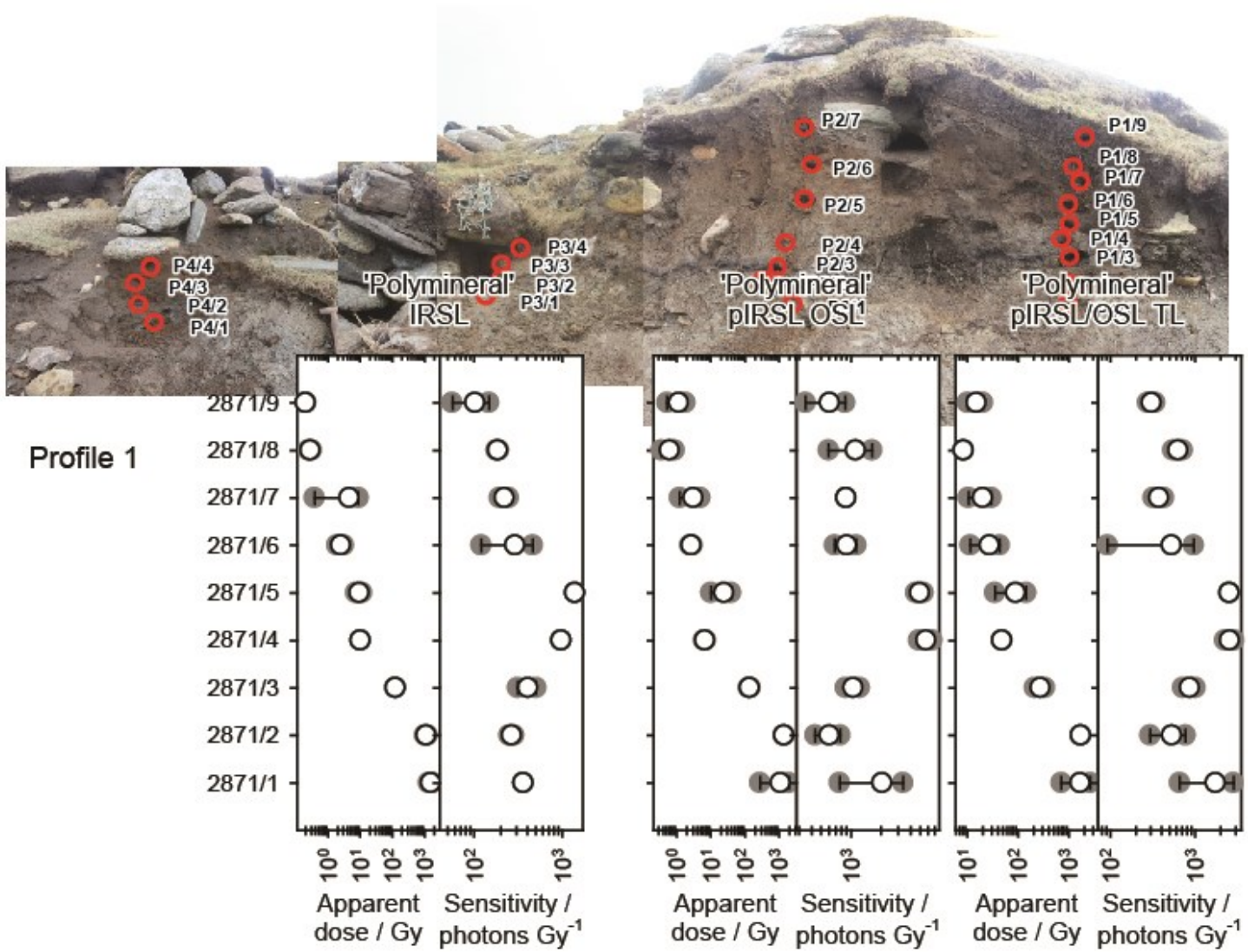

Figure 4-2: P1, Polymineral IRSL-OSL-TL OSL stored dose and sensitivities plotted vs depth

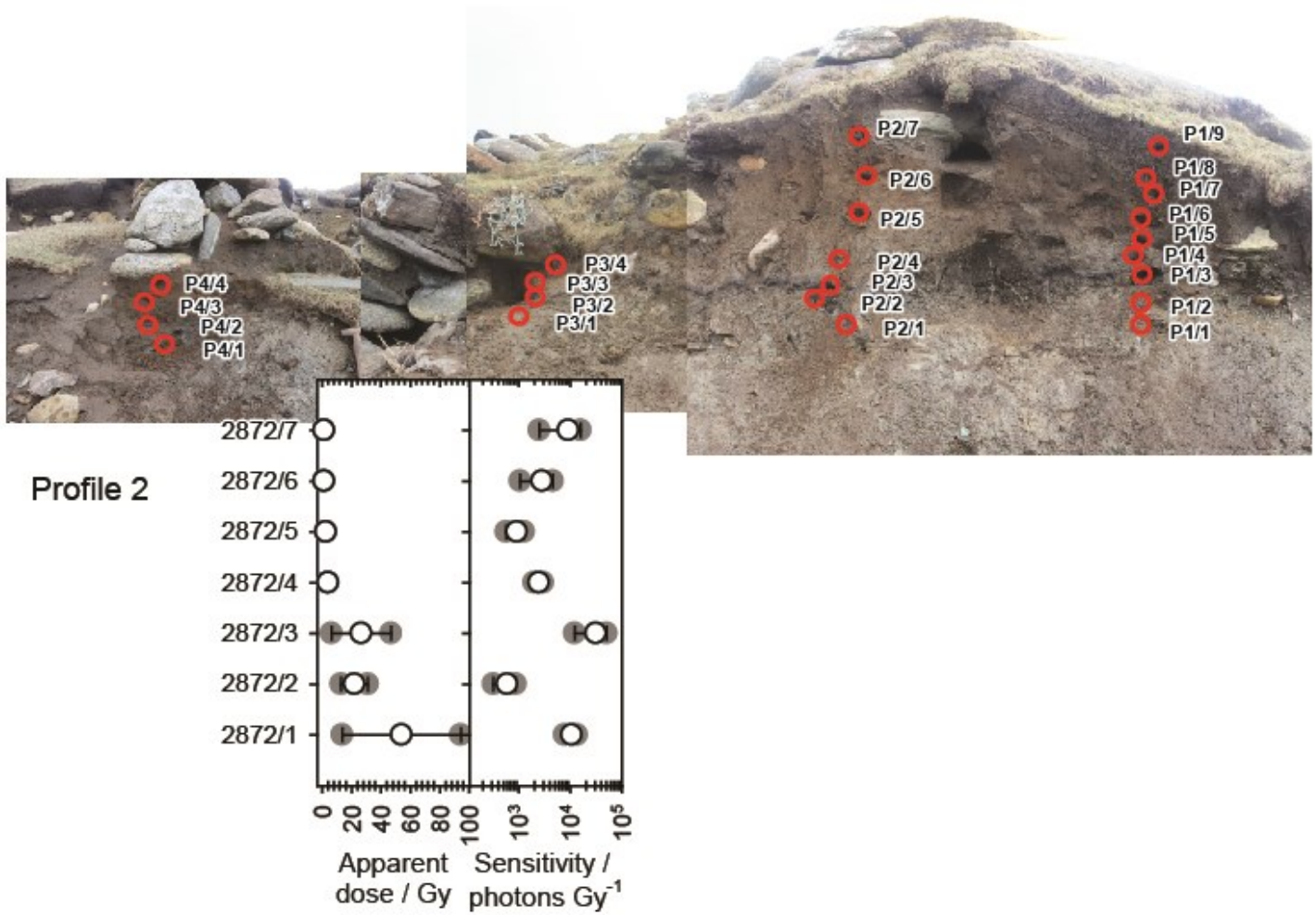

Figure 4-3: P2, Quartz OSL stored dose and sensitivities plotted vs depth

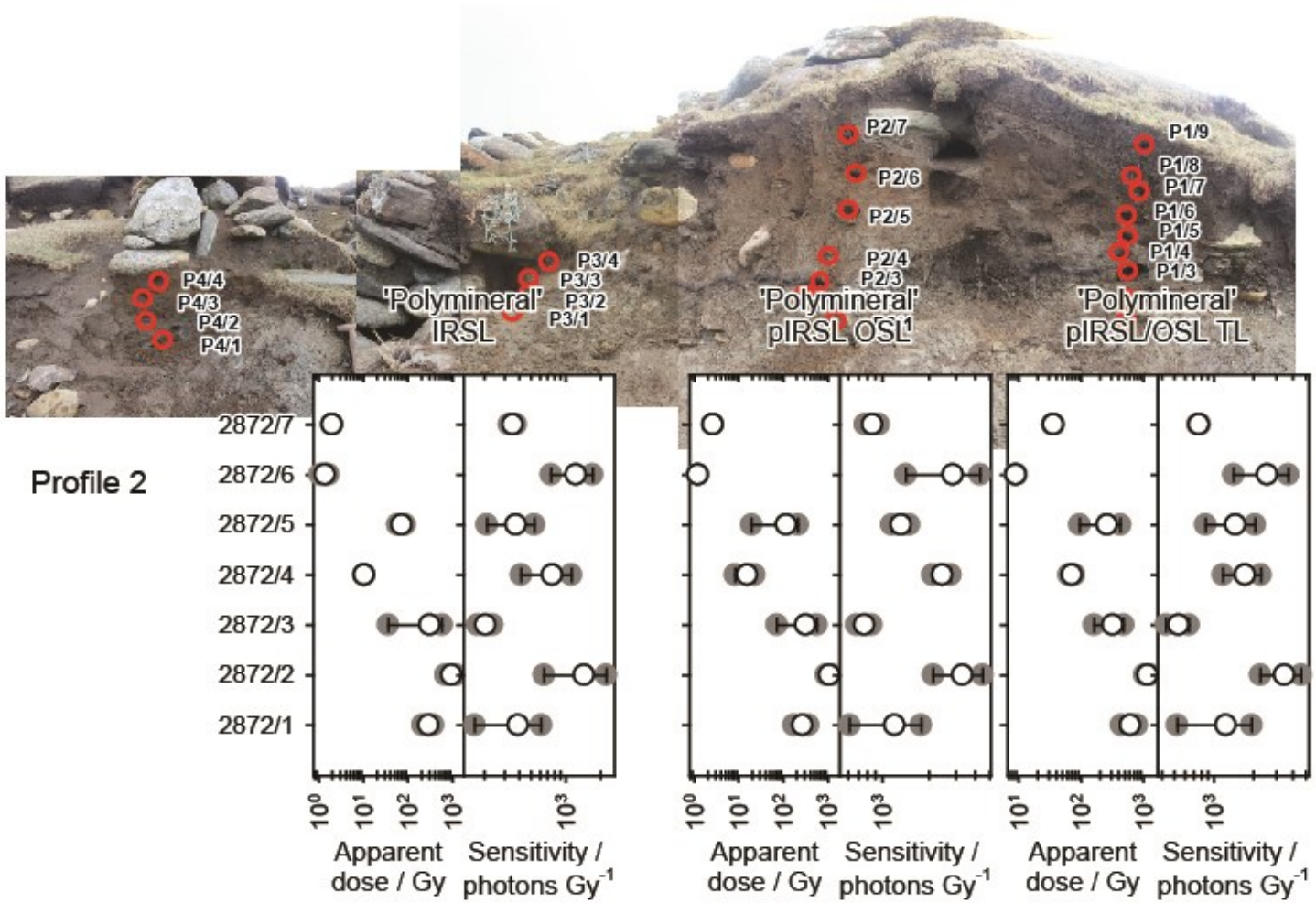

Figure 4-4: P2, Polymineral IRSL-OSL-TL OSL stored dose and sensitivities plotted vs depth

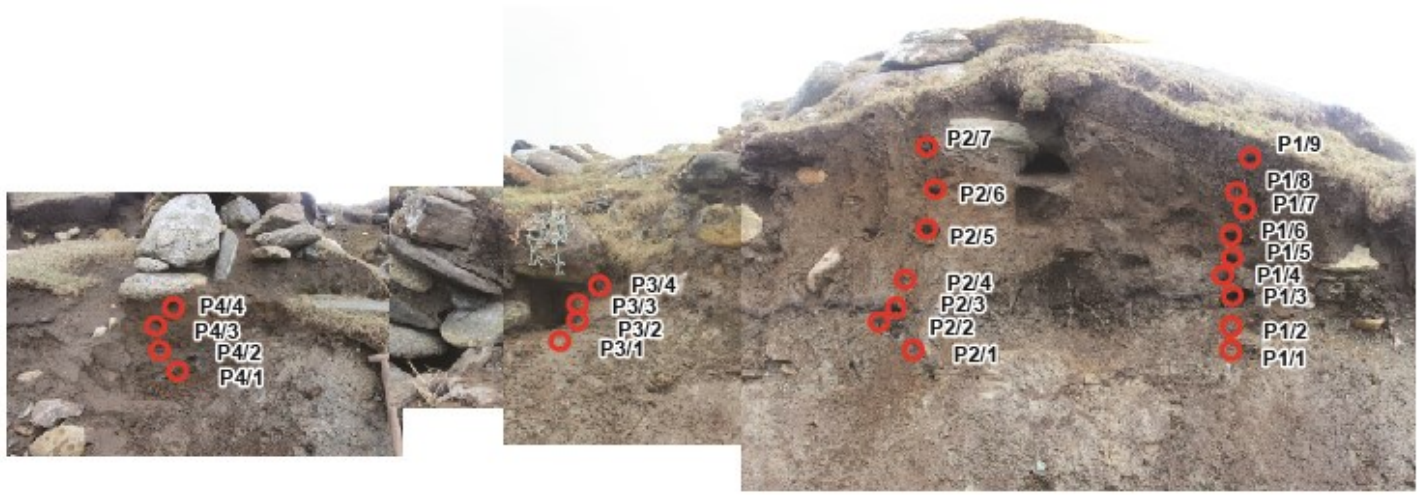

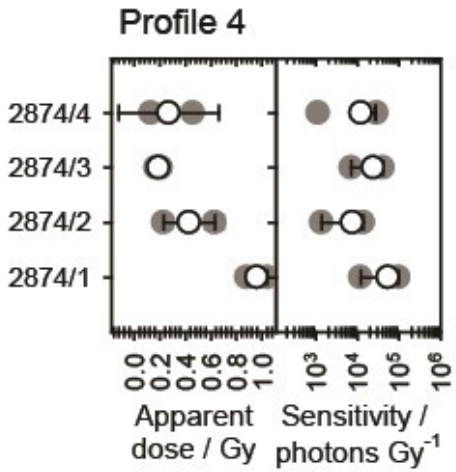

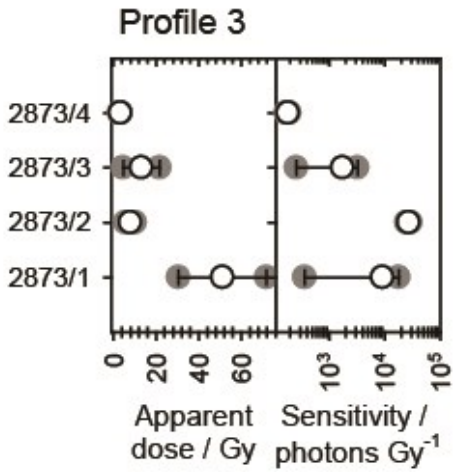

Figure 4-5: P3-4, Quartz OSL stored dose and sensitivities plotted vs depth

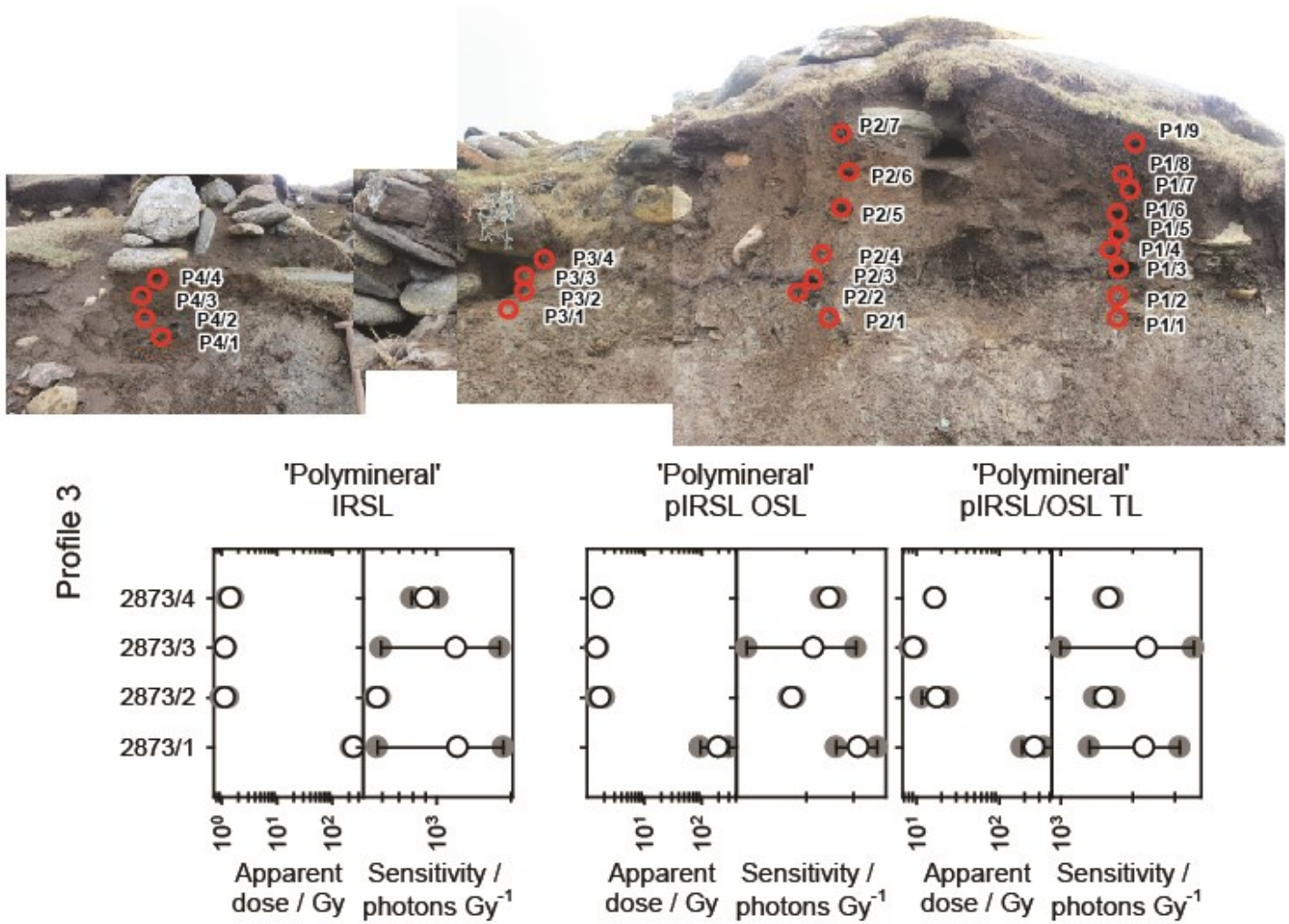

Figure 4-6: P3, Polymineral IRSL-OSL-TL OSL stored dose and sensitivities plotted vs depth

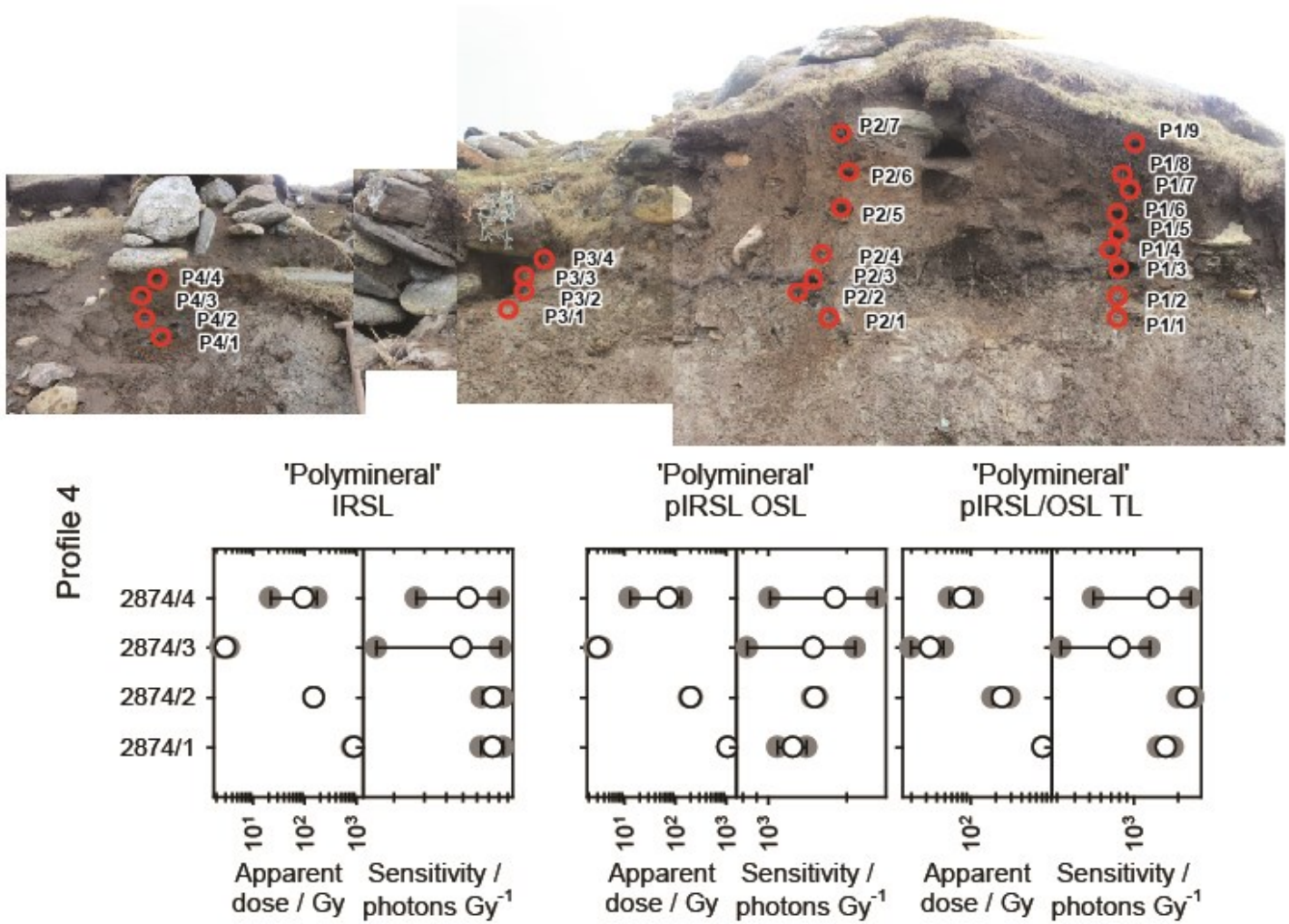

Figure 4-7: P4, Polymineral IRSL-OSL-TL OSL stored dose and sensitivities plotted vs depth

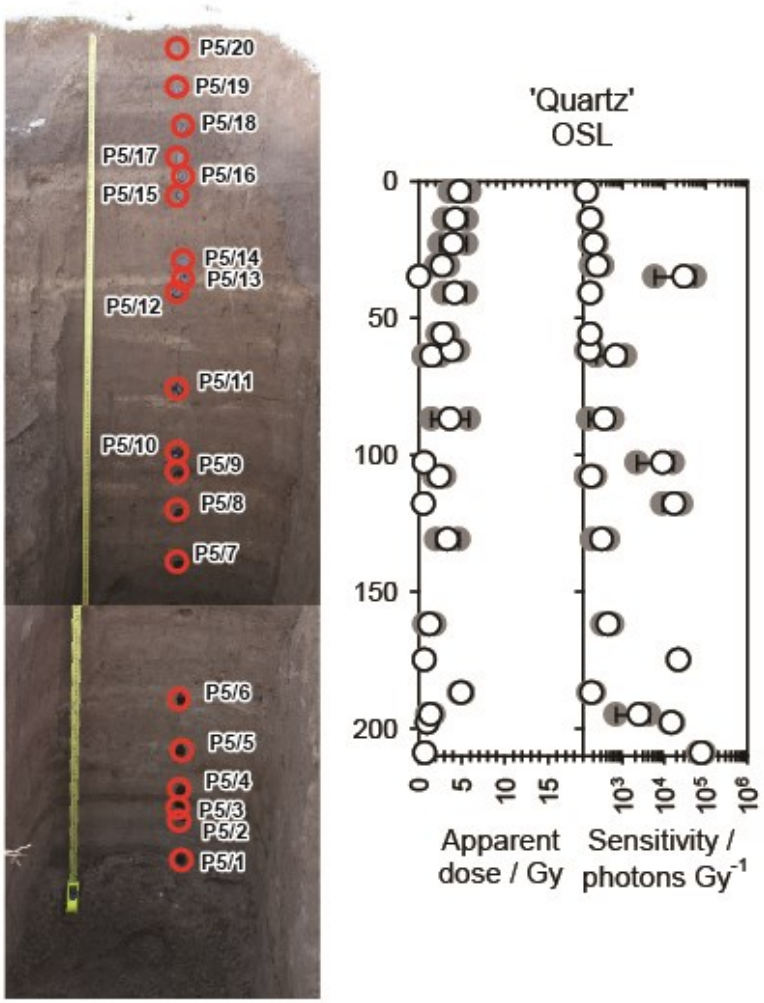

Figure 4-8: P5, Quartz OSL stored dose and sensitivities plotted vs depth

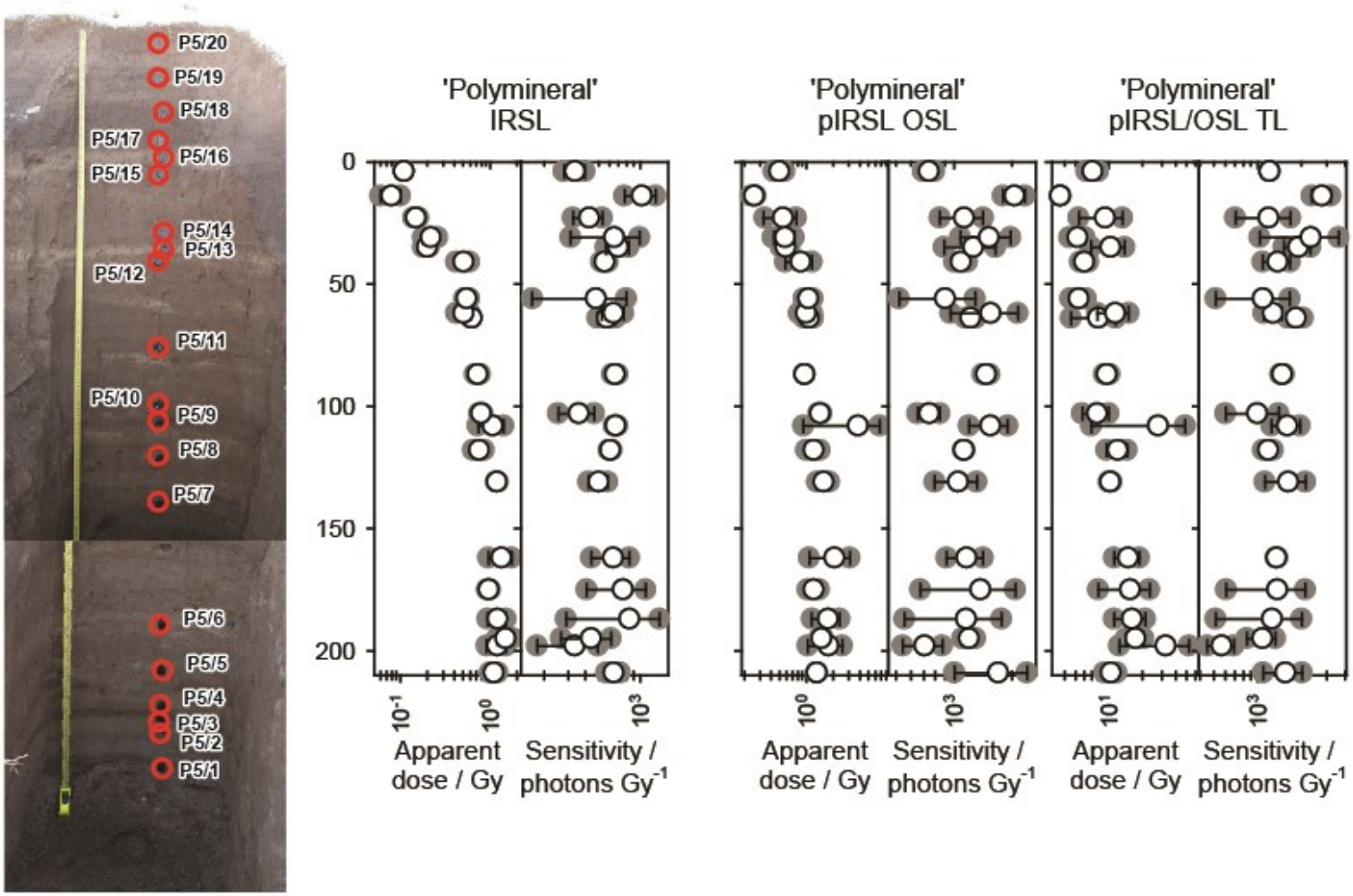

Figure 4-9: P5, Polymineral IRSL-OSL-TL OSL stored dose and sensitivities plotted vs depth

5. Quartz OSL SAR measurements

The preceding sections have highlighted that 1) the longest environmental records are recorded within the substrate stratigraphies to the noosts, 2) that the noosts are of different age, with their underlying sedimentary sequences recording different depositional histories, 3) that the beach section only records the later part of the environmental record. Moreover, these investigations have provided the first indication that the 'till' at the base of the succession, was likely to have been re-worked, or modified, in the waning stages of the last glacial cycle. The dating samples, for which dose rates are also determined, will allow us to test these assumptions. Furthermore, these samples will provide a means to determine periods of sand activity at the noost site, which may relate to periods of climatic instability, TPQ for construction and modification of the noosts, and the temporal framework to assess the environmental/climatic archive as recorded in the beach section.

5.1. Sample preparation

5.1.1. Water contents

Dating materials and bulk sediment samples were weighed, saturated with water and re-weighed. Following oven drying at 50 °C to constant weight, the actual and saturated water contents were determined as fractions of dry weight. These data were used, together with information on field conditions to determine water contents and an associated water content uncertainty for use in dose rate determination.

5.1.2. HRGS and TSBC Sample Preparation

Bulk quantities of material, weighing c. 50g, were removed from each full dating and bulk sediment sample for environmental dose rate determinations. These dried materials were transfer to high-density-polyethylene (HDPE) pots and sealed with epoxy resin for high-resolution gamma spectrometry (HRGS). Each pot was stored for 3 weeks prior to measurement to allow equilibration of ^{222}Rn daughters. A further 20 g of the dried material was used in thick source beta counting (TSBC; Sanderson, 1988).

5.1.3. Quartz mineral preparation

Approximately 20g of material was removed for each tube and processed to obtain sand-sized quartz grains for luminescence measurements. Each sample was wet sieved to obtain the 90-150 and 150-250 µm fractions. Both fractions were treated with 1 M hydrochloric acid (HCl) for 10 minutes, 15% hydrofluoric acid (HF) for 15 minutes, and 1 M HCl for a further 10 minutes. The HF-etched sub-samples were then centrifuged in sodium polytungstate solutions of ~2.51, 2.58, 2.62, and 2.74 gcm^{-3}, to obtain concentrates of potassium-rich feldspars (2.51-2.58 gcm^{-3}), sodium feldspars (2.58-2.62 gcm^{-3}) and quartz plus plagioclase (2.62-2.74 gcm^{-3}). The selected quartz fraction was then subjected to further HF and HCl washes (40% HF for 10 minutes, followed by 1M HCl for 10 minutes).

All materials were dried at 50°C and transferred to Eppendorf tubes. The 40% HF-etched, 2.62-2.74 gcm^{-3} 'quartz' fractions were dispensed to 10mm stainless steel discs for measurement. The purity of which was checked using a Hitachi S-3400N scanning electron microscope (SEM), coupled with an Oxfords Instruments INCA EDX system, to determine approximate elemental concentrations for each sample. 32 aliquots were dispensed for each sample.

5.2. Measurements and determinations

5.2.1. Dose rate determinations

Dose rates were measured in the laboratory using HRGS and TSBC. Full sets of laboratory dose rate determinations were made for all samples.

HRGS measurements were performed using a 50% relative efficiency "n" type hyper-pure Ge detector (EG&G Ortec Gamma-X) operated in a low background lead shield with a copper liner. Gamma ray spectra were recorded over the 30 keV to 3 MeV range from each sample, interleaved with background measurements and measurements from SUERC Shap Granite standard in the same geometries. Sample counts were for 80ks. The spectra were analysed to determine count rates from the major line emissions from ^{40}K (1461 keV), and from selected nuclides in the U decay series (^{234}Th, ^{226}Ra + ^{235}U, ^{214}Pb, ^{214}Bi and ^{210}Pb) and the Th decay series (^{228}Ac, ^{212}Pb, ^{208}Tl) and their statistical counting uncertainties. Net rates and activity concentrations for each of these nuclides were determined relative to Shap Granite by weighted combination of the individual lines for each nuclide. The internal consistency of nuclide specific estimates for U and Th decay series nuclides was assessed relative to measurement precision, and weighted combinations used to estimate mean activity concentrations (Bq kg^{-1}) and elemental concentrations (% K and ppm U, Th) for the parent activity. These data were used to determine infinite matrix dose rates for alpha, beta and gamma radiation.

Beta dose rates were also measured directly using the SUERC TSBC system (Sanderson, 1988). Count rates were determined with six replicate 600 s counts on each sample, bracketed by background measurements and sensitivity determinations using the Shap Granite secondary reference material. Infinite-matrix dose rates were calculated by scaling the net count rates of samples and reference material to the working beta dose rate of the Shap Granite (6.25 ± 0.03 mGy a^{-1}). The estimated errors combine counting statistics, observed variance and the uncertainty on the reference value.

The dose rate measurements were used in combination with the assumed burial water contents, to determine the overall effective dose rates for age estimation. Cosmic dose rates were evaluated by combining latitude and altitude specific dose rates (0.17 ± 0.01 mGy a^{-1}) for the site with corrections for estimated depth of overburden using the method of Prescott and Hutton (1994).

5.2.2. Quartz SAR luminescence measurements

All measurements were conducted using a Risø DA-15 automatic reader equipped with a $^{90}Sr/^{90}Y$ β-source for irradiation, blue LEDs emitting around 470 nm and infrared (laser) diodes emitting around 830 nm for optical stimulation, and a U340 detection filter pack to detect in the region 270-380 nm, while cutting out stimulating light (Bøtter-Jensen et al., 2000).

Initially, equivalent dose determinations were made on sets 32 aliquots per sample, using a single aliquot regeneration (SAR) sequence (cf Murray and Wintle, 2000). Using this procedure, the OSL signal levels from each individual disc were calibrated to provide an absorbed dose estimate (the equivalent dose) using an interpolated dose-response curve, constructed by regenerating OSL signals by beta irradiation in the laboratory. Sensitivity changes which may occur as a result of readout, irradiation and preheating (to remove unstable radiation-induced signals) were monitored using small test doses after each regenerative dose. Each measurement was standardised to the test dose response determined immediately after its readout, to compensate for observed changes in sensitivity during the laboratory measurement sequence. The regenerative doses were chosen to encompass the likely value of the equivalent (natural) dose. A repeat dose point was included to check the ability of the SAR procedure to correct for laboratory-induced sensitivity changes (the 'recycling test'), a zero dose point is included late in the sequence to check for thermally induced charge transfer during the irradiation and preheating cycle (the 'zero cycle'), and an IR response check included to assess the magnitude of non-quartz signals. Regenerative dose response curves were constructed using doses of 0.5, 1, 2.5, 10 and 2.5 Gy, with test doses of 1.5 Gy. The 32 aliquot sets were sub-divided into eight subsets, such that eight preheating regimes were explored - 200°C to 270°C, in 10°C increments.

5.3. Results of Quartz OSL SAR measurements

5.3.1. Dose rates

HRGS results are shown in Table 5-1, both as activity concentrations (i.e. disintegrations per second per kilogram) and as equivalent parent element concentrations (in % and ppm), based in the case of U and Th on combining nuclide specific data assuming decay series equilibrium.

K concentrations ranged between 0.6 and 1.1 % (with a mean of 0.8 ± 0.3% (stdev)), U concentrations between 0.8 and 1.2 ppm (mean, 0.9 ± 0.3 ppm) and Th concentrations between 1.2 and 4.1 (mean, 2.6 ± 1.5 ppm). By site, the range in concentrations was less variable: for the noost sections, the mean values were K- 0.9 ± 0.3 %, U- 1.0 ± 0.2 ppm and Th- 2.9 ± 0.2 ppm; and for the beach section, K- 0.6 ± 0.1 %, U- 0.6 ± 0.6 ppm and Th- 1.6 ± 0.1 ppm.

SUTL no.	Activity Concentration[a] / Bq kg^{-1}			Equivalent Concentration[b]		
	K	U	Th	K / %	U / ppm	Th / ppm
2861a	276 ± 32	13.3 ± 1.6	8.9 ± 1.5	0.89 ± 0.10	1.08 ± 0.13	2.18 ± 0.36
2861b	211 ± 24	13.6 ± 5	13 ± 4.8	0.68 ± 0.08	1.10 ± 0.40	3.21 ± 1.17
2862	189 ± 34	9.3 ± 2.4	5.0 ± 1.4	0.61 ± 0.11	0.75 ± 0.19	1.23 ± 0.35
2863	332 ± 35	14.2 ± 1.7	16.8 ± 1.5	1.07 ± 0.11	1.15 ± 0.14	4.13 ± 0.37
2864	274 ± 33	14.9 ± 2.2	10.9 ± 1.4	0.89 ± 0.11	1.21 ± 0.18	2.69 ± 0.36
2865	242 ± 32	11.8 ± 1.6	8.8 ± 1.4	0.78 ± 0.10	0.95 ± 0.13	2.16 ± 0.35
2866	182 ± 39	11.2 ± 4	10 ± 1.4	0.59 ± 0.13	0.91 ± 0.33	2.47 ± 0.36
2867	255 ± 32	9.7 ± 1.6	7 ± 1.4	0.82 ± 0.10	0.79 ± 0.13	1.72 ± 0.35
2868	209 ± 12	6.1 ± 1.7	6.8 ± 1.7	0.68 ± 0.04	0.50 ± 0.14	1.67 ± 0.42

2869	169 ± 13	10.5 ± 1.7	5.8 ± 1.7	0.55 ± 0.04	0.85 ± 0.14	1.42 ± 0.41
2870	181 ± 12	4.1 ± 1.7	6.4 ± 1.6	0.58 ± 0.04	0.33 ± 0.14	1.59 ± 0.39

Table 5-1: Activity and equivalent concentrations of K, U and Th determined by HRGS

[a]Shap granite reference, working values determined by David Sanderson in 1986, based on HRGS relative to CANMET and NBL standards.

[b]Activity and equivalent concentrations for U, Th and K determined by HRGS (Conversion factors based on NEA (2000) decay constants): 40K: 309.3 Bq kg^{-1} $\%K^{-1}$, 238U: 12.35 Bq kg^{-1} $ppmU^{-1}$, 232Th: 4.057 Bq kg^{-1} ppm Th^{-1}

Infinite matrix alpha, beta and gamma dose rates from HRGS are listed for all samples in Table 5-2, together with infinite matrix beta dose rates from TSBC and field gamma dose rates from FGS. Beta dose rates from HRGS ranged between 0.6 and 1.2 mGy a^{-1} (with mean values of 0.9 ± 0.3 mGy a^{-1}). The beta dose rates measured by TSBC ranged between 0.6 and 1.4 mGy a^{-1}, with a mean of 0.9 ± 0.2 mGy a^{-1}. Gamma dose rates from HRGS ranged from 0.3 and 0.6 mGy a^{-1} (with a mean value of 0.4 ± 0.2 mGy a^{-1}). Wet gamma dose rates were measured in situ by FGS for each of the dating positions, with values ranging between 0.3 and 0.4 mGy a^{-1}, with a mean of 0.3 ± 0.1 mGy a^{-1}.

SUTL no.	HRGS, dry[a] / mGy a^{-1}			TSBC, dry / mGy a^{-1}	FGS, wet / mGy a^{-1}
	Alpha	Beta	Gamma		
2861a	4.61 ± 0.45	0.96 ± 0.09	0.45 ± 0.03	0.88 ± 0.07	0.31 ± 0.02
2861b	5.43 ± 1.41	0.82 ± 0.09	0.46 ± 0.08	-	-
2862	3.00 ± 0.60	0.65 ± 0.10	0.30 ± 0.04	0.68 ± 0.07	0.25 ± 0.02
2863	6.26 ± 0.47	1.18 ± 0.10	0.60 ± 0.04	1.36 ± 0.08	0.36 ± 0.02
2864	5.35 ± 0.56	0.99 ± 0.09	0.49 ± 0.04	0.99 ± 0.07	0.34 ± 0.02
2865	4.25 ± 0.44	0.85 ± 0.09	0.41 ± 0.03	1.05 ± 0.07	0.44 ± 0.02
2866	4.34 ± 0.95	0.69 ± 0.12	0.37 ± 0.05	1.07 ± 0.06	0.41 ± 0.02
2867	3.45 ± 0.44	0.85 ± 0.09	0.38 ± 0.03	0.93 ± 0.06	0.36 ± 0.02
2868	2.61 ± 0.50	0.68 ± 0.04	0.31 ± 0.03	0.78 ± 0.06	-
2869	3.41 ± 0.49	0.62 ± 0.04	0.30 ± 0.03	0.77 ± 0.06	-
2870	2.09 ± 0.49	0.58 ± 0.04	0.26 ± 0.03	0.63 ± 0.06	-

Table 5-2: Infinite matrix dose rates determined by HRGS and TSBC

[a]based on dose rate conversion factors in Aikten (1983) and Sanderson (1987)

The water content measurements are given in Table 5-3, together with the assumed values for the average water content during burial. Field (ranging from 7 - 23 % of dry weight) and saturated (22 - 27 % of dry weight) water contents were determined from all samples in the laboratory, with working values between 16 and 20 % adopted for effective dose rate evaluation. Effective dose rates to the HF-etched 200[b] µm quartz grains are given in table 5-3 (the mean of the TSBC and HRGS data, accounting for water content and grain size), together with the estimate of the gamma dose rate (the mean of the FGS and HRGS data, accounting for water content).

SUTL no.	Water contents / %			Effective Dose Rate[a] / mGy a^{-1}		
	Field	Sat	Assumed	Beta[b]	Gamma	Total[b,d]
2861	22.9	26.3	19.5 ± 5	0.67 ± 0.09	0.34 ± 0.04	1.14 ± 0.10
2862	7.4	24.1	16 ± 8	0.67 ± 0.12	0.25 ± 0.02	0.90 ± 0.11
2863	19.6	25.6	19.5 ± 5	0.92 ± 0.10	0.43 ± 0.04	1.47 ± 0.11
2864	12.6	25.0	19 ± 5	0.72 ± 0.09	0.37 ± 0.04	1.22 ± 0.10
2865	15.6	27.1	19 ± 5	0.70 ± 0.09	0.39 ± 0.04	1.23 ± 0.10
2866	19.7	21.9	19 ± 5	0.64 ± 0.10	0.36 ± 0.05	1.14 ± 0.11
2867	15.1	22.6	19 ± 5	0.65 ± 0.09	0.34 ± 0.04	1.13 ± 0.09
2868	9.5	24.1	17 ± 6	0.55 ± 0.04	0.26 ± 0.03	0.92 ± 0.05
2869	11.8	21.9	17 ± 6	0.52 ± 0.04	0.25 ± 0.03	0.90 ± 0.05
2870	11.3	23.9	17 ± 6	0.46 ± 0.04	0.22 ± 0.03	0.82 ± 0.05

Table 5-3: Effective beta and gamma dose rates following water correction.

[a] Effective beta dose rate combining water content corrections with inverse grain size attenuation factors obtained by weighting the 200[b] µm attenuation factors of Mejdahl (1979) for K, U, and Th by the relative beta dose contributions for each source determined by Gamma Spectrometry;

[d] includes a cosmic dose contribution

Effective beta dose rates ranged between 0.5 and 0.9 mGy a^{-1}, and the effective gamma dose rates between 0.2 and 0.4 mGy a^{-1}. Total effective dose rates to quartz ranged between 0.8 and 1.5 mGy a^{-1}.

5.3.2. Quartz single aliquot equivalent dose determinations

For equivalent dose determination, data from single aliquot regenerative dose measurements were analysed using the Risø TL/OSL Viewer programme to export integrated summary files that were analysed in MS Excel and SigmaPlot. Composite dose response curves were constructed from selected discs and when possible, for each of the eight preheating groups from each sample, and used to estimate equivalent dose values for each individual disc and their combined sets. Dose response curves for each of the eight preheating temperature groups and the combined data were determined using either a fit to exponential function or a linear (Appendix B). There was no evidence of significant differences in normalised OSL ratios (both in natural and regenerated dose points) between subsets of discs pre-heated at temperatures from 200°C to 270°C). Accordingly composite dose response curves from selected discs for each sample were constructed and used to estimate equivalent dose values for each individual discs and their combined sets.

Equivalent dose distributions were appraised on a sample by sample basis, and between associated samples, using conventional statistics and kernel density probability and Abanico plotting methods (see appendix B). For 5 out of the 10 samples, the equivalent dose distributions were moderately tight, with a dominant dose population centred around the weighted and robust means, with the former used to determine the equivalent dose (Table 5-4; Appendix B). A further 3 samples of the samples were characterised by slightly more heterogeneous distributions, but again with a dominant central tendency, coincident with the weighted and robust means (Table 5-4; Appendix B). 2 out of the 10 samples, were characterised by broad, heterogeneous distributions which represent mixed age materials; for these the weighted and robust means were discordant (Table 5-4; Appendix B). Comments on the individual equivalent dose distributions are provided in table 5-4, together with the weighted and robust mean combinations, with the respective standard deviations and standard errors listed. In the instances that the equivalent dose distributions are relatively tight, the standard error was used in the subsequent age determinations. Both are presented in the tables 5-4 and 5-5 for convenience.

SUTL no.	n	Comments on apparent age distribution / individual samples	Comments on apparent age distribution / associated samples	Weighted Mean	Robust Mean
2861 (OSL1)	17†/32	dominant population centred around 3.7 Gy (>75% of aliquots), although with both lower (c. 1.5 Gy, 12.5%) and higher dose outliers (c.7.2-8.0 Gy; 12.5%)	associated with SUTL2863 (OSL3); combined, dominant population between 3.4 to 3.9 Gy, although with individual aliquots which tail to higher apparent doses (> 7.5 Gy)	3.66 ± 0.20 (0.10)	3.55 ± 0.67 (0.17)
2862	-/32	normalised natural OSL signals / normalised zero dose OSL signals indistinguishable	SUTL2862 < SUTL2861 and SUTL2864-2867	0.11 ± 0.05 (0.05)	0.14 ± 0.11 (0.04)
2863 (OSL3)	29†/32	dominant population centred around 4.0 Gy (c. 80% of aliquots), although with both lower (c. 2.2-2.3 Gy, ~10%) and higher dose outliers (> 7.5 Gy, ~10%)	SUTL2863 < 2864 < 2865; associated with SUTL2861 (OSL1); combined, dominant population between 3.4 to 3.9 Gy, although with individual aliquots which tail to higher apparent doses (> 7.5 Gy)	2.92 ± 0.21 (0.05)	3.31 ± 0.68 (0.17)
2864 (OSL4)	32†/32	dominant population centred around 1.0 Gy (> 80% of aliquots), although with individual aliquots which tail to lower apparent doses (0.5 - 0.6 Gy, <20%)	SUTL2863 < 2864 < 2865	0.77 ± 0.05 (0.02)	0.88 ± 0.26 (0.05)
2865 (OSL5)	26†/32	bimodal distribution, dominant population at 1.4 to 1.6 Gy (70% of aliquots), subordinate population at 0.8 to 0.9 Gy (30%)	SUTL2863 < 2864 < 2865; dominant population (measured to good precision) with weighted mean at 1.4 ± 0.1 Gy (A); subordinate population (with large errors) at 0.8 ± 0.2 Gy (B)	A: 1.35 ± 0.12 (0.05) **B: 0.79 ± 0.12 (0.09)**	1.47 ± 0.39 (0.1)

2866 (OSL6)	18?/32	complex, heterogeneous distribution, spanning from 0.3 to >7.0 Gy		0.54 ± 0.36 (0.05)	2.10 ± 2.27 (0.61)
2867 (OSL7)	26†/32	dominant population centred around 0.9 Gy c. 80% of aliquots), although with both lower (c. 0.3-0.4 Gy, c. 10%) and higher dose outliers (> 4 Gy; c.10 %)		0.92 ± 0.20 (0.03)	0.97 ± 0.31 (0.09)
2868 (OSL8)	22†/32	complex, heterogeneous distribution, spanning from 0.5 to > 1.0 Gy; some clustering at 0.7 to 0.9 Gy	SUTL2868 > 2869 > 2870	0.64 ± 0.03 (0.03)	0.65 ± 0.1 (0.02)
2869 (OSL9)	24†/32	complex, heterogeneous distribution, spanning from 0.3 to > 1.0 Gy; some clustering at 0.4 to 0.5 Gy (>75% of aliquots)	SUTL2868 > 2869 > 2870	0.47 ± 0.03 (0.02)	0.47 ± 0.1 (0.02)
2870 (OSL10)	24†/32	complex, heterogeneous distribution, spanning from 0.2 to > 0.7 Gy; some clustering around 0.3 Gy	SUTL2868 > 2869 > 2870	0.25 ± 0.01 (0.01)	0.30 ± 0.07 (0.01)

Table 5-4: Comments on equivalent dose distributions of SUTL2861 to SUTL2870; preferred estimates in bold

errors stated: ± weighted standard deviation (weighted error)

5.3.3. Age determinations

The total dose rate is determined from the sum of the equivalent beta and gamma dose rates, and the cosmic dose rate. Age estimates are determined by dividing the equivalent stored dose by the dose rate (Table 5-5). Uncertainty on the age estimates is given by combination of the uncertainty on the dose rates and stored doses; in table 5-5 both the weighted standard deviation and error are listed (in the format ± *weighted standard deviation* (*weighted error*)).

SUTL no.	Archaeological significance	Years / ka	Calendar years
2861	red sands, base, in position of profile 1 (= SUTL2863)	3.22 ± 0.29	1210 ± 330 (290) BC
2862	clean sands, top, in position of profile 1 (< SUTL2864)	0.12 ± 0.06	AD 1900 ± 60 (50)†
2863	red sands, base, in position of profile 2 (= SUTL2861)	1.99 ± 0.15	AD 30 ± 210 (150)
2864	red sands, middle, in position of profile 2 (>SUTL2863, <SUTL2865)	0.63 ± 0.06	AD 1380 ± 70 (60)
2865	red sands, top, in position of profile 2 (>SUTL2864, >SUTL2863)	1.10 ± 0.10 *0.64 ± 0.10*	AD 920 ± 130 (100) *AD 1370 ± 100 (80)*
2866	red sands, top; modification of E noost	0.48 ± 0.06	AD 1540 ± 320 (60)
2867	red sands, top; construction of W noost	0.81 ± 0.07	AD 1210 ± 190 (70)
2868	sands, above brown sandy soil (lowest sampled in profile) (SUTL2868<SUTL2869<SUTL2870)	0.70 ± 0.05	AD 1320 ± 50 (50)
2869	sands, top of charcoal-bearing horizon (SUTL2868<SUTL2869<SUTL2870)	0.52 ± 0.04	AD 1500 ± 40 (40)
2870	sands (SUTL2868<SUTL2869<SUTL2870)	0.31 ± 0.02	AD 1710 ± 20 (20)

Table 5-5: Quartz OSL sediment ages

errors stated: ± weighted standard deviation (weighted error)

6. Discussion and conclusions

We have coupledluminescence profiling and OSL dating to produce a complete sequence of dates for the substrate stratigraphies adjacent to, and underlying the Underhoull noosts, and for the beach section in the neighbouring bay to the West. In summary, the key findings are:

1.) Initial screening on all profiling samples using the portable OSL reader, provided the first indication that the substrate stratigraphies adjacent to the noost extend from the late glacial period to the modern day. The progression in signal intensities with depth (following both red and blue stimulation), from the turf base, through the upper accumulation of sands, the underlying clay/sand sequence, into the 'weathered tills', is broadly consistent with the expected age ranges of 10-50 years, 500 years (Little Ice Age), and 15 000 years (the waning stages of the last glacial cycle). Moreover, the maxima and dynamic ranges in OSL and IRSL signal intensities for the sequences beneath the noosts, suggest that the construction and modification of these structures were temporally distinct. For the beach section in the more westerly of the embayments, the range in OSL and IRSL signal intensities through these sediments, indicate that these sediments represent a shorter chronology.

2.) Further characterisation of these profiling samples, by paired analyses on quartz and polymineral extracts using a simplified 2-step SAR OSL protocol, confirmed the findings of the initial screening - reinforcing the argument for a modest chronology across the substrate stratigraphies adjacent to, and beneath the noosts; and a shorter chronology for the beach section. Furthermore, the maxima and range of stored dose estimate obtained for the strata beneath the noosts, suggest that their construction and modification were temporally distinct.

3.) The temporal framework to interpret the environmental/climatic archives in the Underhoull sediments, as well as the constructional sequence of the noosts, is provided by the 10 sediment samples, collected across the bay, in both the western embayment (7 samples, noost sections) and western embayment (3 samples, beach section). In the east, from the four profiles encompassing the sediment/substrate stratigraphies adjacent to, and beneath the noosts, the dating samples cover the sequence of: i) initial sand accumulation (2861/OSL1 and 2863/OSL3), ii.) later sand accumulation (a progression? or episodic?; 2862/OSL2, 2864/OSL4 and 2865/OSL5), iii.) modification(/construction?) of noost 1 (2866/OSL6) and iv.) construction of noost 2 (2867/OSL7). In the west, from the beach section, the dating samples should provide the temporal framework to interpret the later (potentially the last 500-600 years) of environmental/climatic history of the bay (2868-70/OSL8-10).

The combination of these approaches provided the following chronology, for the noost sections: 1.) onset of sand activity, as recorded in the sedimentary archives of profiles 1 and 2, at 3.22 ± 0.29 ka (1210 ± 290BC; SUTL2861) and 1.99 ± 0.15 ka (AD30 ± 150; SUTL2863); 2.) construction of the W noost after 0.81 ± 0.07 ka (AD1210 ± 70; SUTL2867); 3.) modification and

re-built of the E noost after 0.48 ± 0.06 ka (AD1540 ± 60; SUTL2866); and 4.) continued sand movements into the early 20th century AD (0.12 ± 0.06 ka; AD1900 ± 60; SUTL2862), with arguably heightened activity at the onset of the Little Ice Age (0.64 ± 0.10 ka; AD 1380 ± 60; SUTL2866). For clarification, the uncertainties listed here, and in the summary, follow the reasoning given in sections 5.3.2 and 5.3.3. The uppermost sample collected in profile 2, at the top of the red sands, yielded a sediment age of 1.10 ± 0.10 ka (AD 920 ± 130; SUTL2865). This warrants further explanation: 1. it may imply some post-depositional disturbance (with mixing of residual or older materials), 2. or that this unit was poorly reset at deposition (the older residual materials contributing to an over age-estimation), or 3. that the sampling position cuts back into progressively older deposits. Interestingly though, if greatest weight is given to the lowest dose population (at c. 0.8 Gy; Table 5-1), then this would correspond to a depositional age of 0.64 ± 0.10 ka (AD 1370 ± 100), contemporaneous with the deposition of the lower unit.

For the section along strike, the sediment chronology spans from the early 14th century AD through to the early 18th century AD (0.70 ± 0.05 ka; SUTL2868 to 0.31 ± 0.02 ka; SUTL2870), consistent with the onset and waning stages of the Little Ice Age. The age progression through this succession is augmented by the quartz SAR OSL age of 0.52 ± 0.04 ka (SUTL2869, at a depth of c. 130 cm), collected approximately equi-distance between the enclosing samples (at 190 cm and 65 cm); interestingly, these ages imply that the bounding sand packages, between 65-130cm and 130-190cm, accumulated at similar rates (0.31 and 0.32 cm a^{-1}, indistinguishable within error).

The emerging sediment-based quartz OSL SAR chronologies for sand blows in southern Unst, both at Underhoull and Sandwick, and elsewhere on the Shetland Isles, attest to a prolonged history of sand movements from the Neolithic, through the Norse period into the Little Ice Age and today. We now have 8 OSL dates associated with sand accumulations at Underhoull (and 4 from Sandwick), which provide clear evidence of a long history of sand movement. Further work would be needed to elucidate on the full range of periods represented in the sand filled landscapes, and to define their relationships to the Norse archaeology. This temporal framework also provides the first chronological evidence to support a Norse age for the noosts on the foreshore at Underhoull, and furthermore, continued use with some internal modifications into the 15-16th centuries AD.

7. References

Aitken, M.J., 1983, Dose rate data in SI units: PACT, v. 9, p. 69–76.

Anderson, D.E., 1998, A reconstruction of Holocene climatic changes from peat bogs in north-west Scotland: Boreas, v. 27, p. 208-224.

Bøtter-Jensen, L., Bulur, E., Duller, G.A.T., and Murray, A.S., 2000, Advances in luminescence instrument systems: Radiation Measurements, v. 32, p. 523-528.

Burbidge, C., McIlveny, J., and Sanderson, D.C.W., 2007a, Luminescence dating of back-dune sedimentary sequences from Dunnet Bay, Caithness, SUERC, p. 1-72.

Burbidge, C.I., Batt, C.M., Barnett, S.M., and Dockrill, S.J., 2001, The Potential for Dating the Old Scatness Site, Shetland, By Optically Stimulated Luminescence: Archaeometry, v. 43, p. 589-596.

Burbidge, C.I., Sanderson, D.C.W., Housley, R.A., and Allsworth Jones, P., 2007b, Survey of Palaeolithic sites by luminescence profiling, a case study from Eastern Europe: Quaternary Geochronology, v. 2, p. 296-302.

Clemmensen, L.B., Andreasen, F., Heinemeier, J., and Murray, A., 2001, A Holocene coastal aeolian system, Vejers, Denmark: landscape evolution and sequence stratigraphy: Terra Nova, v. 13, p. 129-134.

Clemmensen, L.B., Murray, A., Heinemeier, J., and de Jong, R., 2009, The evolution of Holocene coastal dunefields, Jutland, Denmark: A record of climate change over the past 5000 years: Geomorphology, v. 105, p. 303-313.

Dietze, M., Kreutzer, S., Fuchs, M.C., Burow, C., Fischer, M., and Schmidt, C., 2013, A practical guide to the R package Luminescence: Ancient TL, v. 32, p. 11-18.

Gilbertson, D.D., Schwenninger, J.L., Kemp, R.A., and Rhodes, E.J., 1999, Sand-drift and Soil Formation Along an Exposed North Atlantic Coastline: 14,000 Years of Diverse Geomorphological, Climatic and Human Impacts: Journal of Archaeological Science, v. 26, p. 439-469.

Kinnaird, T.C., Sanderson, D.C.W., and Bigelow, G., 2014, Luminescence dating of windblown sands from archaeological sites in Shetland (Early Modern Farmstead, Broo Peninsula; Norse settlement, Sandwick South, Unst), *in* Sanderson, D.C.W., ed., Luminescence Dating Reports, SUERC, p. 1-49.

Kinnaird, T.C., Sanderson, D.C.W., and Bigelow, G.F., 2015, Feldspar SARA IRSL dating of very low dose rate aeolian sediments from Sandwick South, Unst, Shetland: Quaternary Geochronology, v. 30, p. 168-174.

Kinnaird, T.C., Sanderson, D.C.W., and Simpson, I.A., 2013, Luminescence investigations at Quendale (Broo Peninsula, Shetland), *in* Sanderson, D.C.W., ed., Luminescence Dating Reports, SUERC, p. 1-15.

Kinnaird, T.C., Sanderson, D.C.W., and Woodward, N.L., 2011, Applying luminescence methods to geoarchaeology: a case study from Stronsay, Orkney: Earth and Environmental Science Transactions of the Royal Society of Edinburgh, v. 102, p. 191-200.

Langdon, P.G., Barber, K.E., and Hughes, P.D.M., 2003, A 7500-year peat-based palaeoclimatic reconstruction and evidence for an 1100-year cyclicity in bog surface wetness from Temple Hill Moss, Pentland Hills, southeast Scotland: Quaternary Science Reviews, v. 22, p. 259-274.

Mejdahl, V., 1979, Thermoluminescence daing: Beta-dose attenuation in quartz grains Archaeometry, v. 21, p. 61-72.

Murray, A.S., and Wintle, A.G., 2000, Luminescence dating of quartz using an improved single-aliquot regenerative-dose protocol: Radiation Measurements, v. 32, p. 57-73.

NEA, 2000, The JEF-2.2 Nuclear Data Library: Nuclear Energy Agency, Organisation for economic Co-operation and Development. JEFF Report, v. 17.

Prescott, J.R., and Hutton, J.T., 1994, Cosmic ray contributions to dose rates for luminescence and ESR dating: Large depths and long-term time variations: Radiation Measurements, v. 23, p. 497-500.

Rhodes, E.J., Bronk Ramsey, C., Outram, Z., Batt, C., Willis, L., Dockrill, S., and Bond, J., 2003, Bayesian methods applied to the interpretation of multiple OSL dates: high precision sediment ages from Old Scatness Broch excavations, Shetland Isles: Quaternary Science Reviews, v. 22, p. 1231-1244.

Sanderson, D.C.W., 1987, Thermoluminescence dating of vitrified Scottish Forts: Paisley, Paisley college.

—, 1988, Thick source beta counting (TSBC): A rapid method for measuring beta dose-rates: International Journal of Radiation Applications and Instrumentation. Part D. Nuclear Tracks and Radiation Measurements, v. 14, p. 203-207.

Sanderson, D.C.W., Bishop, P., Houston, I., and Boonsener, M., 2001, Luminescence characterisation of quartz-rich cover sands from NE Thailand: Quaternary Science Reviews, v. 20, p. 893-900.

Sanderson, D.C.W., Bishop, P., Stark, M.T., and Spencer, J.Q., 2003, Luminescence dating of anthropogenically reset canal sediments from Angkor Borei, Mekong Delta, Cambodia: Quaternary Science Reviews, v. 22, p. 1111-1121.

Sanderson, D.C.W., and Murphy, S., 2010, Using simple portable OSL measurements and laboratory characterisation to help understand complex and heterogeneous sediment sequences for luminescence dating: Quaternary Geochronology, v. 5, p. 299-305.

Sommerville, A.A., 2003, Luminescence dating of wind blown sands from archaeological sites in Northern Scotland: Glasgow, Unpublished PhD thesis, University of Glasgow.

Sommerville, A.A., Hansom, J.D., Housley, R.A., and Sanderson, D.C.W., 2007, Optically stimulated luminescence (OSL) dating of coastal aeolian sand accumulation in Sanday, Orkney Islands, Scotland: The Holocene, v. 17, p. 627-637.

Wilson, P., 2002, Holocene coastal dune development on the South Erradale peninsula, Wester Ross, Scotland: Scottish Journal of Geology, v. 38, p. 5-13.

Wilson, P., and Braley, S.M., 1997, Development and age structure of Holocene coastal sand dunes at Horn Head, near Dunfanaghy, Co Donegal, Ireland: The Holocene, v. 7, p. 187-197.

Wilson, P., Clark, R., Birnie, J., and Moore, D.M., 2002, Late Pleistocene and Holocene landscape evolution and environmental change in the Lake Sulivan area, Falkland Islands, South Atlantic: Quaternary Science Reviews, v. 21, p. 1821-1840.

Wilson, P., McGourty, J., and Bateman, M.D., 2004, Mid-to late-Holocene coastal dune event stratigraphy for the north coast of Northern Ireland: The Holocene, v. 14, p. 406-416.

Wilson, P., Orford, J.D., Knight, J., Braley, S.M., and Wintle, A.G., 2001, Late-Holocene (post-4000 years BP) coastal dune development in Northumberland, northeast England: The Holocene, v. 11, p. 215-229.

Wintle, A.G., Clarke, M.L., Musson, F.M., Orford, J.D., and Devoy, R.J.N., 1998, Luminescence dating of recent dunes on Inch Spit, Dingle Bay, southwest Ireland: The Holocene, v. 8, p. 331-339.

Appendix A1: Dose Response Plots

Quartz Composite OSL Dose Response Curves

Figure A-1: Composite dose response curves for SUTL2861

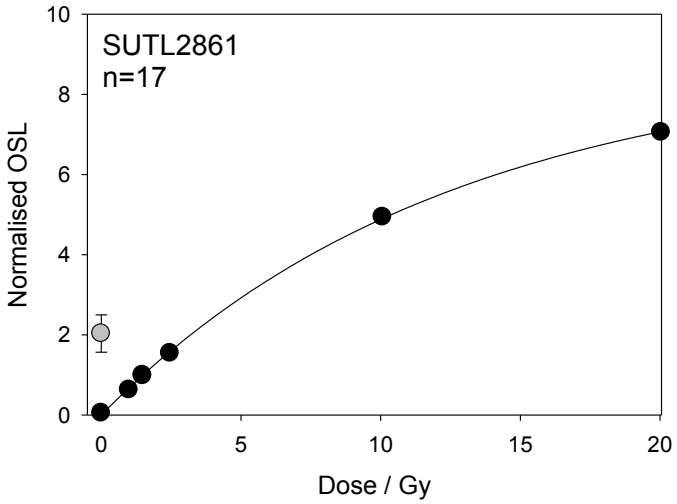

Figure A-2: Composite dose response curves for SUTL2863

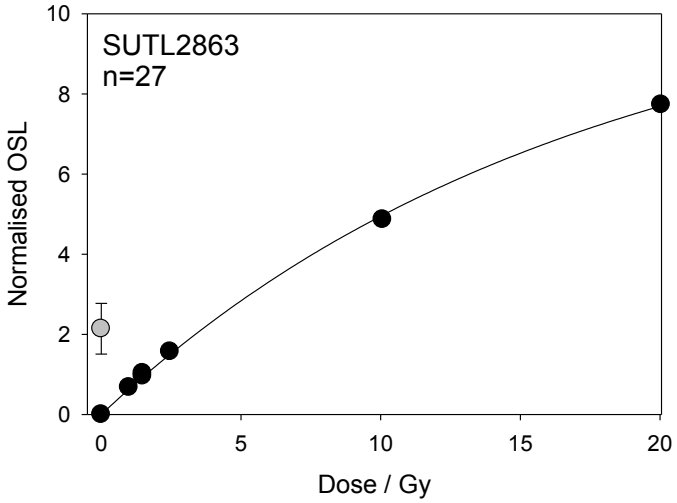

Figure A-3: Composite dose response curves for SUTL2864

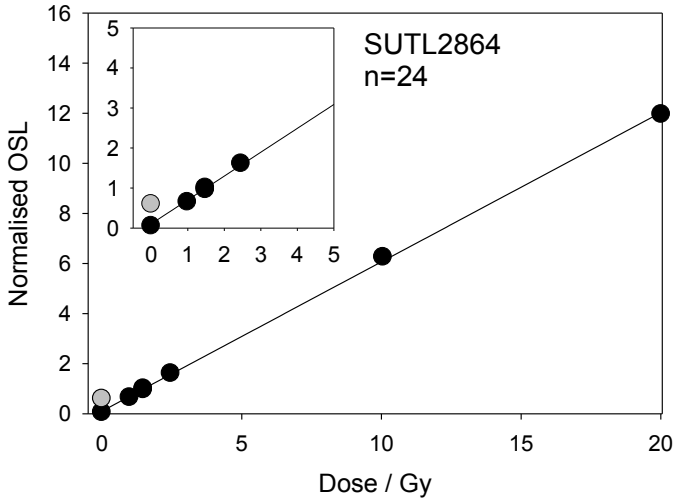

Figure A-4: Composite dose response curves for SUTL2865

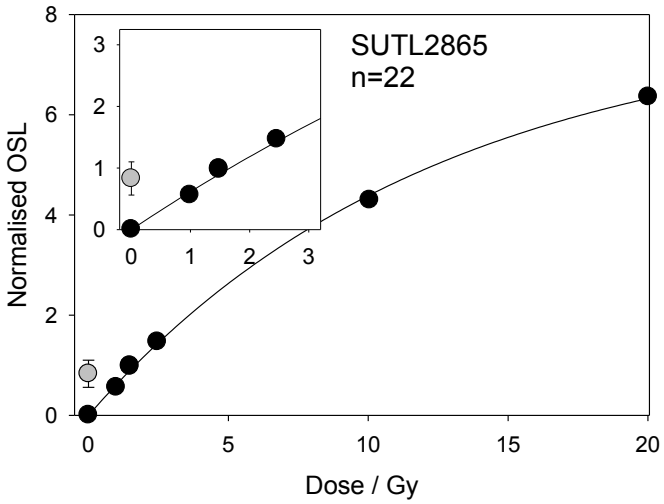

Figure A-5: Composite dose response curves for SUTL2866

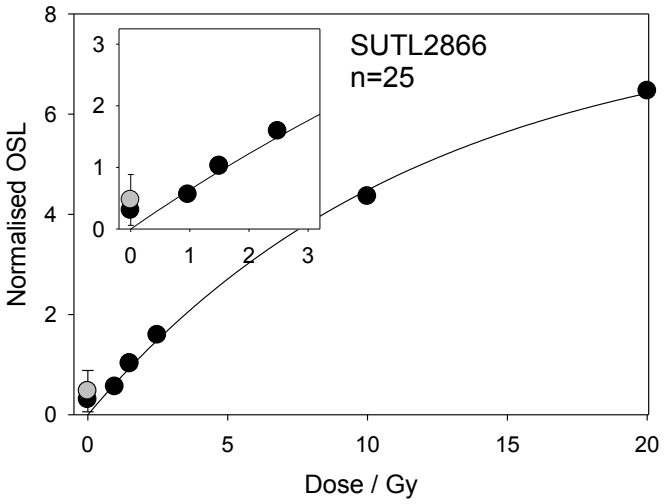
SUTL2866
n=25
Normalised OSL
Dose / Gy
0
2
4
6
8
0
5
10
15
20
0
1
2
3

Figure A-6: Composite dose response curves for SUTL2867

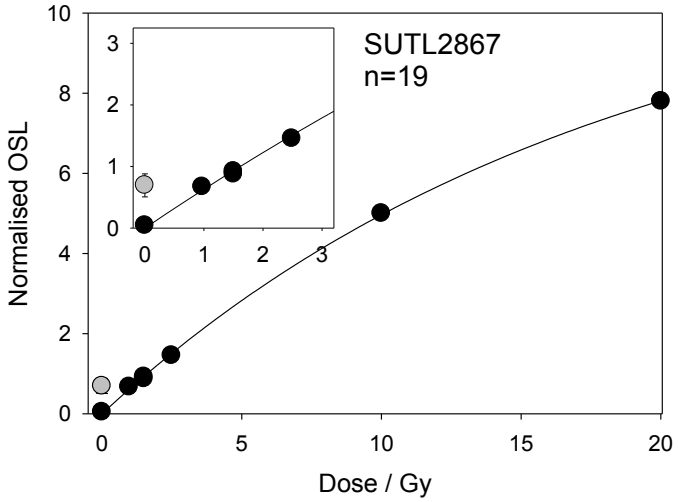

Figure A-7: Composite dose response curves for SUTL2868

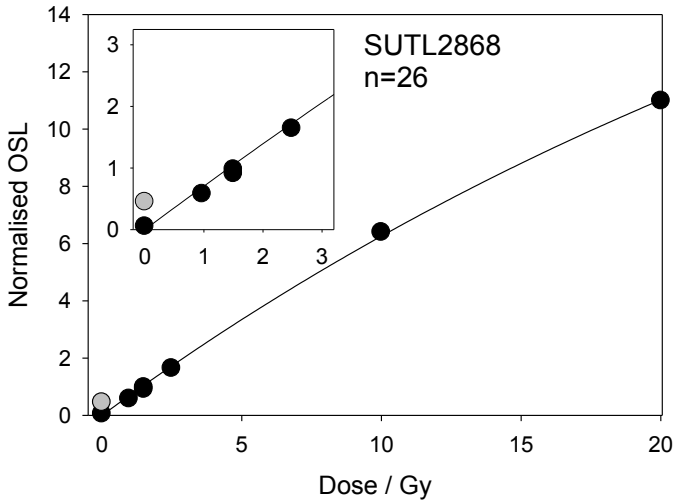

Figure A-8: Composite dose response curves for SUTL2869

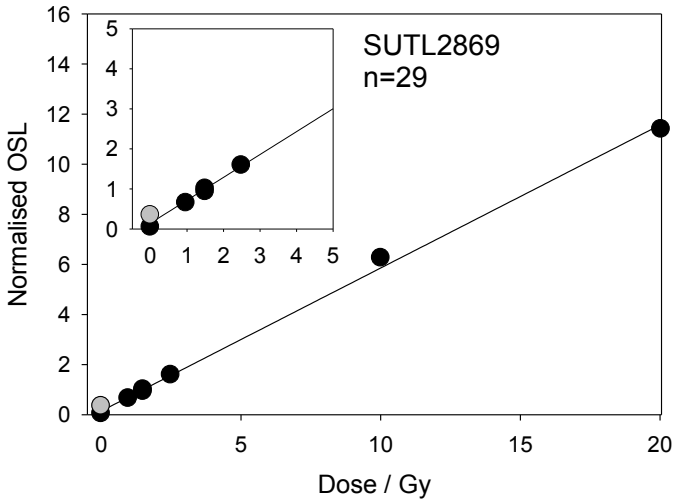
SUTL2869
n=29
Normalised OSL
Dose / Gy
0
2
4
6
8
10
12
14
16
0
5
10
15
20
0
1
2
3
4
5

Figure A-9: Composite dose response curves for SUTL2870

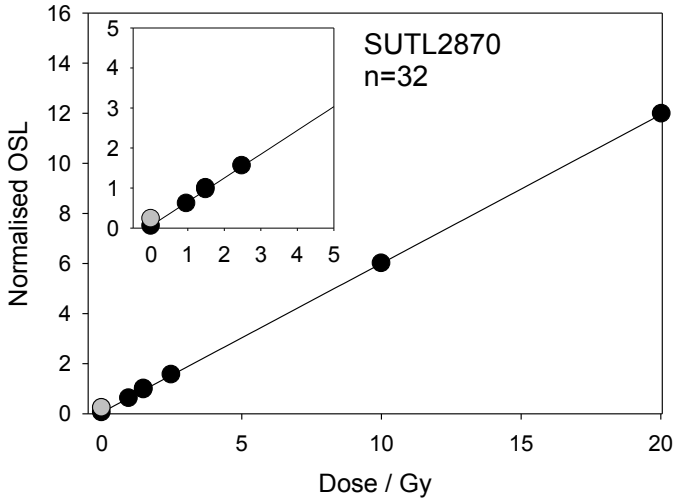

Appendix B1: De distributions

Figure B-1: Equivalent dose distributions for SUTL2861 (after Dietze et al., 2013), as (a) Abanico Plot, and (b) KDPE plot

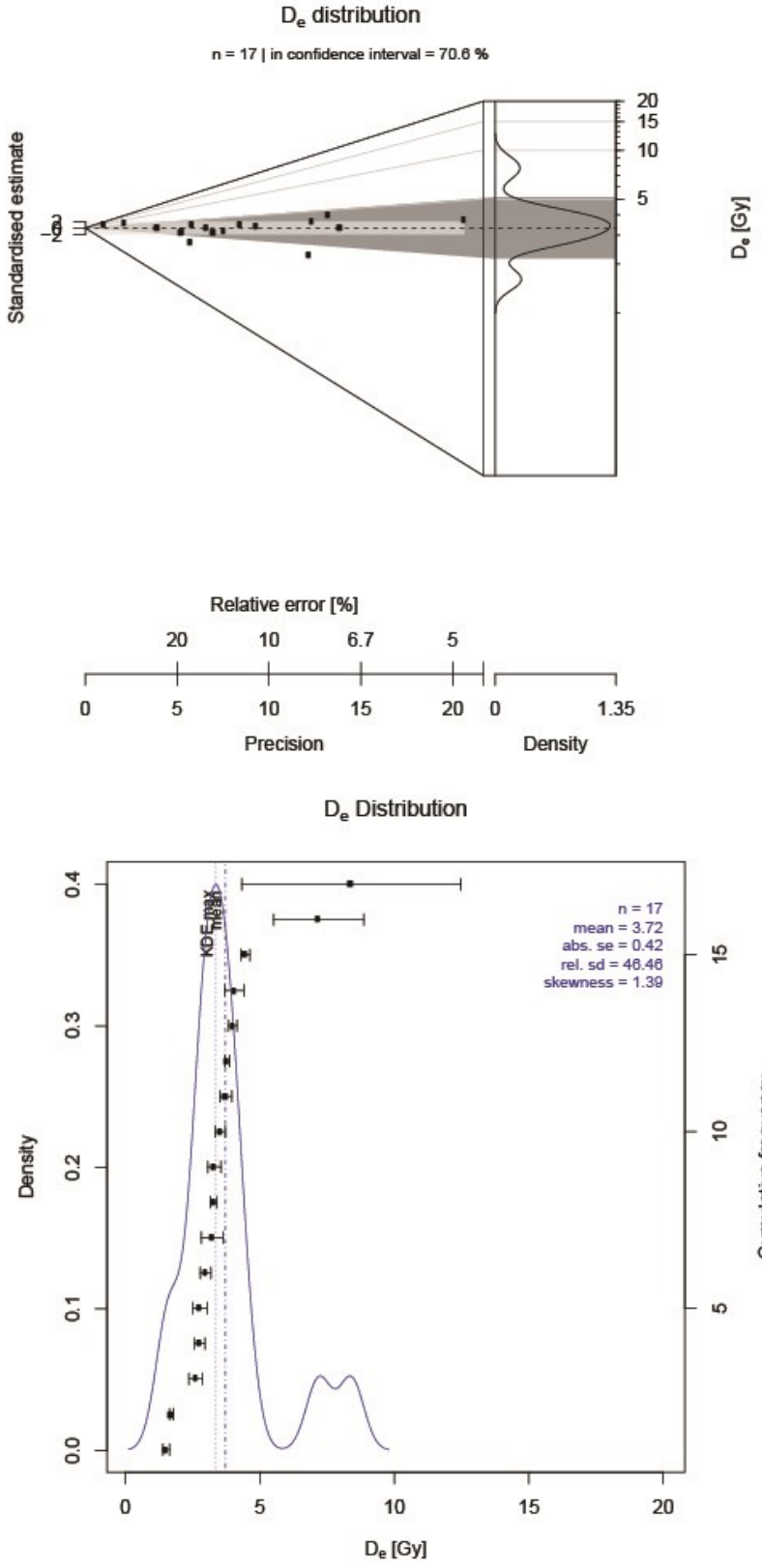
De distribution
n = 17 | in confidence interval = 70.6 %
Standardised estimate
De [Gy]
Relative error [%]
20
10
6.7
5
0
5
10
15
20
Precision
0
1.35
Density
De Distribution
n = 17
mean = 3.72
abs. se = 0.42
rel. sd = 46.46
skewness = 1.39
KDE max
mean
Density
Cumulative frequency
De [Gy]

Figure B-2: Equivalent dose distributions for SUTL2863 (after Dietze et al., 2013), as (a) Abanico Plot, and (b) KDPE plot

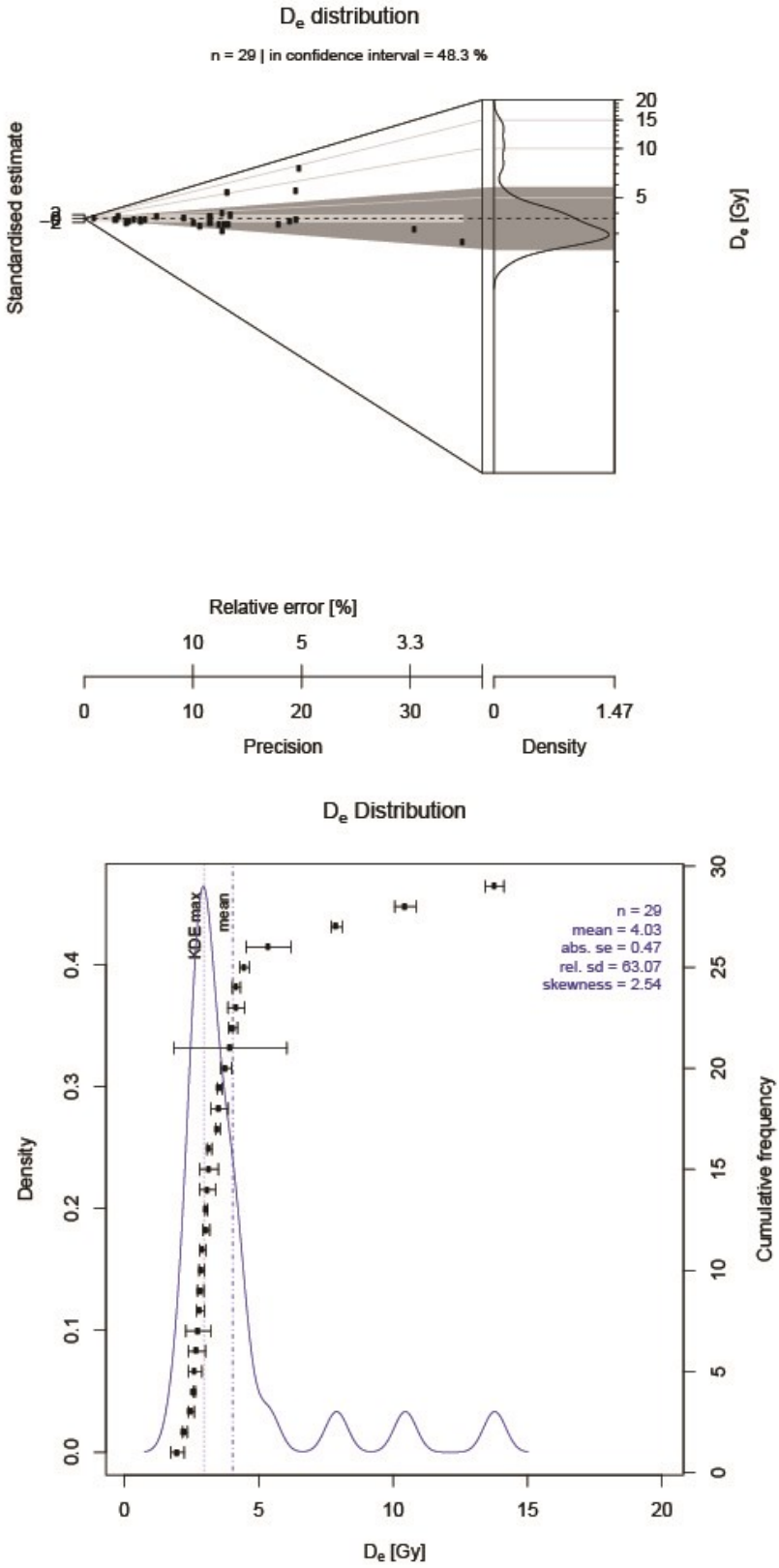

Figure B-3: Equivalent dose distributions for SUTL2864 (after Dietze et al., 2013), as (a) Abanico Plot, and (b) KDPE plot

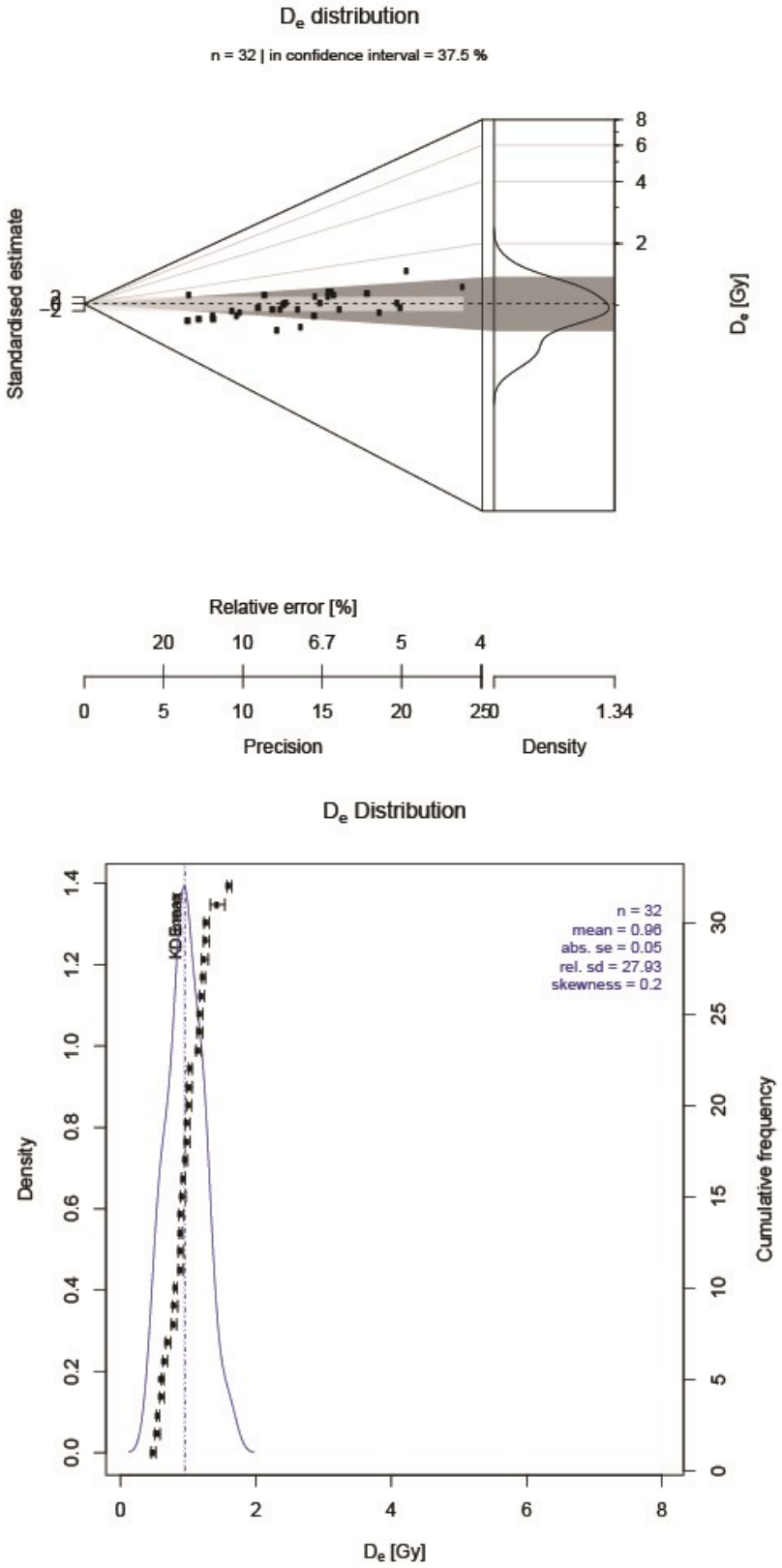

Figure B-4: Equivalent dose distributions for SUTL2865 (after Dietze et al., 2013), as (a) Abanico Plot, and (b) KDPE plot

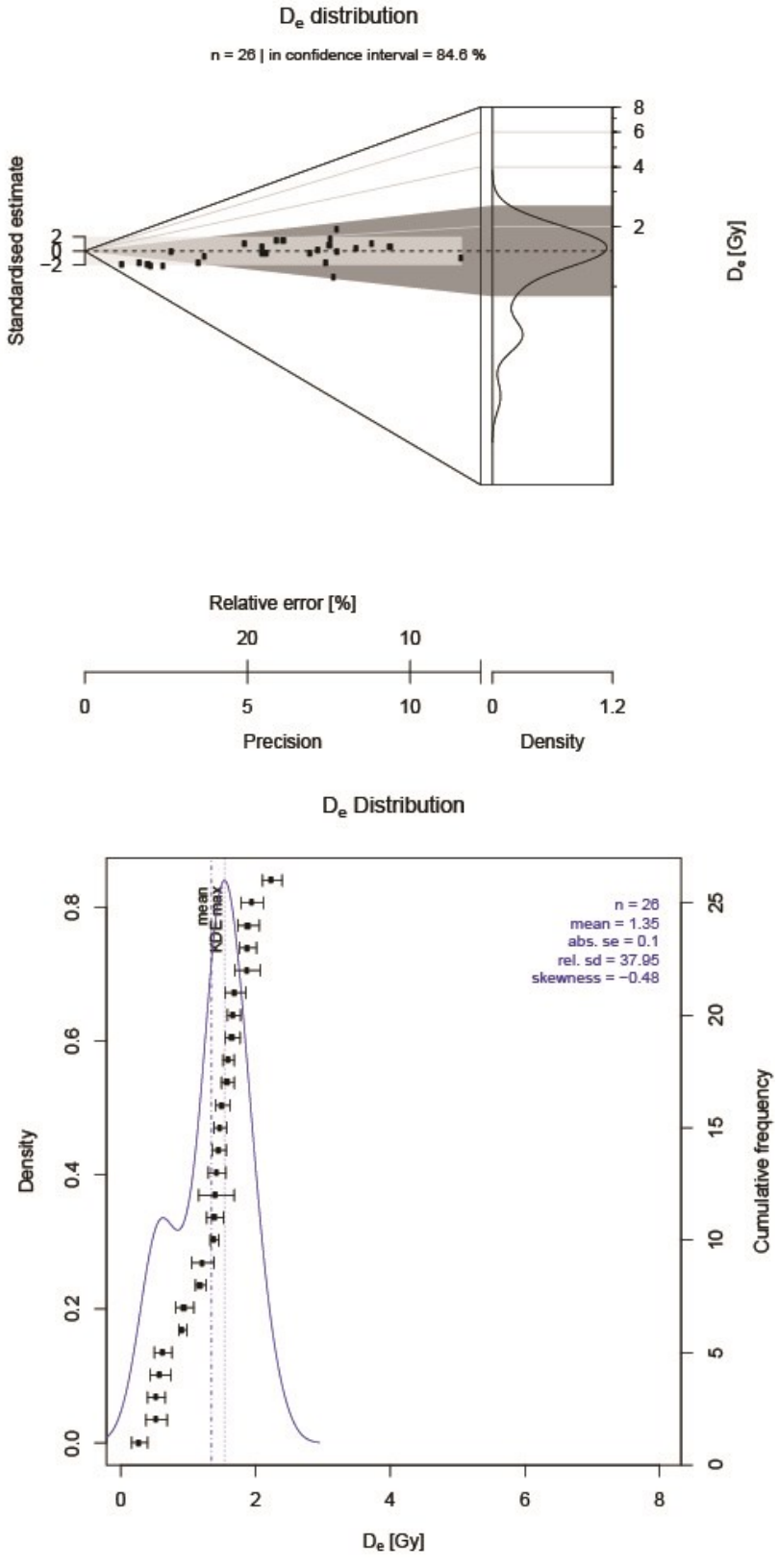

Figure B-5: Equivalent dose distributions for SUTL2866 (after Dietze et al., 2013), as (a) Abanico Plot, and (b) KDPE plot

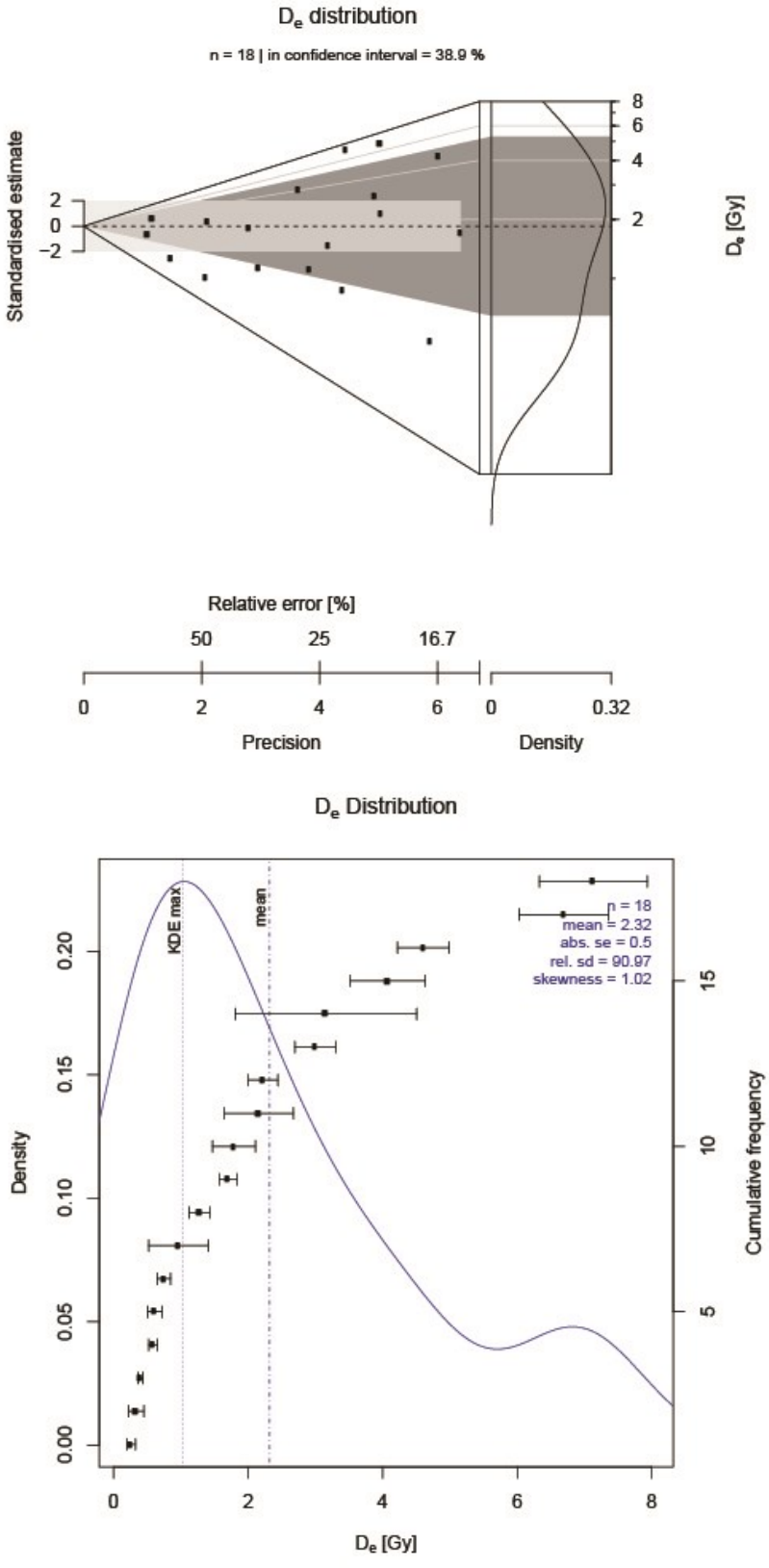

Figure B-6: Equivalent dose distributions for SUTL2867 (after Dietze et al., 2013), as (a) Abanico Plot, and (b) KDPE plot

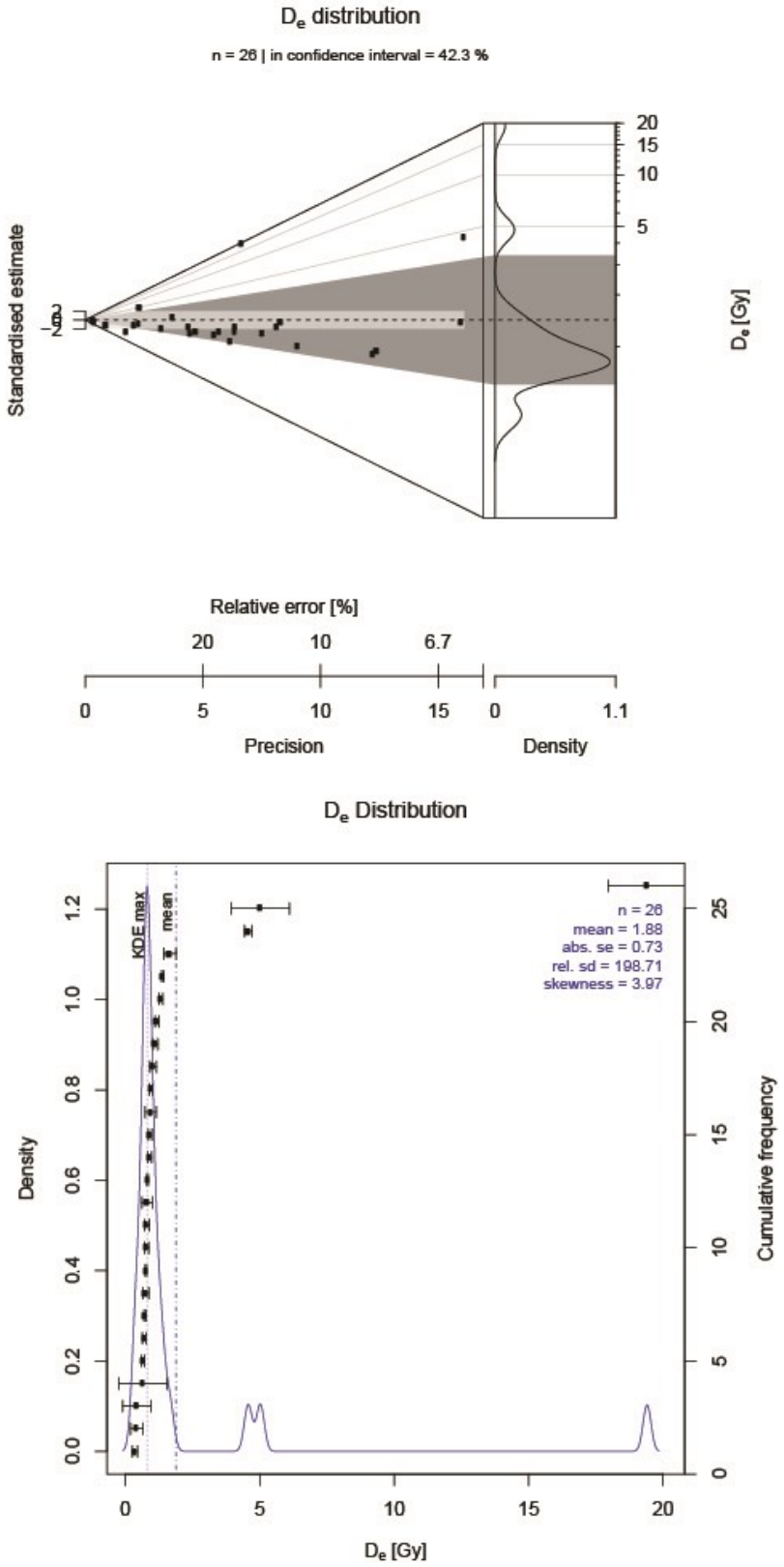

Figure B-7: Equivalent dose distributions for SUTL2868 (after Dietze et al., 2013), as (a) Abanico Plot, and (b) KDPE plot

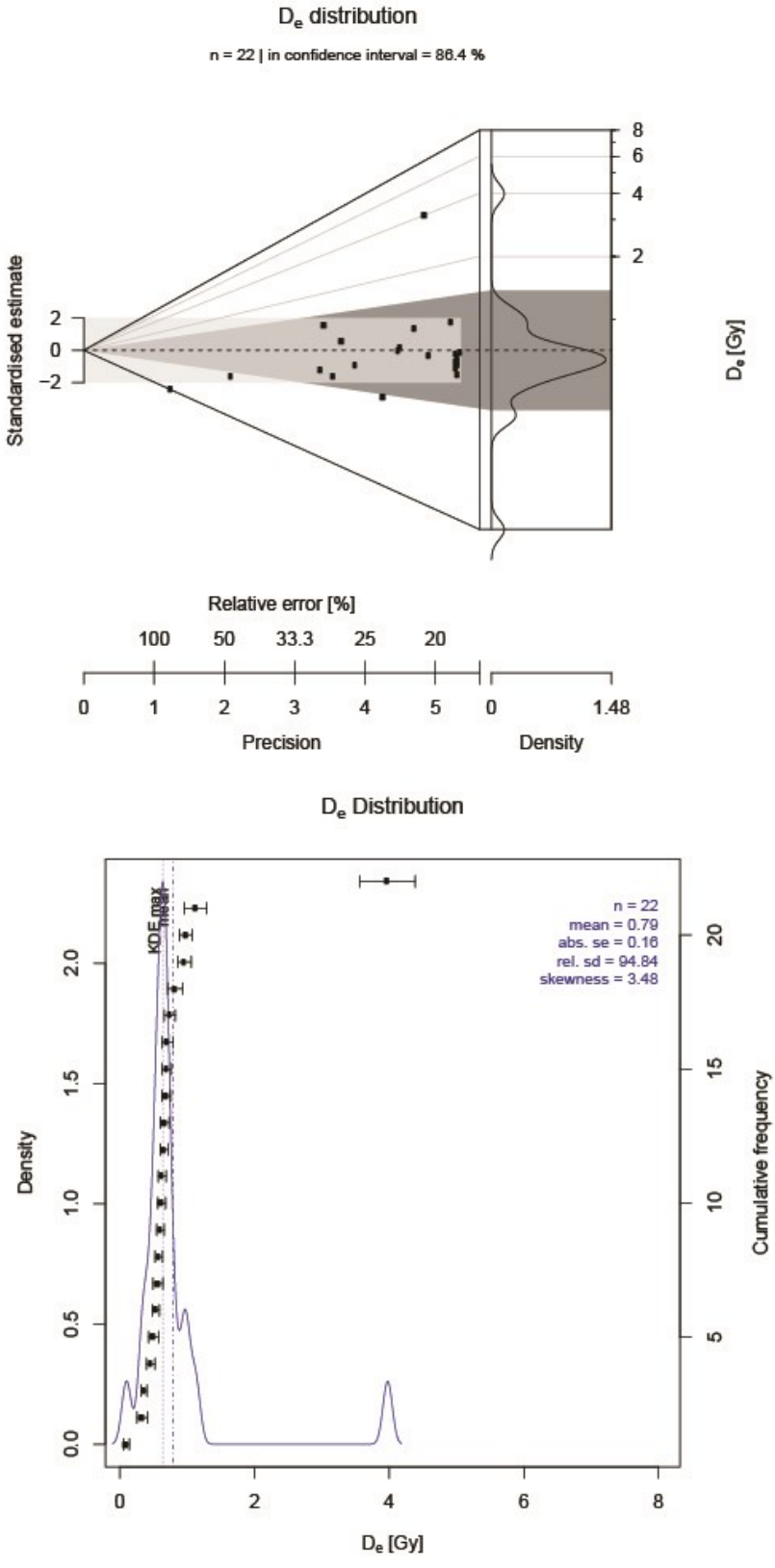

Figure B-8: Equivalent dose distributions for SUTL2869 (after Dietze et al., 2013), as (a) Abanico Plot, and (b) KDPE plot

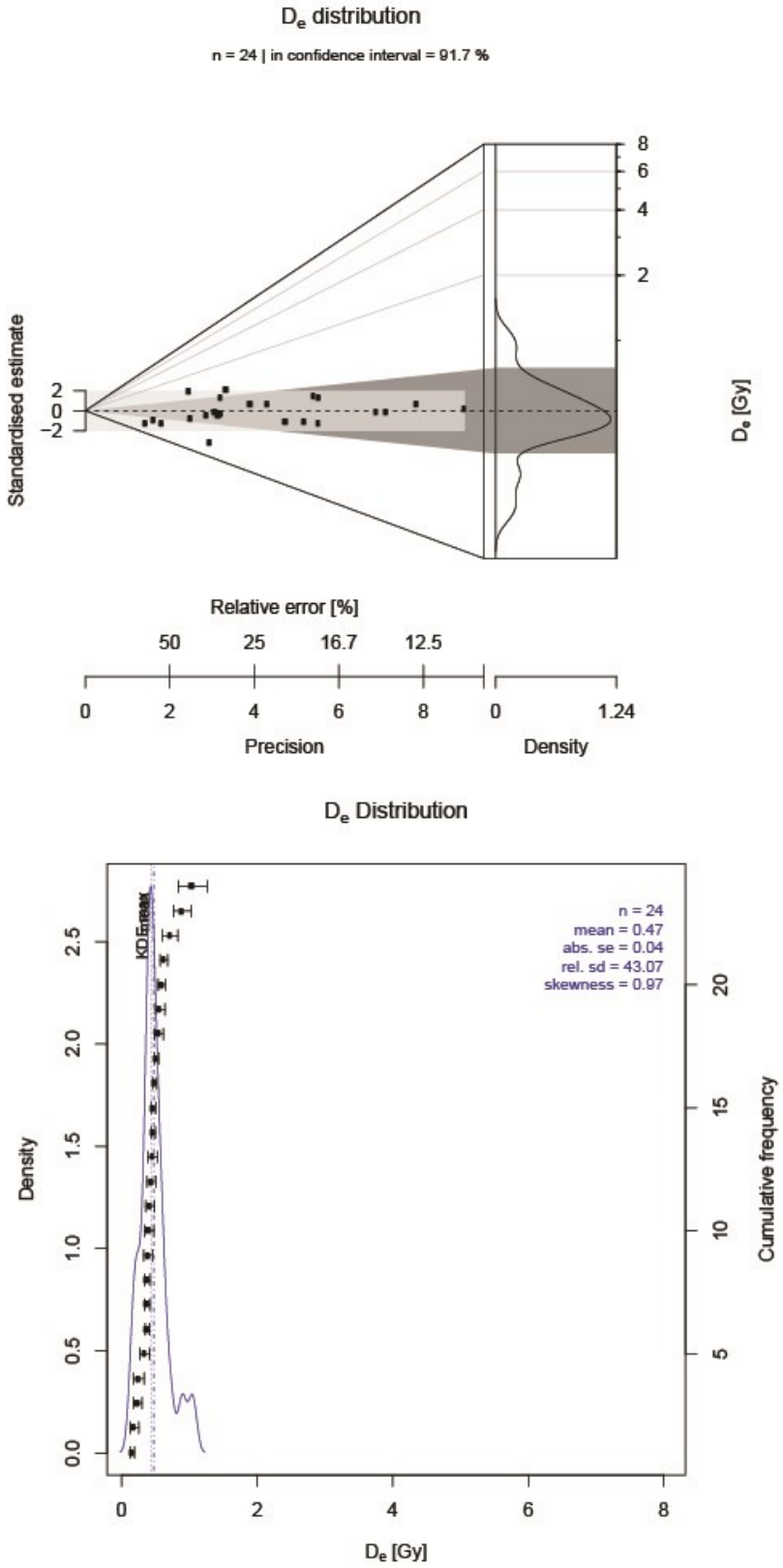

Figure B-9: Equivalent dose distributions for SUTL2870 (after Dietze et al., 2013), as (a) Abanico Plot, and (b) KDPE plot

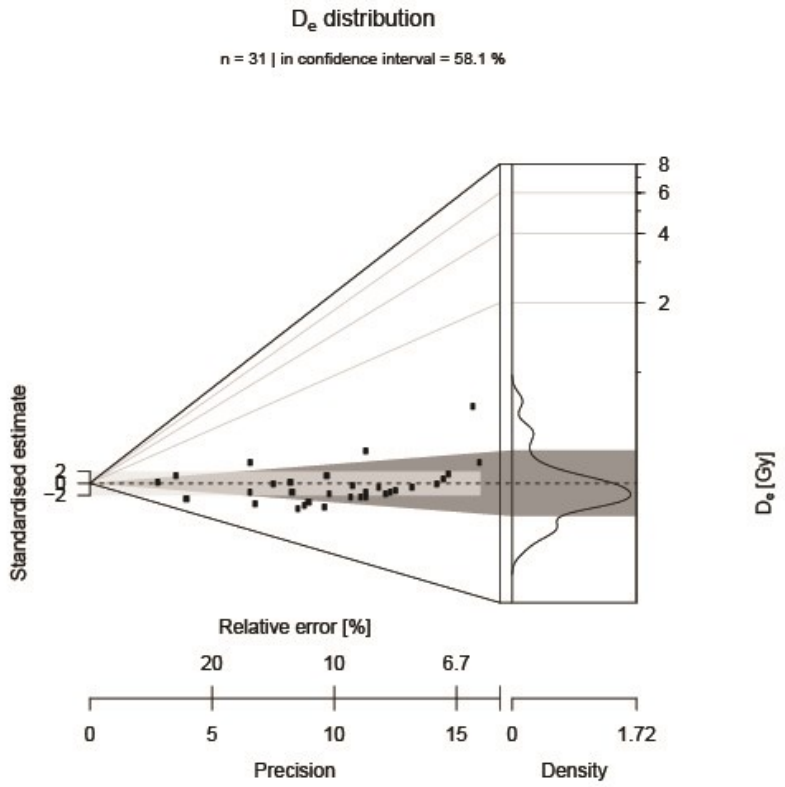
De distribution
n = 31 | in confidence interval = 58.1 %
Standardised estimate
De [Gy]
Relative error [%]
20
10
6.7
Precision
Density
1.72

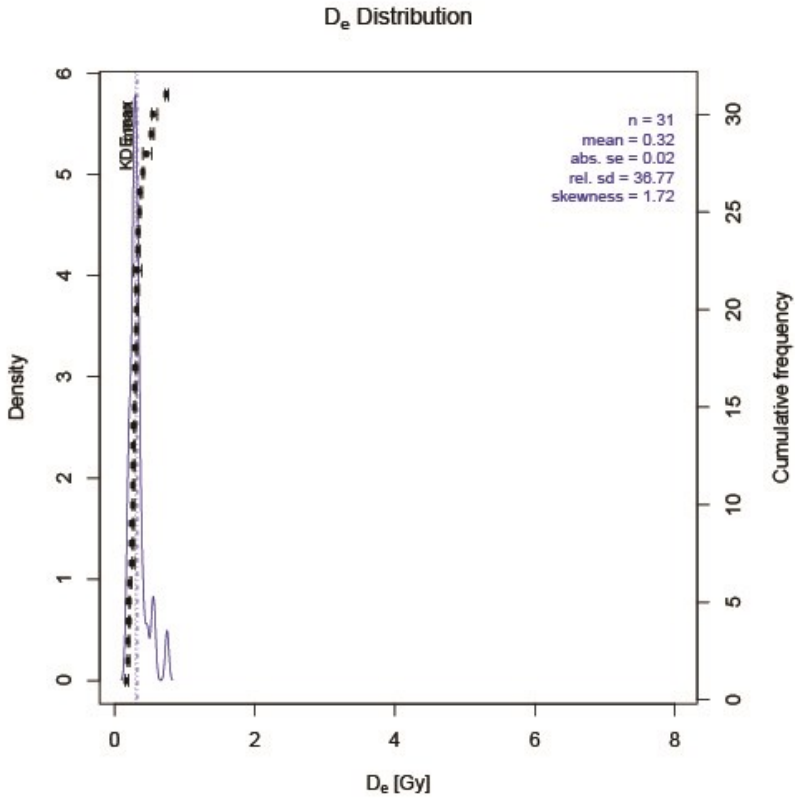
De Distribution
KDEmax
n = 31
mean = 0.32
abs. se = 0.02
rel. sd = 36.77
skewness = 1.72
Density
Cumulative frequency
De [Gy]

Appendix B – Geomorphological maps

The following geomorphological maps were created while at the field sites, as reported in Chapter 3 of the thesis.

B1 – Lunda Wick, Unst, Shetland

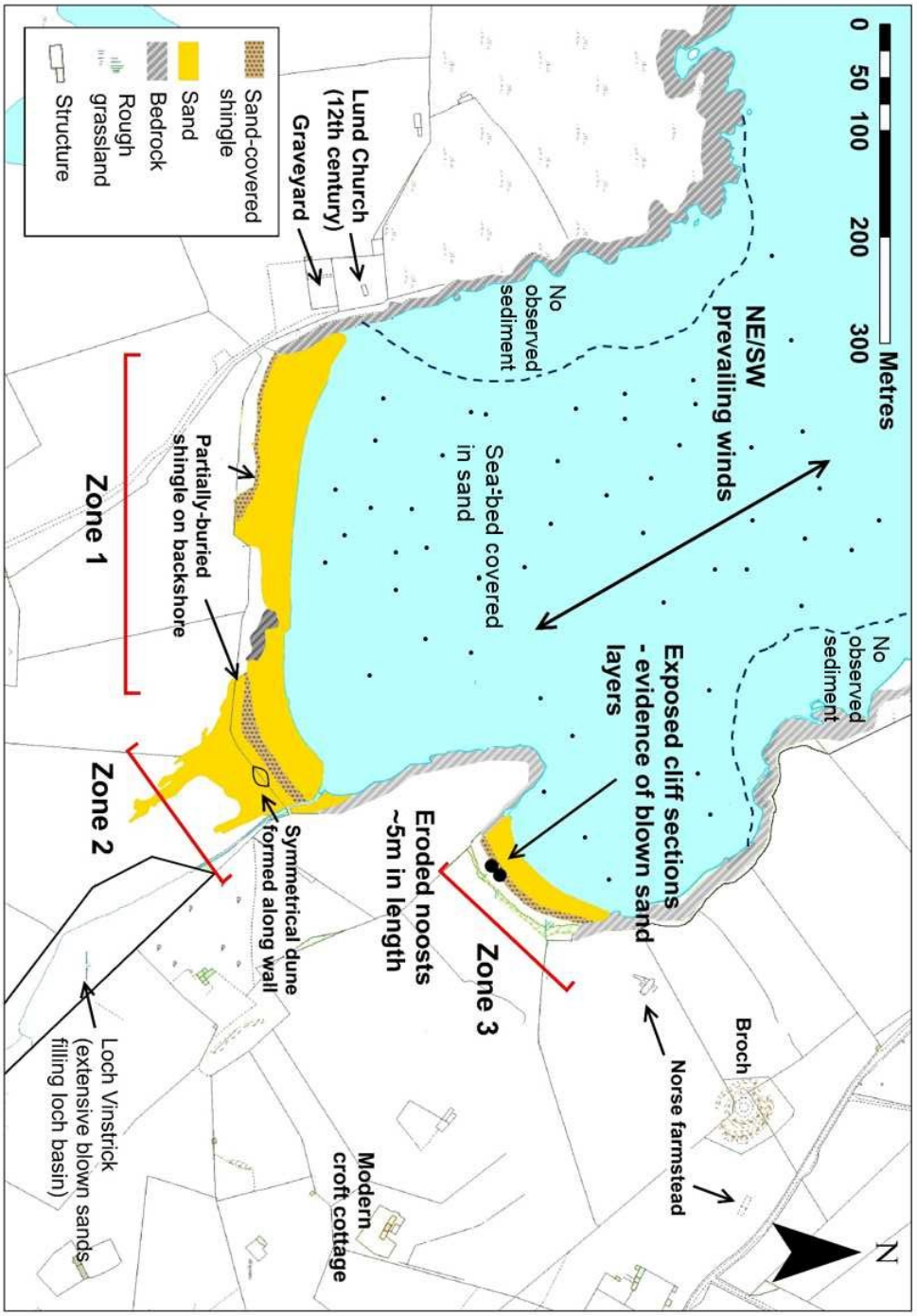

B2 – Sandwick, Unst, Shetland

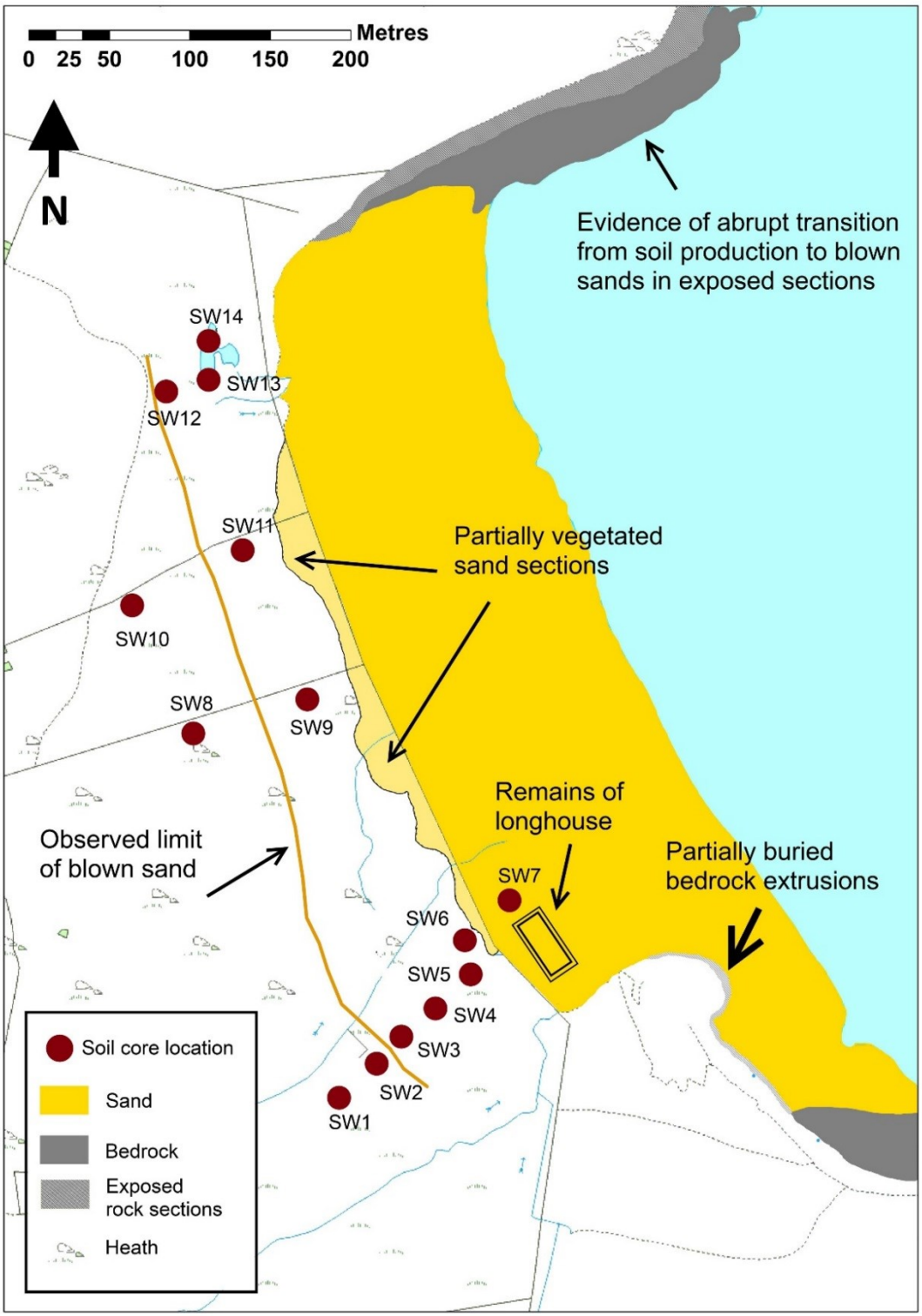

B3 – Hvalsey, Greenland

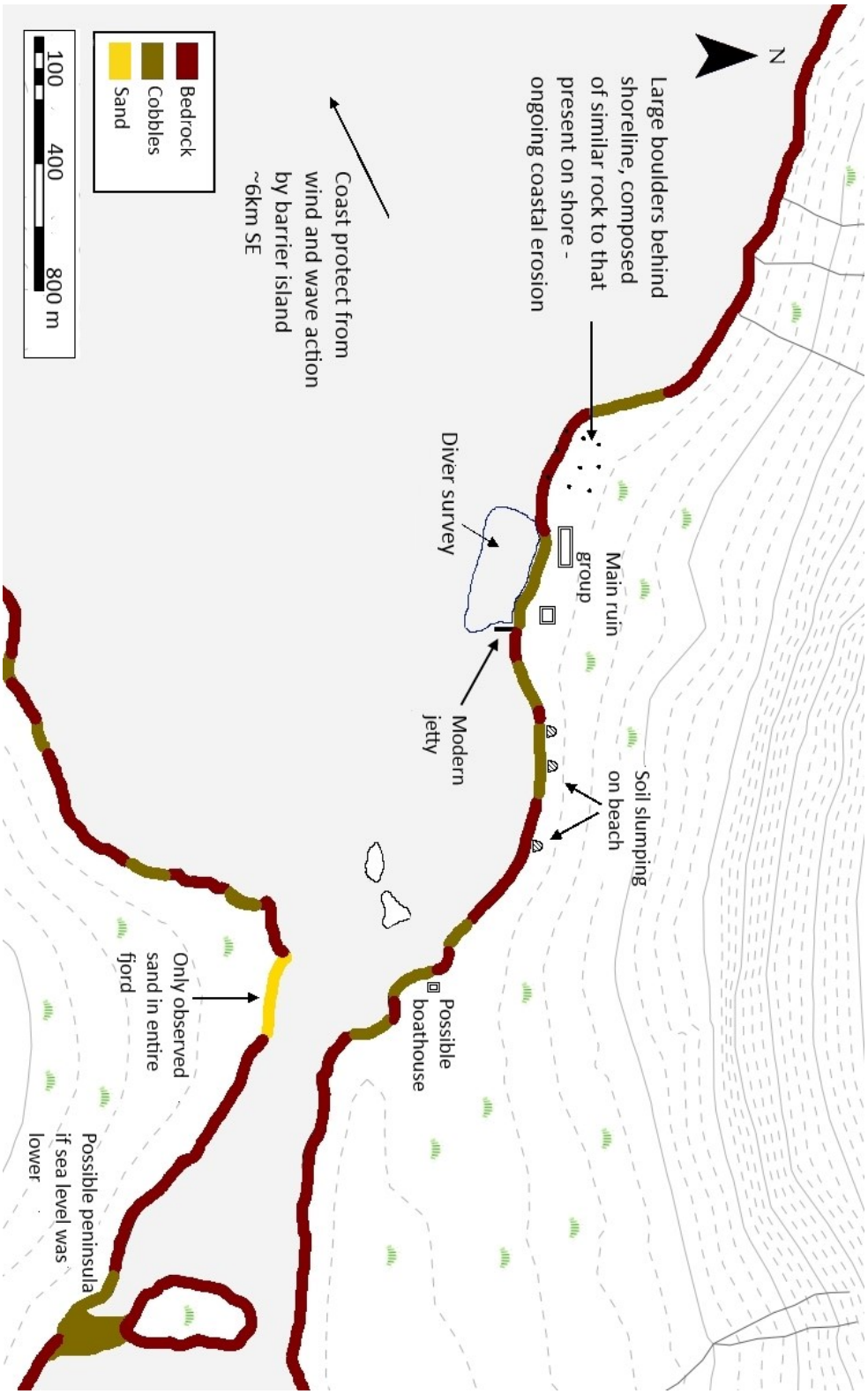

Dive-survey interpolated grid - Hvalsey

Interpolated grid from dive survey carried out at Hvalsey, July 2014. Dive transects marked by black line, roughly following depth contour as reported by dive computer. Grid interpolated in ArcMap 10.1.

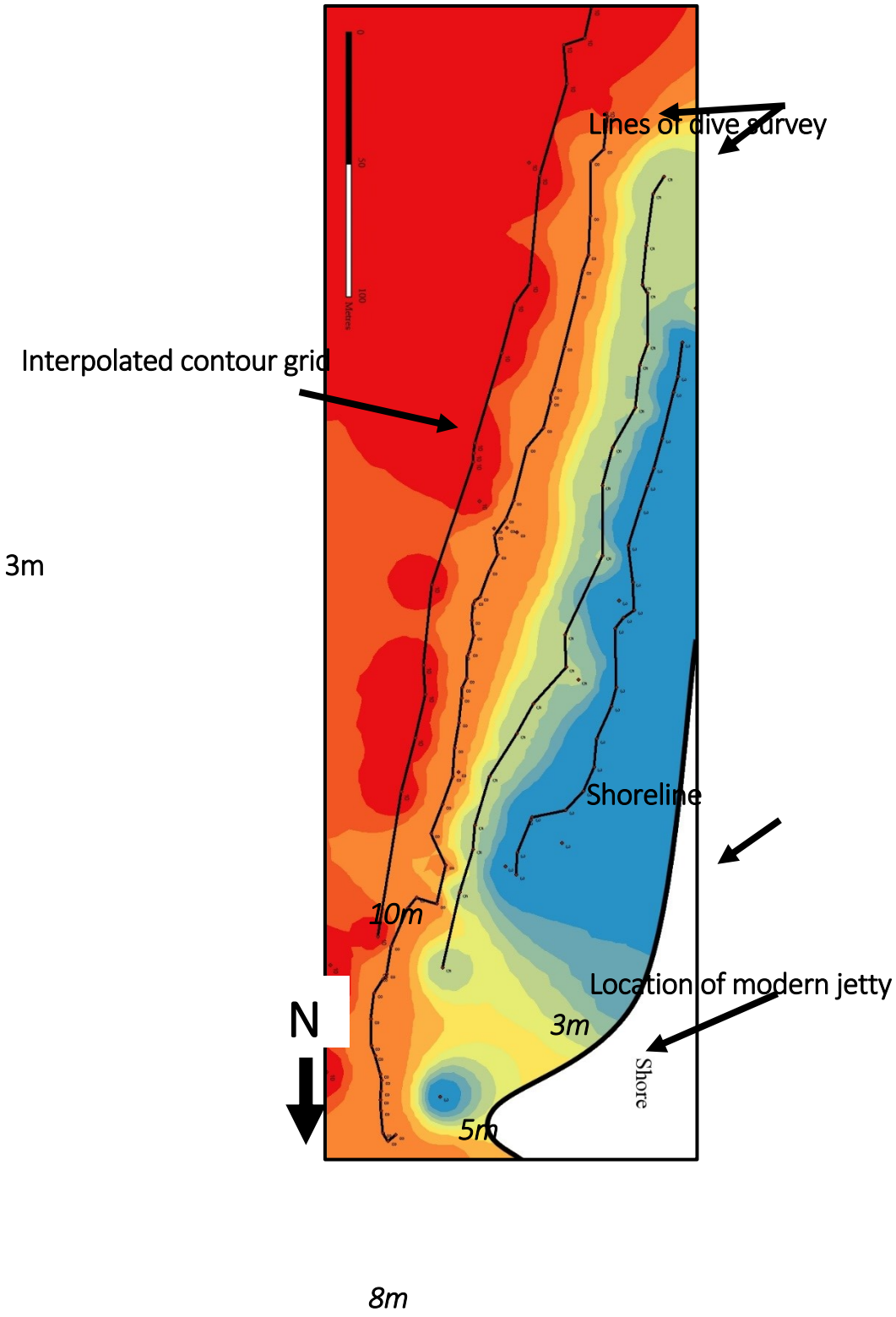

B4 – Igaliku Kujalleq, Greenland

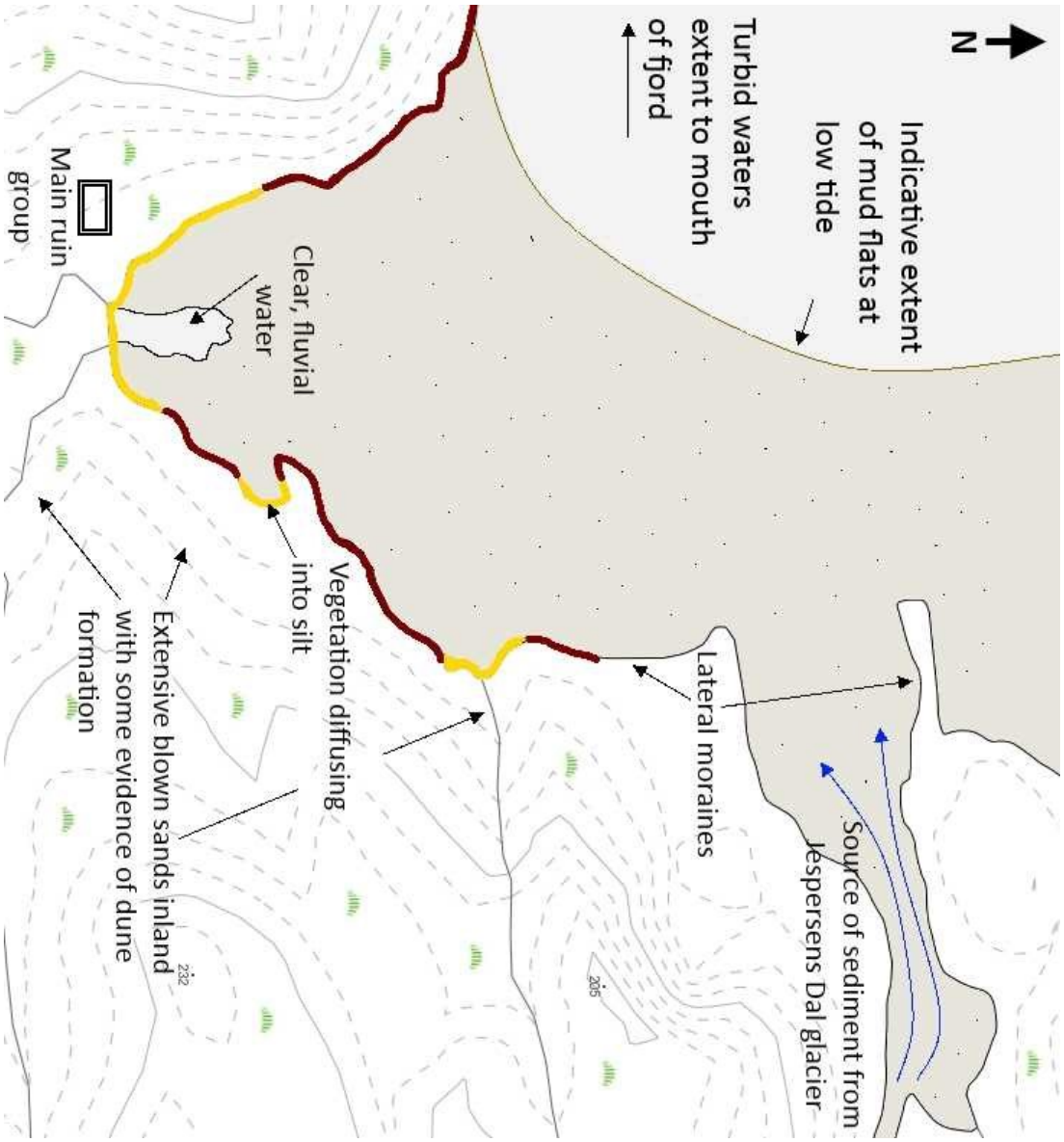

B5 – Qassiarsuk, Greenland

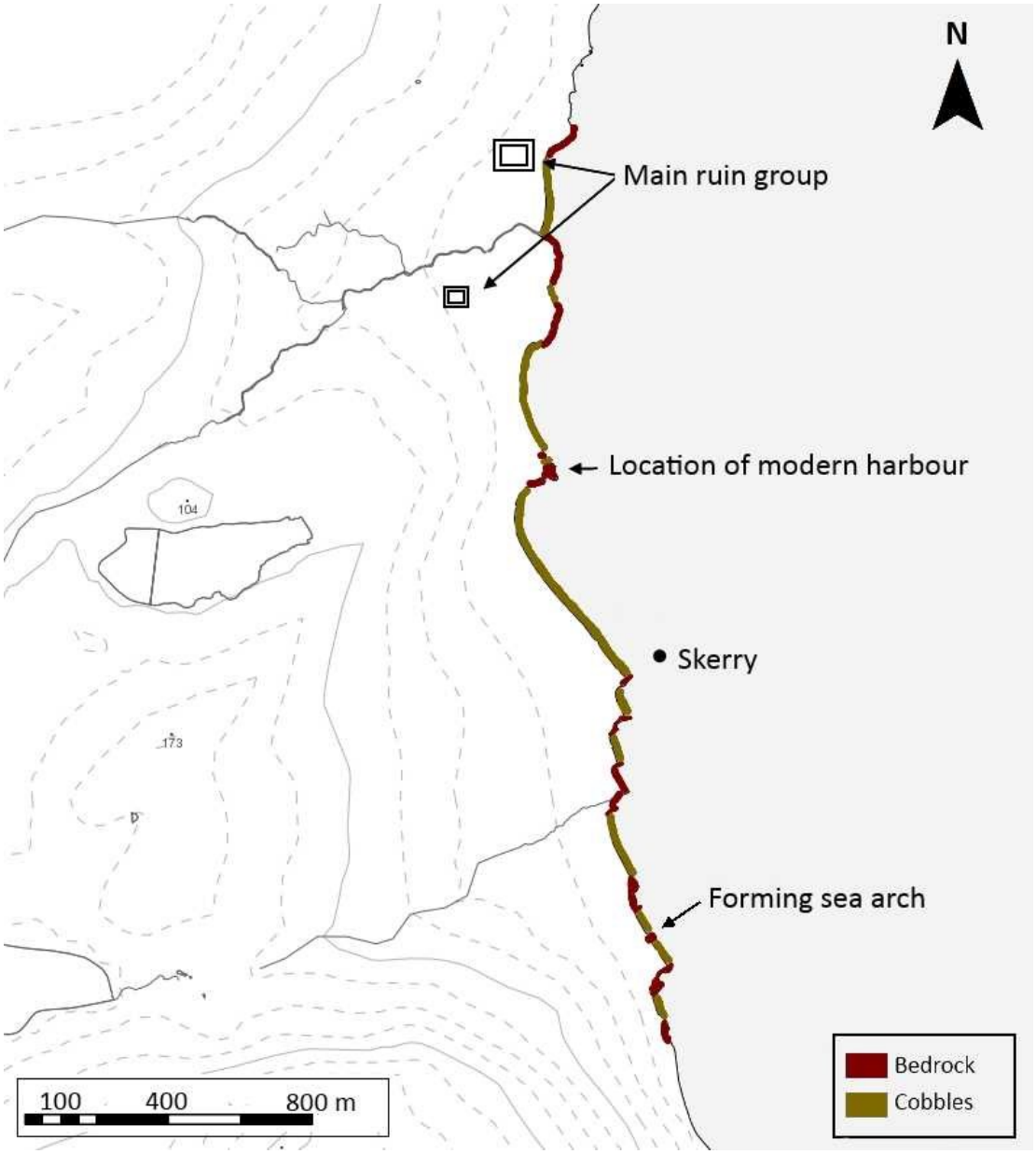

B6 – Igaliku, Greenland

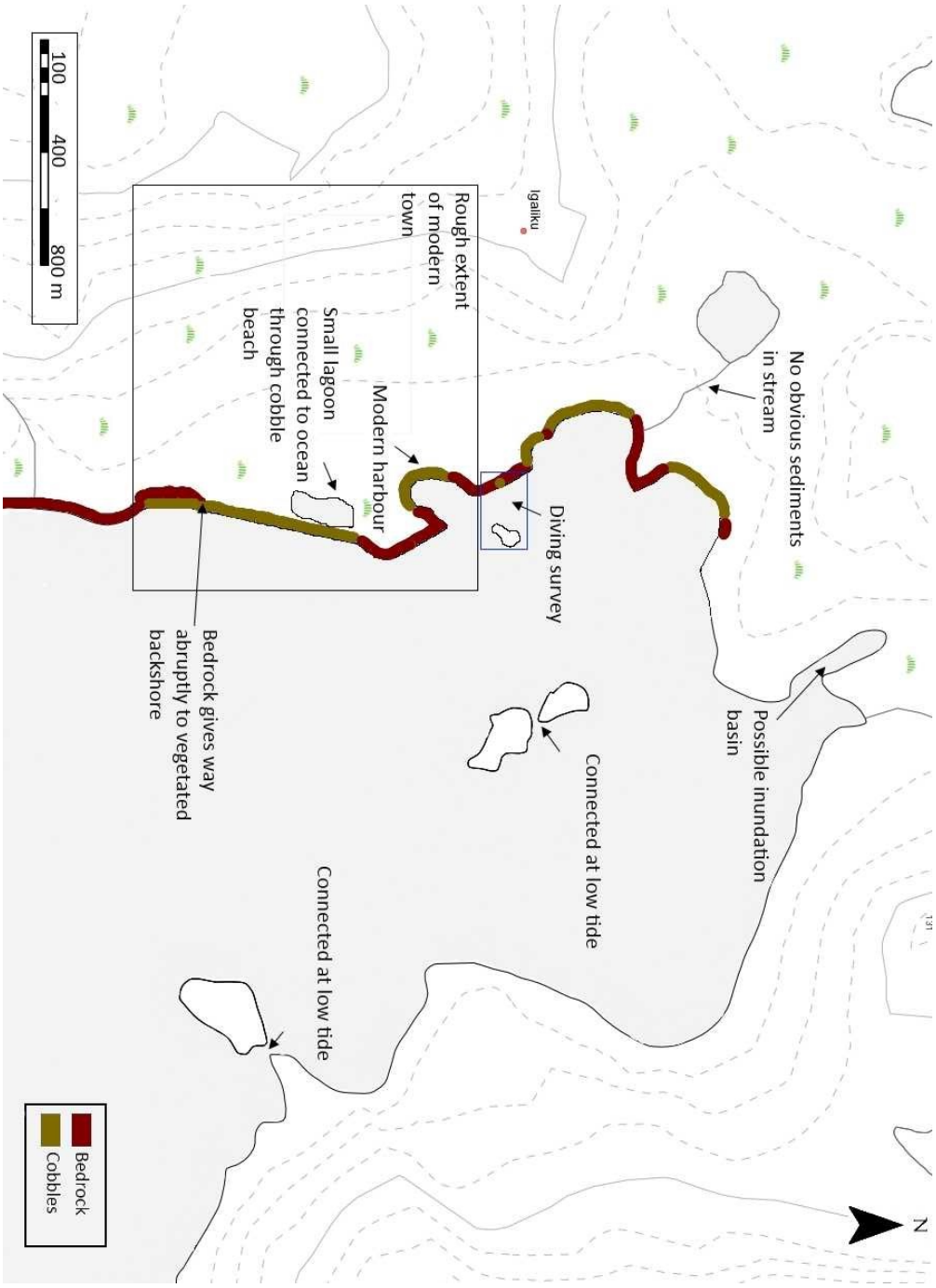

Appendix C – Soil core photographs

Please refer to respective geomorphic maps for location of soil cores.

C1 - Burra Firth

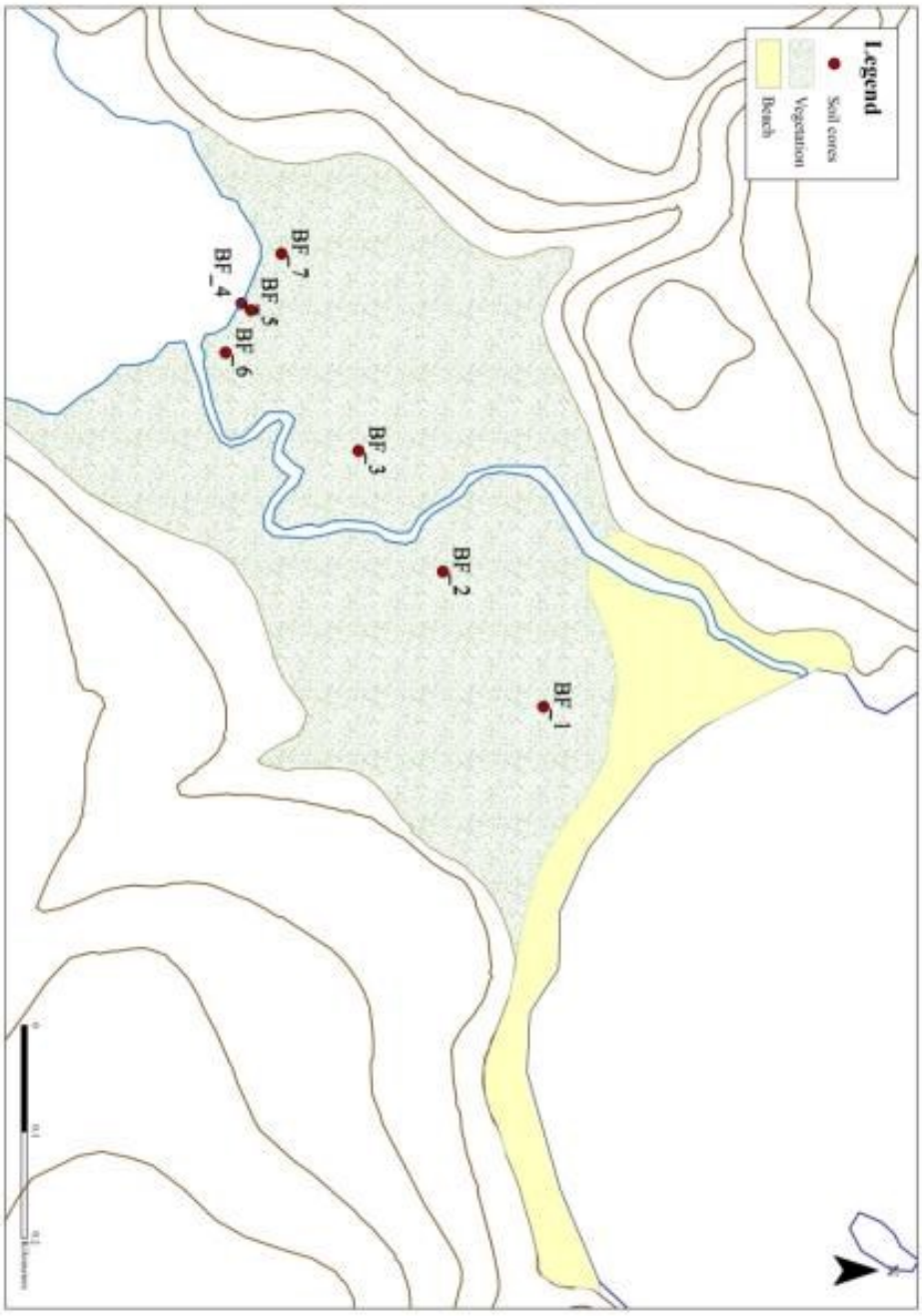

BF_1

BF_2

BF_3

BF_4

BF_5

BF_6

BF_7

C2 - Wick of Skaw

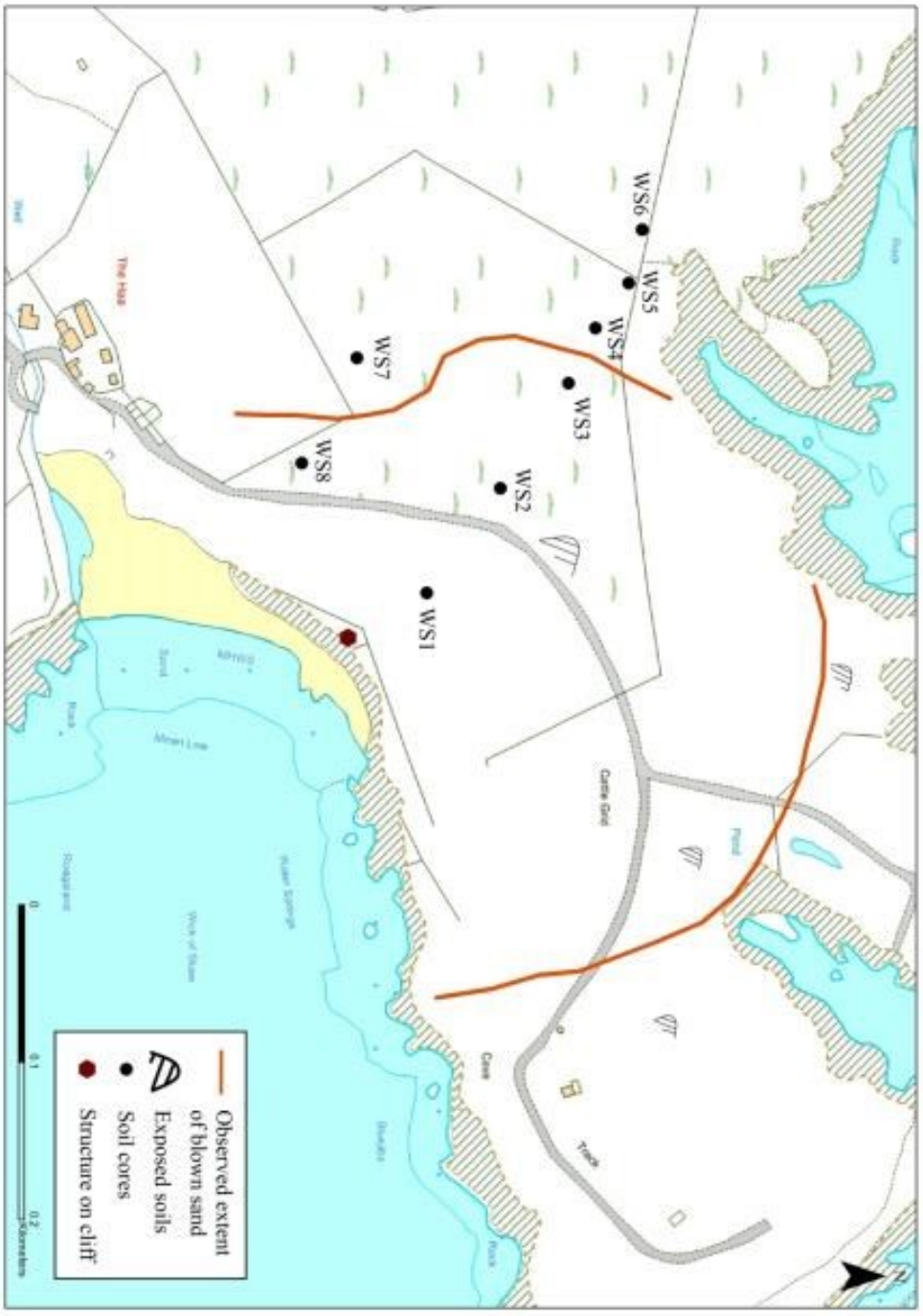

WS_1

WS_2

WS_3

WS_4

WS_5

WS_6

WS_7

WS_8

C3 – Sandwick

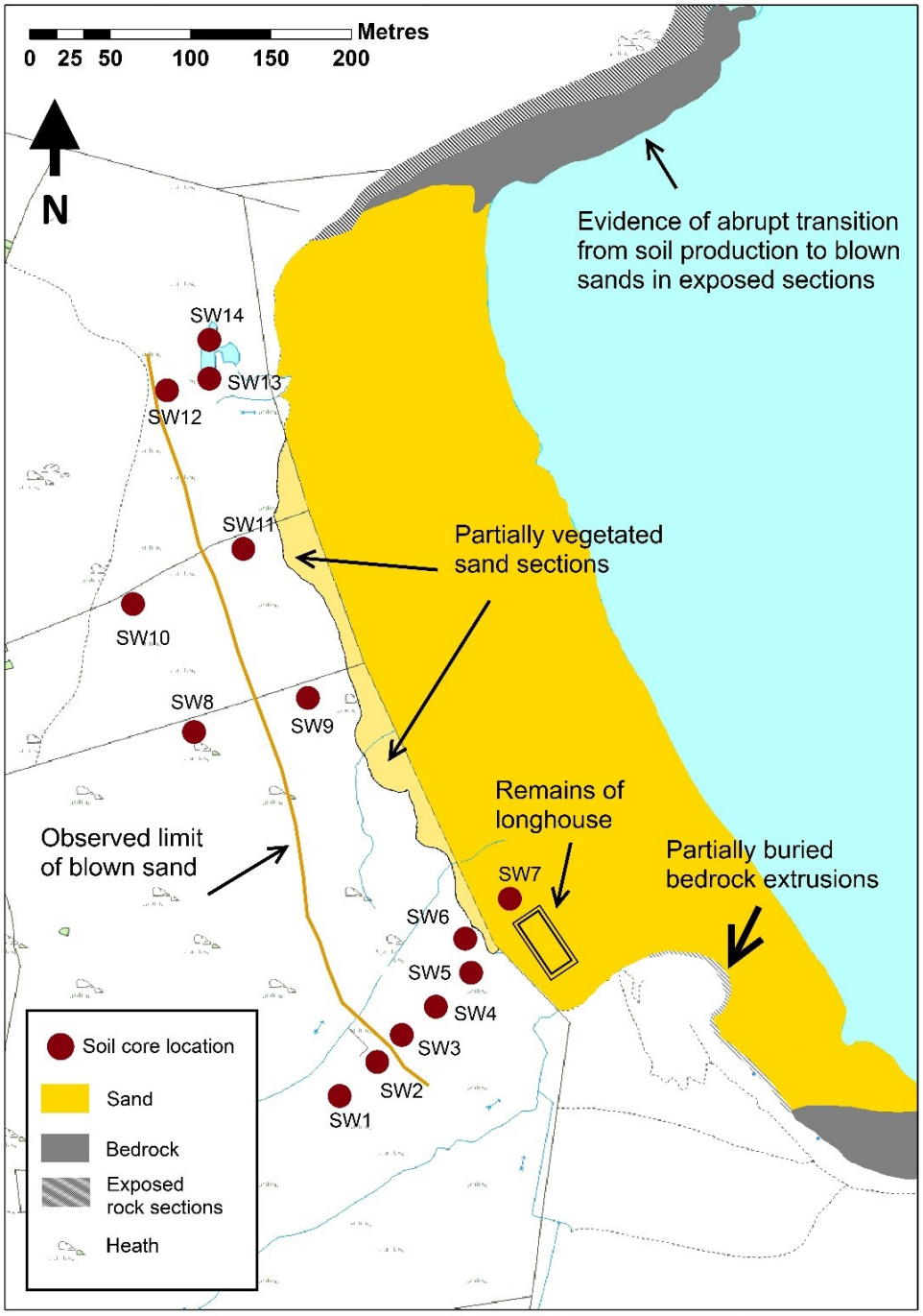
Metres
0 25 50 100 150 200
N
Evidence of abrupt transition from soil production to blown sands in exposed sections
SW14
SW13
SW12
SW11
Partially vegetated sand sections
SW10
SW8
SW9
Remains of longhouse
Observed limit of blown sand
Partially buried bedrock extrusions
SW7
SW6
SW5
SW4
SW3
SW2
SW1
Soil core location
Sand
Bedrock
Exposed rock sections
Heath

SW_1

SW_2

SW_3

SW_4

SW_5

SW_6

SW_7

SW_8

SW_9

SW_10

SW_11

SW_12

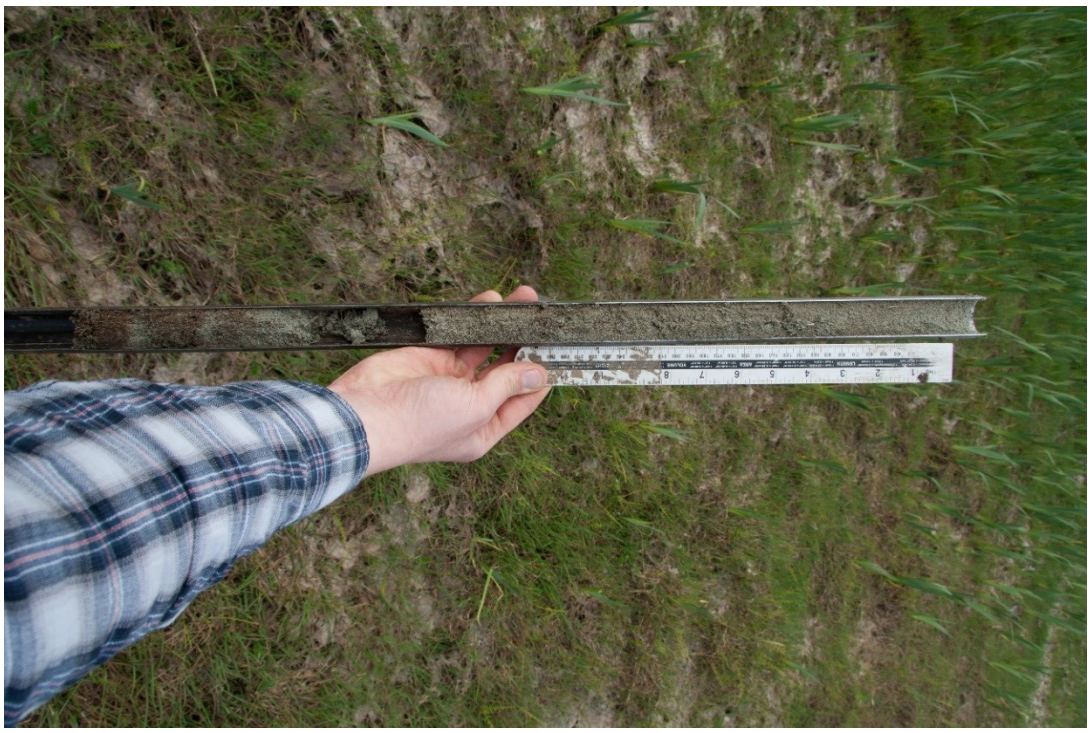

SW_13

SW_14

Appendix D – Model sensitivity

The following sensitivity results are for the model runs as reported in Chapter 4.2.4 of the thesis.

D.1 Wave angle change

The model indicates that the impact of changing the incident wave angle on sediment accumulation patterns is varied (Figures D1 a-d, D2 a-d).

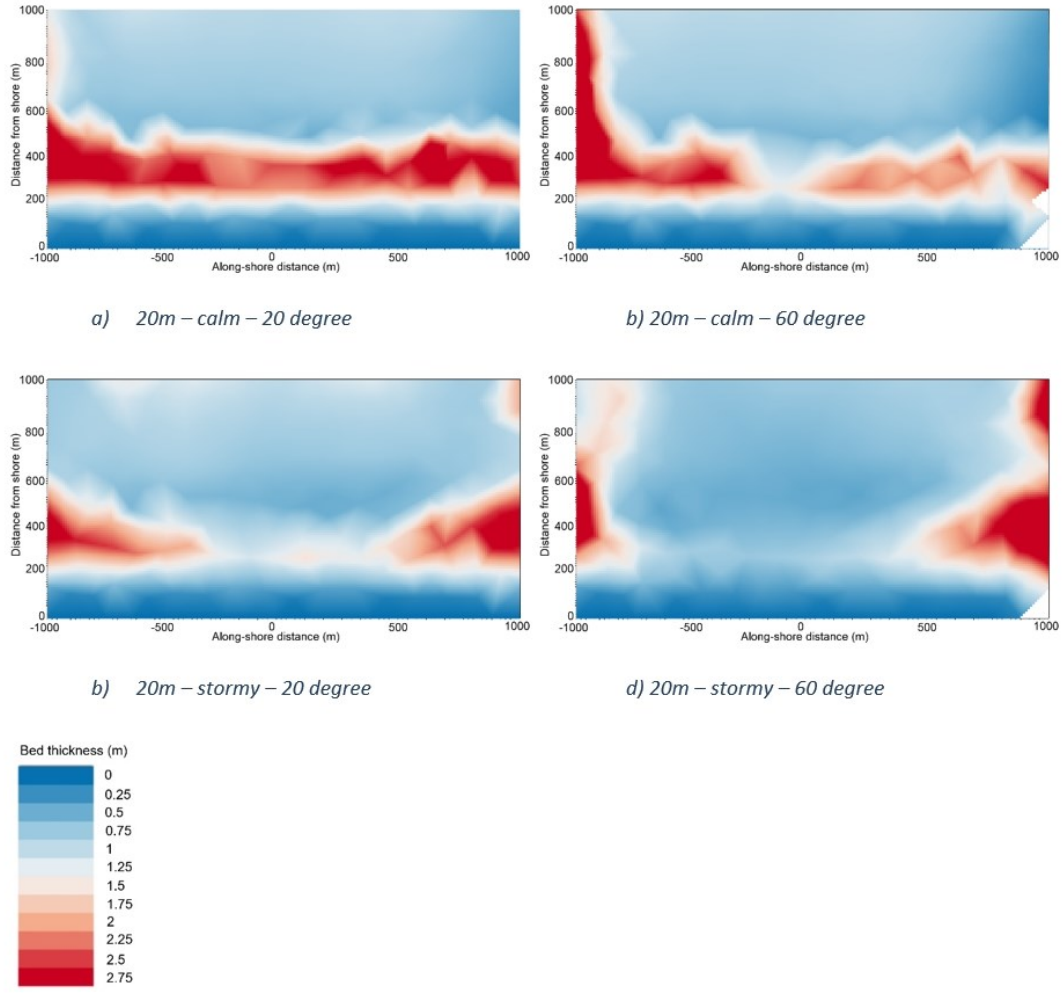

Figure D1 17 - Wave angle change (20° and 60°) sensitivity analysis – 20m depth. Little change in sediment transport patterns is seen with a 20° angle change, but a much more pronounced changed with a 60° angle change, with significant sediment rotation towards deeper water observed.

For the shallow depth scenario of 20m, changing the incident wave angle to 20° has little effect on nearshore sediment accumulation under both the calm and stormy scenarios. Some rotation towards the western headland wall is seen in the calm

scenario, but very little change is seen in the stormy scenario when compared to the 0° wave angle of the primary model runs. When incident wave angle is increased to 60°, sediment rotation in the calm scenario is much more pronounced, with sediment accumulation increased along the western headland wall although a sand bar does still form, sediment thickness is reduced throughout when compared to the primary model runs. In the storm scenario, sediment is rotated away from the shoreline almost completely and accumulates asymmetrically along both headland walls in deeper water.

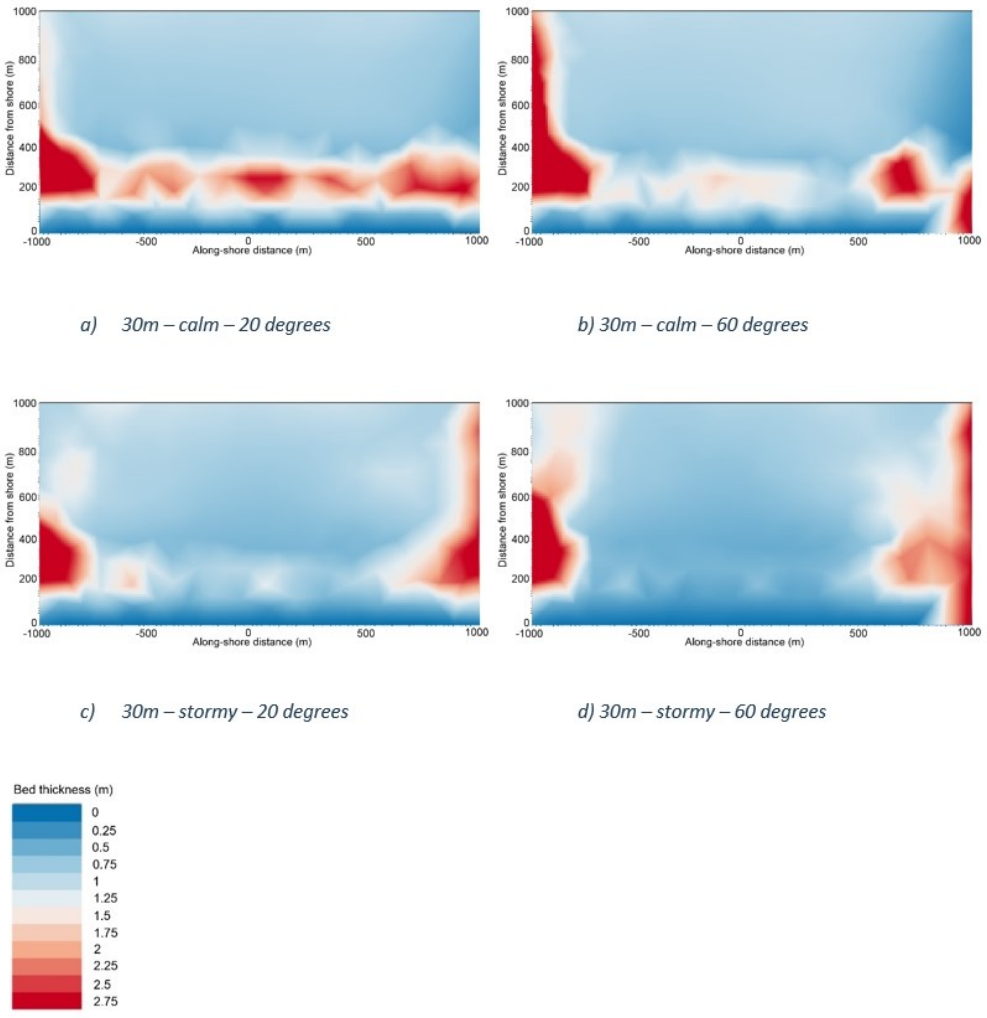

Figure D2 - Wave angle change (20° and 60°) sensitivity analysis - 30m depth. As with the 20m scenario, little change in sediment transport patterns is seen under the 20° scenario, but significant changes again are observed under the 60° scenario, with almost all sediment being removed from nearshore and accumulating against the headland walls and out to sea.

For the deep water 30m scenario, changing the incident wave angle from 0° to 20° has a relatively minor effect on sediment accumulation in both calm and stormy scenarios. As in the 20m scenarios, some sediment rotation towards headland walls is observed. Changing the incident wave angle to 60° has a dramatic effect, with no nearshore sand bars forming at all and almost all sediment accumulation occurring against the headland walls. Some model instability is seen in figures b) and d), in which sediment accumulates in the swash zone, however this impacts less than 0.25% of the domain, and thus has a negligible impact on the results.

D.2 Tidal range change

Figures D3 a) to d) show sediment accumulation patterns after 10 years with the tidal range in the model increased from 2.56m to 5.7m.

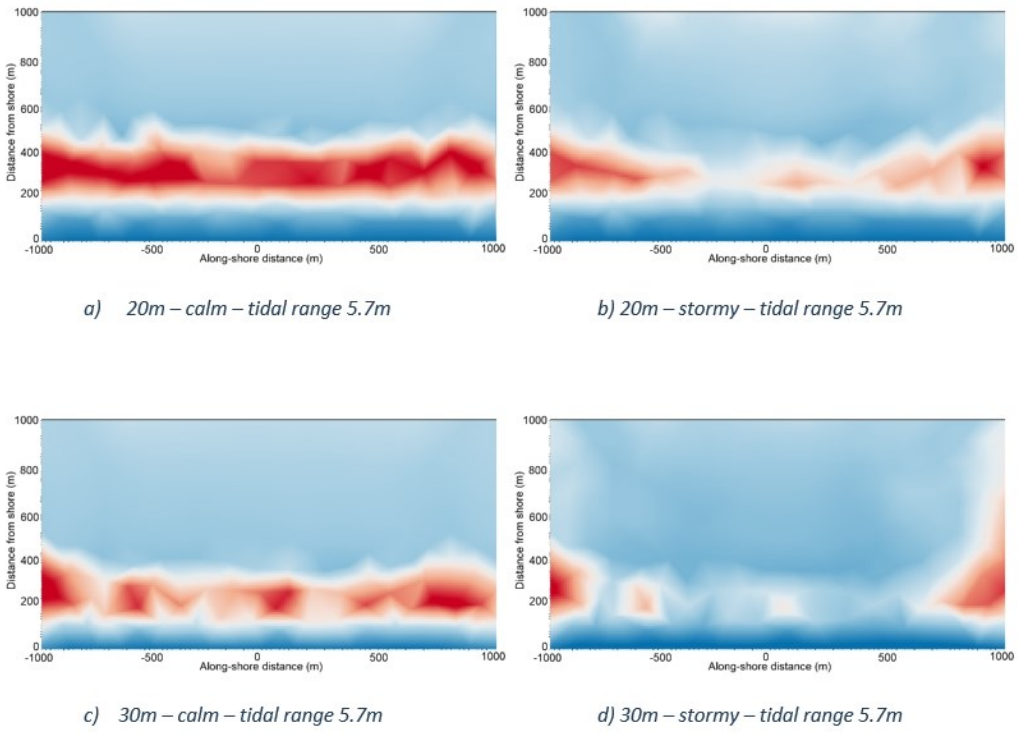

Figure D3 - Sensitivity analyses of tidal range change

When compared to the primary model runs, the model appears insensitive to an increase in the tidal range. Very little change is observed in each scenario, with only some slight additional sediment accumulation along the eastern headland wall in the 30m stormy scenario.

This page intentionally left blank.